UiT The Arctic University of Norway

Department of Chemistry, Faculty of Science and Technology

Inherent Chirality and Stereoisomerism in Metallocorrole Sandwich Compounds

-

Kristian Torstensen

KJE-3900 Master's Thesis in Molecular Science, January 2024

Abstract

In this thesis, I have presented my findings on stereoisomerism in eight-coordinate metallobiscorrole sandwich compounds. Metallobiscorroles were first synthesized in our laboratory about eight years ago and, although they were fully structurally characterized with X-ray crystallography, their crowded ^{1}H NMR spectra essentially defied assignment. My master's thesis project began with the task to synthesize partially fluorinated metallobiscorrole systems that would prove amenable to a full ^{1}H and ^{19}F NMR analysis.

Earlier density functional theory calculations on the metallobiscorroles indicated the possibility of two square-antiprismatic diastereomers in which the corroles are rotated approximately 45 and 135 degrees relative to each other. Furthermore, each diastereomer is inherently chiral, approximately C_2-symmetric, and exists as a pair of enantiomers. The calculations also unambiguously indicated that each stereoisomer was configurationally stable, making the metallobiscorrole core doubly stereogenic, giving rise to both diastereomerism and enantiomerism. To date, however, only the 135 degree diastereomer has been experimentally reported. In this thesis, I have provided fully assignable NMR analysis of a handful metallobiscorrole complexes, and strong experimental evidence for the successful synthesis of both diastereomers and thereby formal proof of the doubly stereogenic character of metallobiscorrole sandwich complexes.

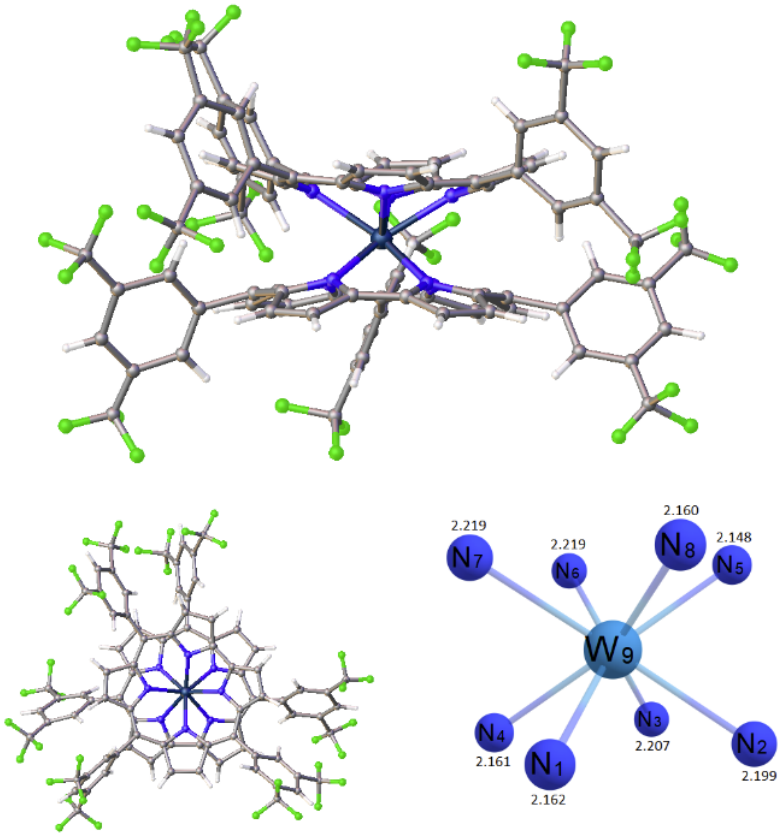

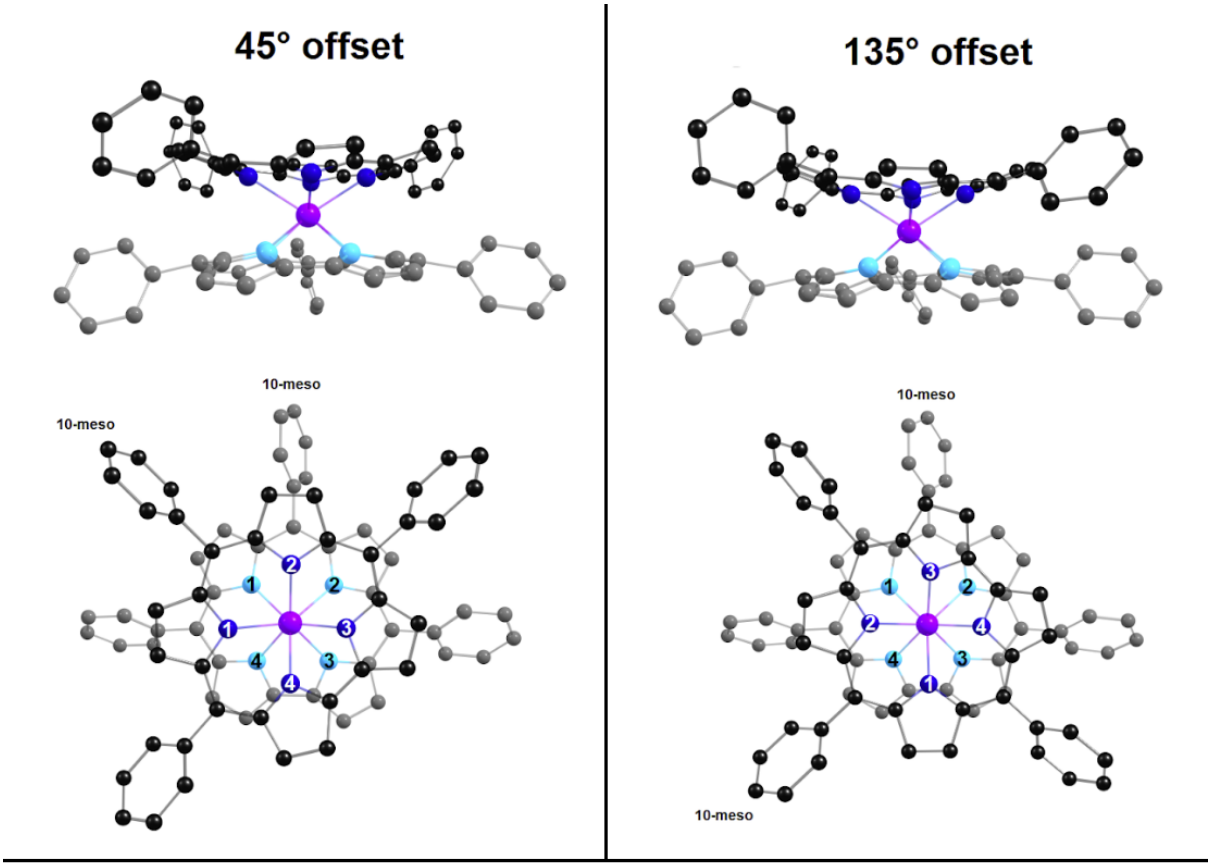
45° offset
135° offset
10-meso
10-meso
10-meso
10-meso

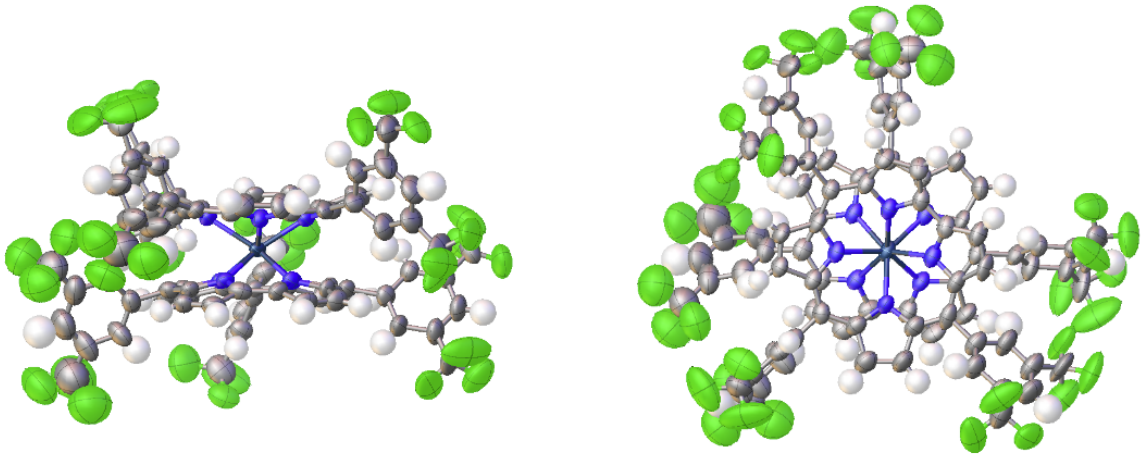

Acknowledgement

I would like to first and foremost thank my advisor Prof. Abhik Ghosh for supplementing my degree with special topic courses, and building *added value* into various projects. Additionally, I extend my appreciation to his collegial research group composed of fellow students and senior researchers Dr. Simon Larsen and Dr. Abraham Alemayehu, where Dr. Alemayehu has served as my laboratory advisor on a day-to-day basis. I'm very honored and grateful to have been a part of this research group, and I can wholeheartedly recommend Abhik's research group for future students.

I would also like to thank the engineers in the department for general assistance, especially Dr. Truls Ingebrigtsen for being very patient with me and my multiple variable temperature NMR experiments.

Lastly, I would like to thank an old friend who inspired me, and most of all assisted me in the early days of my transition into science. I am forever grateful.

Kristian Torstensen
Tromsø, January 2024

1 INTRODUCTION TO COORDINATION CHEMISTRY AND PORPHYRINOIDS

1.1 Transition Metal Complexes

Transition metals denote the elements found in the periodic table between group 3 and 12. The term transition was first used by the English Chemist Charles R. Bury in 1921 to describe the transition from what is today known as the s- and p-block.[1]

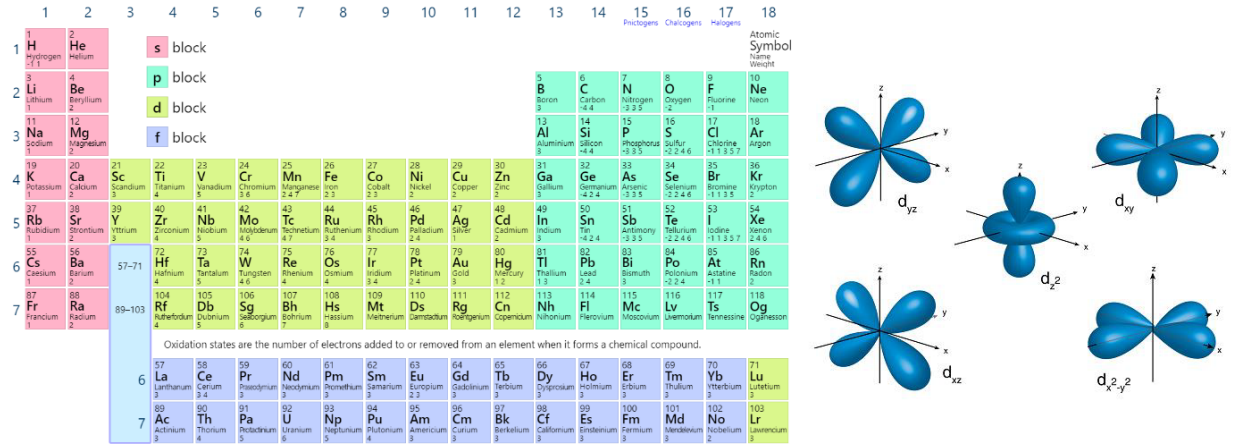

Figure 1. Overview of periodic table including coloring for s-, p-, d- and f-block elements[2], and coordination of d-orbitals. Reused with permission from ref. [3].

The transition elements with its d-orbital valence electrons act as a bridge between the main group elements with s- and p-orbital valence electrons. All transition elements are metals, thereby the name transition metals. The spatial orientation of the d-orbitals allows for rather unusual coordination chemistry compared to the lightest main group elements. Based on occupancy and substituents, the d-orbitals can both act as nucleophiles and electrophiles to form chemical bonds. The bonds formed with transition metals are often seen as coordination bonds between the central metal atom and peripheral ligands, which are often negatively charged ions or molecules with lone pair electrons. The ligands usually contribute with a lone pair of electrons which can be stabilized by interaction with the empty hybridized orbitals located on the central metal. Coordination numbers seen in transition metal complexes are usually 2, 4 and 6 with respectively linear, tetrahedral or square-planar and octahedral geometries. It is however not usual to encounter square antiprismatic eight-coordinate transition metal complexes involving early transition metal due to their mostly empty d-orbitals.

Biologically active transition metal complexes are often categorized as heme or non-heme complexes based on the presence or absence of the tetradentate heme ligand. The heme and non-heme categorization speaks volumes for the importance of the heme ligand in biological chemistry - although, there are multiple biologically important non-heme metal complexes such as alpha-ketoglutarate-dependent non-heme iron proteins which open up for a wide range of biologically important biosynthetic and metabolic pathways.[4]

1.2 Ligand Field Theory

The first field theory for studying the nature of transition metal d-orbitals was the crystal field theory developed in 1929 by the German physicist Hans Bethe.[5] The theory assumed all ligands to be negative point charges, giving a fair estimation of the true nature of ligands. In fact, the overall scheme of d-orbital energy splitting proposed by the crystal field theory still remains today. The theory was extremely applicable and simple to use, and more than 20 years would pass before a complementing theory was invented. In the 1950s, the British chemists John F. Griffith and Leslie Orgel proposed the ligand field theory.[6] The ligand field theory ultimately built upon the crystal field theory, with the extension of using molecular orbital theory for the ligand interactions. This involved no longer assuming ligands to be identical negative point charges located around the metal atom, but rather as molecular systems with unique properties. Although the complexity of the ligand field theory was increased by the introduction of molecular orbital theory, the accuracy was greatly improved. Almost 70 years later, ligand field theory still remains as a powerful tool in the study of transition metal complexes.

Ligand field theory builds upon the molecular orbital interaction between the metal d-orbitals and the ligand orbitals. The five metal d-orbitals are completely degenerate with respect to energy levels in either vacuum or in a completely spherical ligand field. These are however hypothetical circumstances as real metal complexes do not naturally experience any of them.

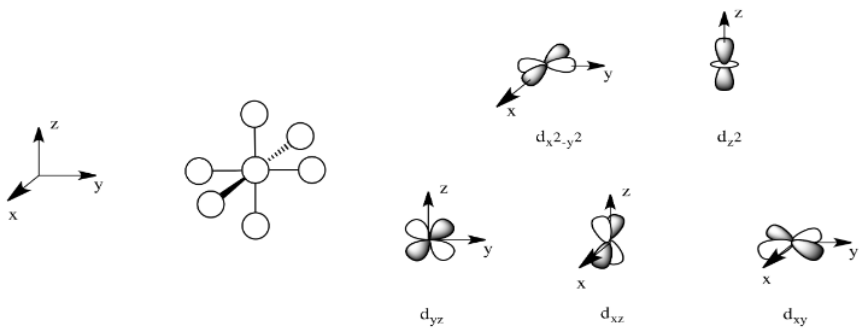

Figure 2. Visualization of molecular orbital interactions in an octahedral complex. Reused with permission from ref. 7.

By aligning the ligands in an octahedral complex along the x, y and z axis, a clear distinction between the transition metal d-orbitals quickly arises. The ligand field surrounding the metal is no longer uniformly distributed, causing two of the five metal d-orbital to interact head on with the metal-ligand bonds ($d_{x^2-y^2}$ and d_{z^2}). This induces an asymmetry of the metal d-orbitals, instead splitting them into two sets of degenerate orbitals, namely e_g and t_{2g}. The two orbitals aligned directly towards the negatively charged ligands on the x, y and z axis are raised in energy, and act as antibonding orbitals for the complex. However, the three t_{2g} orbitals (d_{yz}, d_{xz}, d_{xy}) are neatly placed between the axis and are thus lowered in energy. As the t_{2g} orbitals are not aligned directly towards the ligands they cause no bonding or antibonding interactions, and are thus non-bonding orbitals in transition metal complexes.

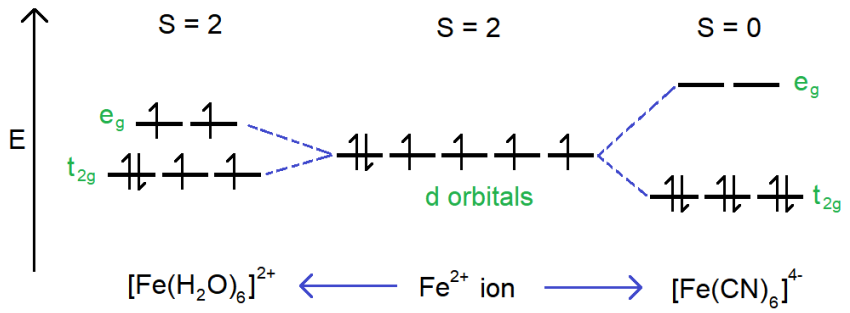

Figure 3. Illustration of metal d orbital splitting in an octahedral field in presence of none, weak and strong field ligands.

A classic example of metal d orbital energy splitting caused by ligands in an octahedral geometry can be seen in Figure 3. Crystal field theory would treat the $[Fe(H_2O)_6]^{2+}$ and $[Fe(CN)_6]^{4-}$ complexes indifferently - it would accurately predict the metal d orbital energy splitting into e_g and t_{2g}, but it would say nothing about the magnitude of the energy splitting. On the other hand, ligand field theory would also take the molecular properties of the ligand into consideration, accurately predicting both the metal d orbital energy splitting and the magnitude. In the example of $[Fe(H_2O)_6]^{2+}$ and $[Fe(CN)_6]^{4-}$ complexes, the magnitude of the energy splitting is crucial to predict the total spin states of the complexes.

Ligand field theory distinguishes between weak, intermediate and strong field ligands. Weak field ligands are the ligands that induce a small energy splitting of the metal d orbitals, which usually result in high spin complexes. A common property of the weak field ligands are

molecules which possess π-donor capabilities, such as halogens or H_2O. Intermediate field ligands are however usually neither π-donating or π-accepting, such as ammonia, and they produce intermediate energy splitting causing both high and low spin complexes. The strong field ligands however, are usually π-accepting in nature such as carbon monoxide and cyanide, which allows for metal backbonding, ultimately stabilizing the t_{2g} orbitals.

The total electron spin of transition metal complexes therefore greatly depends on the magnitude of the energy splitting of the d-orbitals induced by the ligand effects. Strong field ligands can raise the e_g orbitals to the point where electron pairing in the t_{2g} orbitals becomes energetically favorable, such as seen in the $[Fe(CN)_6]^{4-}$ complex. In contrast, weak field ligands often induce a too small d orbital splitting where the energetic penalty of pairing electrons exceeds the electron filling in the raised e_g orbitals, as seen in the $[Fe(H_2O)_6]^{2+}$ complex. For most chemical compounds not involving transition metals, the electron spin of the system is taken for granted as low spin, as the energy levels between the subsequent electron subshells largely exceed the pairing energy of electrons - with the exception of some rare and uniquely designed molecules with inverted singlet-triplet gaps.[8] Transition metal complexes however, need to be carefully examined for correct spin states as the d orbital energy splitting usually lies within the same order of magnitude as the electron pairing energy.

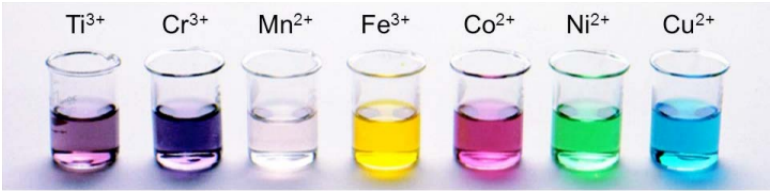

Figure 4. Colors of different metal aquo complexes.[9]

The relatively low energy splitting between the frontier molecular orbitals in transition metal complexes often allows for electronic transitions observable within the visible and ultraviolet spectrum - explaining why many transition metal complexes are commonly used as pigments. This property of transition metal complexes thus opens up a world of possibilities within photophysical chemistry.

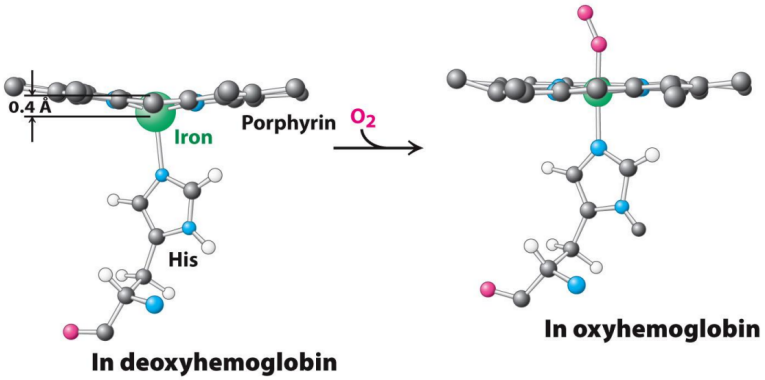

Figure 5. Examples of square pyramidal and octahedral geometry induced by the presence of bound oxygen in hemoglobin. Reused with permission of ref. 10.

Metal complexes involving the biologically important tetradentate heme structure often induces geometries such as square planar, square pyramidal and octahedral with respectively 4, 5 and 6 metal-ligand σ-bonds. Biologically active complexes will often have chemical processes transitioning between these geometry states, an example of this is bound and unbound oxygen to the heme transportation complex. When the heme complex picks up oxygen, it transitions from a square pyramidal to an octahedral geometry. The metal center of the deoxyhemoglobin is seen to be slightly shifted out of the heme plane as a way of further stabilizing the metal d orbitals, making them less overlapping with the σ-bonds. This is a common theme for all transition metal complexes with square pyramidal geometry which includes a planar tetradentate ligand such as the heme ligand.

1.3 Porphyrins

1.3.1 An Introduction

Porphyrins are tetrapyrrole aromatic molecules with extreme versatility within biological chemistry. They are commonly known to be responsible for both the abundant green color of grass and the red color of blood. A series of biologically important porphyrins and porphyrin analogues are found in nature, including the heme cofactors responsible for transporting oxygen in our bodies, heme proteins responsible for oxygenase such as cytochrome P450 and the heme complexes in chlorophyll - responsible for the energy absorption in photosynthesis. These discoveries were generally done in the middle of the 19th century, and the widespread scientific interest in porphyrinoids was thus established.11 12

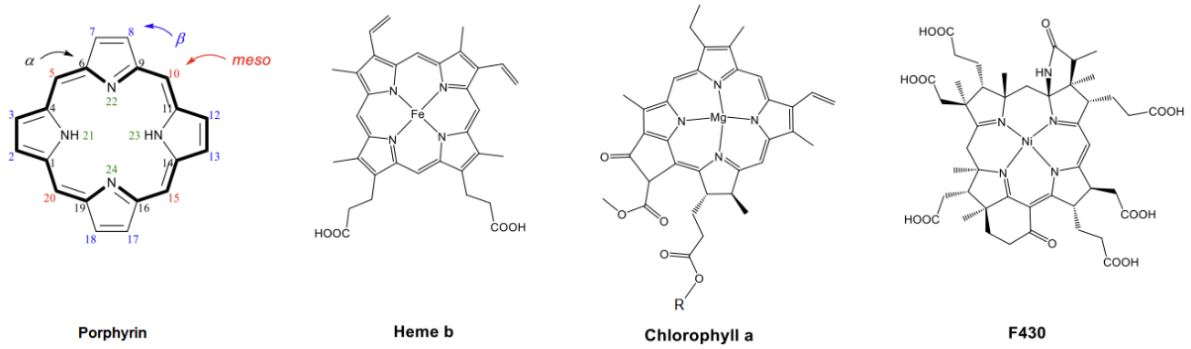

Figure 6. Example of a porphyrin with α, β, and meso positions, including the 18 electron aromatic system indicated in bold, together with three biological active and naturally occurring metalloporphyrins. Redrawn from ref. 13.

The porphyrin skeleton can be depicted as four pyrrolic units linked by methine bridges to create a planar and strongly aromatic structure. Electronically, porphyrins are 22 π-electron species where 18 π-electrons can participate in the aromatic system at the time. The stable state of metal-free porphyrins holds two hydrogens in the tetradentate N_4 cavity, which are rapidly exchanged between the nitrogens - this induces tautomerism of metal-free porphyrins. Upon deprotonation of the internal hydrogens, porphyrins become -2 charged tetradentate ligands.

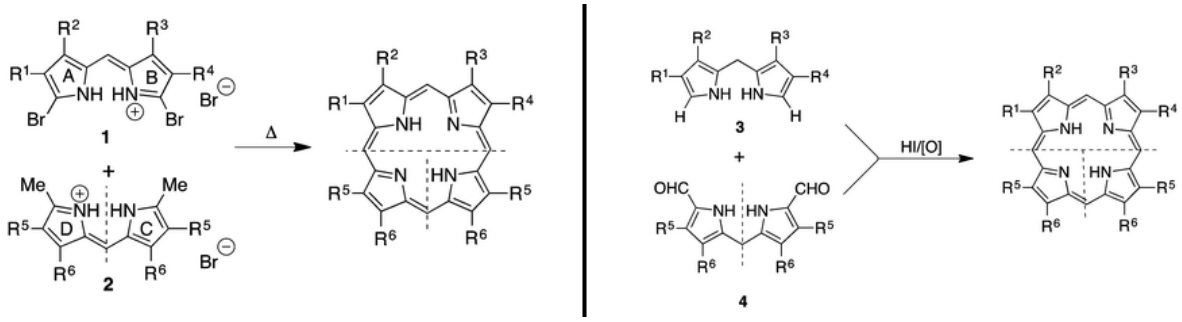

Figure 7. The first synthetic routes towards porphyrins. Left: Fischer, 1929. Right: MacDonald, 1960.

A synthetic route towards artificial porphyrins was first discovered in 1929 by the German chemist Hans Fischer, who also received the Nobel prize in 1930 for his work related to pyrroles and porphyrins.14 The synthesis consisted of a condensation reaction of dipyrromethene salts in strongly heated organic acids. Although the yields were modest, Fischer and his research group carried on to synthesize hundreds of porphyrins. A major improvement was proposed by the Canadian chemist Fergus MacDonald in 1960. The

method involved formyl-substituted dipyrromethanes in a 2+2 cycloaddition reaction, under much milder reaction conditions than Fischer's method.

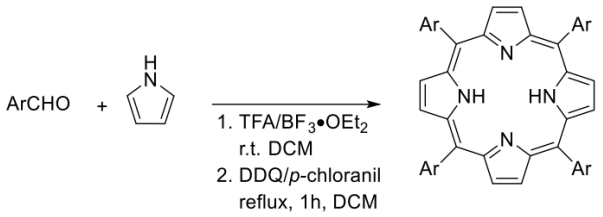

Figure 8. Synthetic route proposed by J. Lindsey in 1986 to obtain artificial porphyrins in high yields.[13]

The first one-pot synthetic route towards artificial porphyrins was proposed in 1935 by Paul Rothemund, and the synthesis laid the groundwork for what would eventually become the overall principal porphyrin synthesis proposed by Jonathan Lindsey in 1986.[15] Lindsey's synthetic route was particularly mild, and involved mixing of equimolar amounts of pyrrole and aldehyde in dichloromethane in the presence of trifluoroacetic acid or boron trifluoride etherate, followed by oxidation of DDQ or *p*-chloranil to yield artificial porphyrins in high yields.

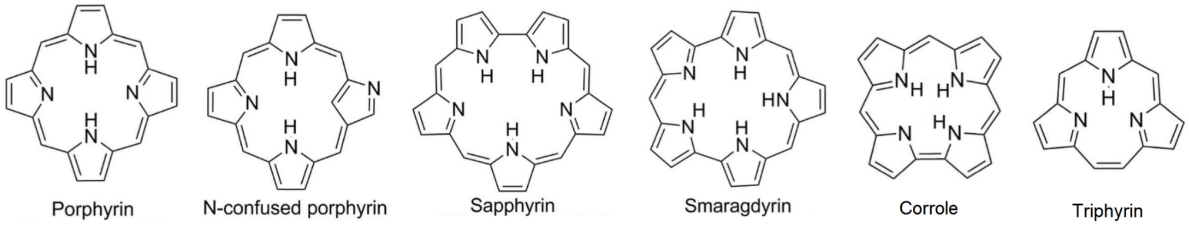

Figure 9. Examples of isomeric, expanded and contracted porphyrinoids.

Since then, plenty of other isomeric, expanded and contracted porphyrinoids have been synthesized and characterized. The analogues share many of the physical properties of porphyrin, such as readily forming transition metal complexes of various kinds. Most notably, the size of the N_4 cavity is highly dependent on expansions or contraction of the porphyrin skeleton, thus allowing for a wide variety of coordination complexes involving porphyrinoids.

1.3.2 Metalloporphyrins

Most of the interesting properties of porphyrinoids arise when metals are inserted into the N_4 cavity. The central metal is usually heavily involved in the frontier orbitals of porphyrinoids, thus indicating a location of reactivity.

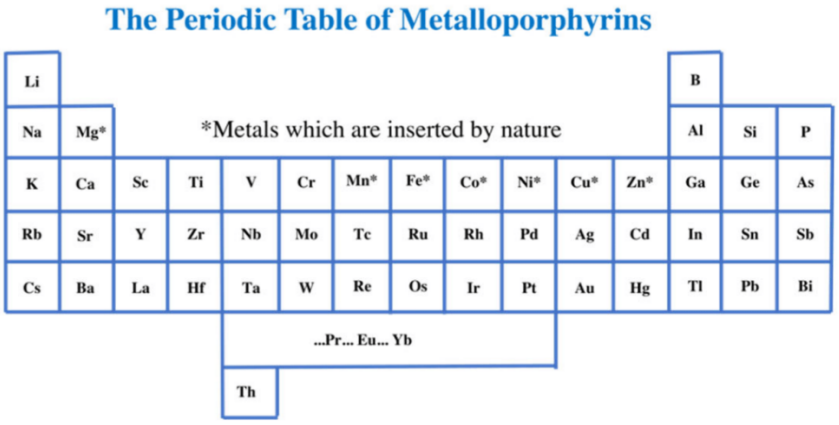

Figure 10. Periodic table of metalloporphyrins published in 1978 by Canadian biochemist David Dolphin.[16]

The field of metalloporphyrins was already thoroughly researched in the late 70's, and almost all metals were already successfully inserted into the porphyrin N_4 cavity - despite only seven of them being found inserted naturally. The most common form of metal insertion into porphyrins include refluxing metal halides or carboxylates with free-base porphyrin in basic, high boiling point solvents such as DMF or pyridine - where the basic solvents help with the neutralization as the internal porphyrin protons are lost upon metalation.[17] More recently, other methods such as microwaving or mechanochemistry have been successfully used to insert metals into porphyrins.[18]

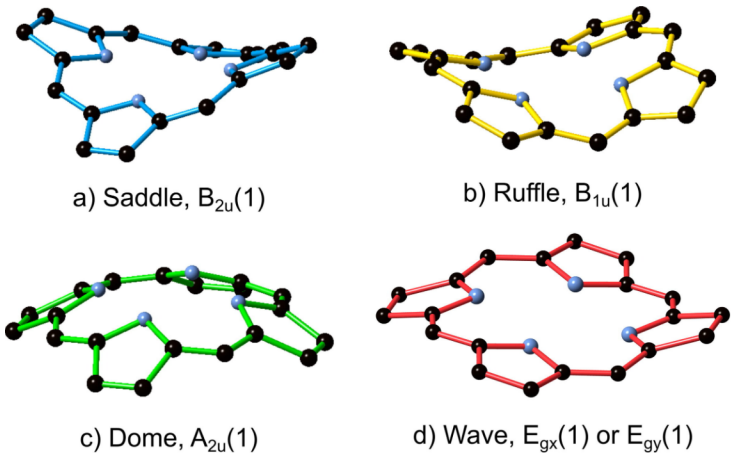

Figure 11. Geometry distortion observed in metalloporphyrins and metallocorroles. Reused with the permission of ref. [19].

Although both porphyrin and corroles are highly aromatic systems and naturally planar for the vast majority of metal complexes, a good portion of metalloporphyrins and metallocorroles experience geometry distortions to at least some degree. The non-planarity

of such metallated porphyrinoids are usually induced by either strong metal-porphyrinoid orbital interaction or peripheral steric crowding caused by bulky beta- or meso-substituents. A major difference in metallporphyrins and metallocorroles is that the latter are more rigid structures and less prone to many of the geometry distortions. Saddling in metalloporphyrins have been observed to primarily be caused by peripheral steric crowding, where saddling in metallocorroles are found to be caused by specific metal-corrole orbital interactions commonly seen in e.g. copper, silver and gold corroles.[20] Ruffling on the other hand, can often be induced in metalloporphyrin by insertion of a small central ion such as silicon, phosphorus or arsenic - on the contrary, strong ruffling in corroles was found to be essentially impossible after a thorough investigation.[21] Doming can frequently be observed in both metalloporphyrins and metallocorroles of square pyramidal geometry, where the fifth ligand pulls the central metal out of the tetradentate plane, as depicted in Figure 5. Another cause of doming can occur when the inserted metal exceeds the size of the N_4 cavity.

1.3.3 Cytochrome P450

A most important instance of biological active metalloporphyrins is the host-guest chemistry found in the cytochrome P450 protein family. The iron-porphyrin, heme, can be found as a cofactor inside the relatively large protein structures, and is responsible for biological monooxygenase.

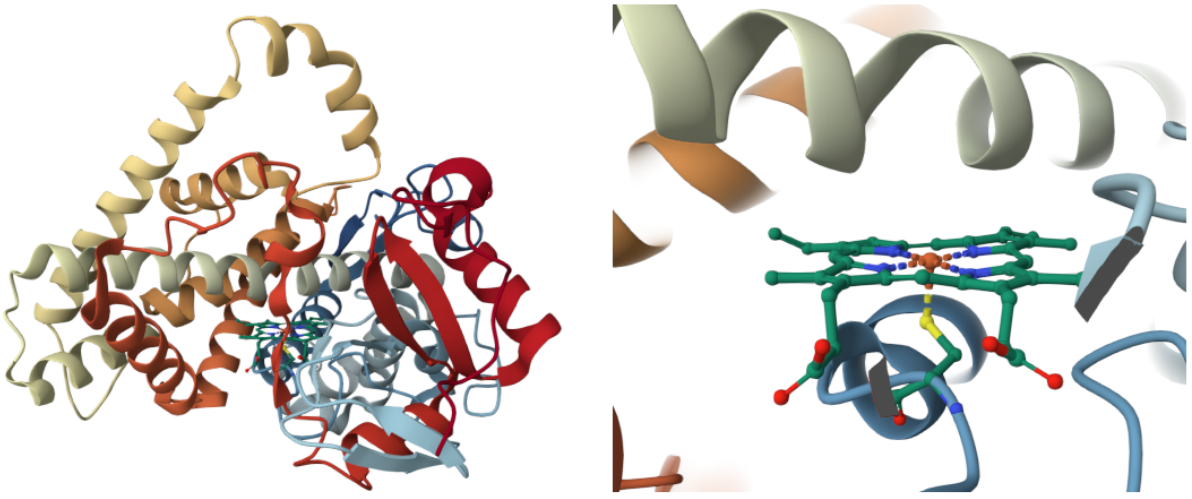

Figure 12. X-ray crystal structure of cytochrome P450 2B4 found in European rabbit, PDB entry: 1PO5.[22]

Since it's first discovered in 1961, cytochrome P450 has been thoroughly investigated to say the least - approximately 350 000 sequences have been collected and more than 45 000 crystal structures are available in RCSB protein database.[23] Only a total of 18 of the more than 270 discovered cytochrome P450 gene families are present in mammals, this

underlines the widespread presence of cytochrome P450 in living species. In fact, the cytochrome P450 protein family is found in every kingdom of life! This gives a precedence of how essential the monooxygenase biological processes are for living organisms to get rid of toxins and other water insoluble compounds. It is therefore to no surprise that cytochrome P450 proteins are of huge scientific interest also in the field of pharmacology, given the fact that they are largely responsible for the metabolism of drugs. In depth understanding of the cytochrome P450 protein family is therefore necessary to explain deficiencies, side effects and even toxicity of drugs given to some people.[24]

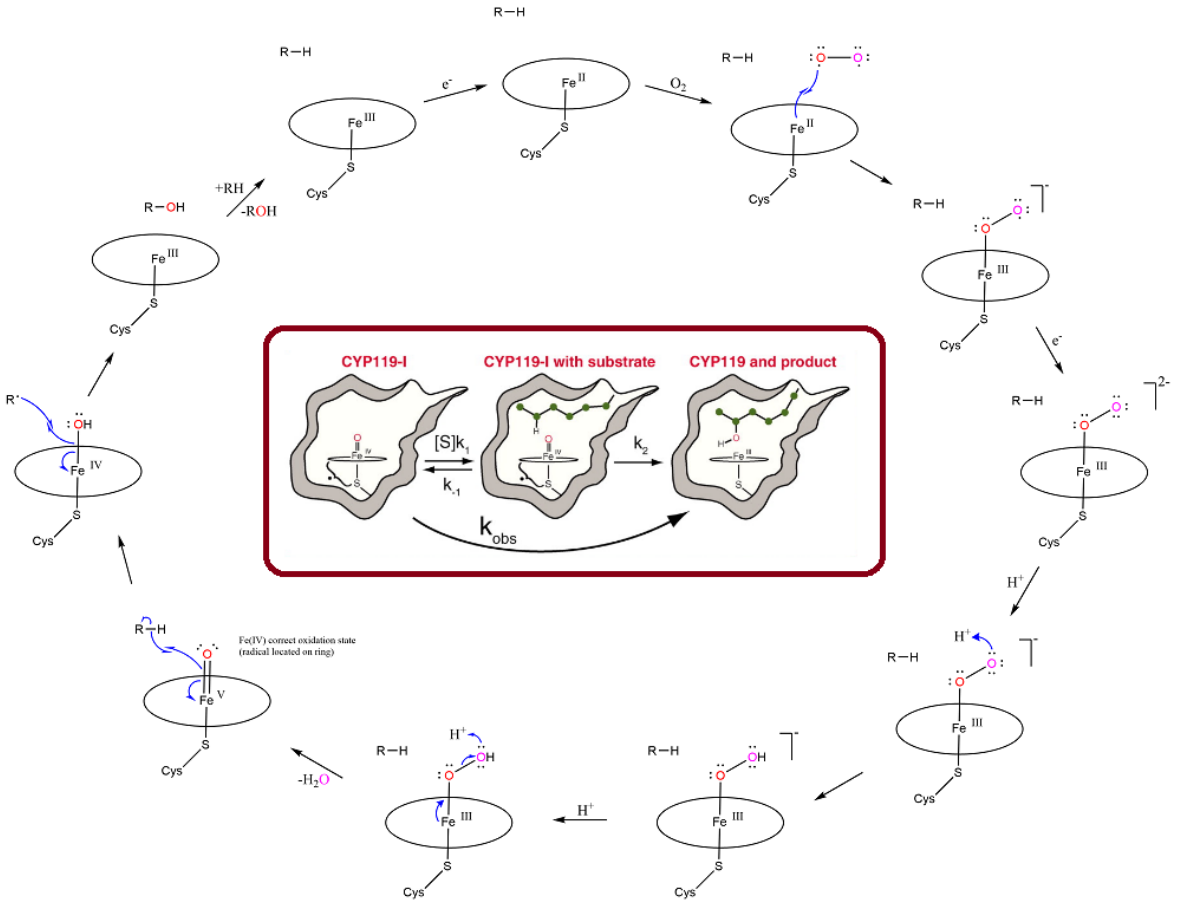

Figure 13. General scheme of biological mechanism catalyzed by cytochrome P450 proteins, with the heme ligand depicted as a ring around the central iron.[25] Imbedded illustration shows an example monooxygenase catalyzed by CYP1194, reused with the permission of ref. [26].

The monooxygenase reaction catalyzed by cytochrome P450 proteins reflect a coordinated interplay among the central iron atom, the porphyrin ligand and the axial cysteine ligand. Additionally, the protein itself is also responsible for the capture and delivery of two electrons onto the metal complex. Compound I, also known as the Fe^{V}=O state, is depicted as a

simplification of the true nature of this state. More precisely, the state is actually a Fe^{IV}=O complex, with the radical electron partially located on the heme ligand and to some degree also on the cysteine sulfur. With this in mind, the high reactivity of Compound I is therefore quite understandable, and this gives a rationale for how even aliphatic hydrogen abstractions can take place.[26]

2 CORROLES

2.1 An Introduction

The rise of scientific interest in porphyrins and the analogue corrin, which is the porphyrinoid ligand in vitamin B_{12}, led to an accidental discovery of the corrole ligand, first reported by Kay and Johnson in 1964.[27] Corroles are known as a contracted porphyrinoid which is missing one of the meso-carbons compared to porphyrin. Despite its contracted skeleton, corroles also possess an aromatic system made of 18 electrons. In contrast to porphyrins, corroles are not found in nature and are purely synthetical. Despite its relatively early discovery, corrole science was largely dormant for many decades afterwards. Synthetic difficulties involving the free-base corrole was a major bottleneck, and the primary reason for the dormancy of the field.

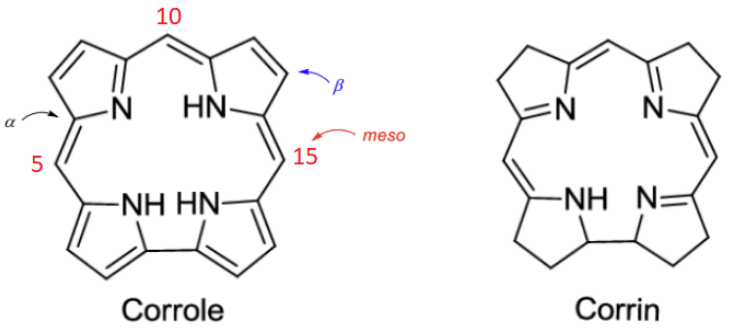

Figure 14. Structure of the porphyrinoids corrole and corrin, where the latter is naturally occurring in vitamin B_{12}.

The corrole structure did however spark modest interest in the ‘80s and ‘90s, but the great synthetic breakthroughs in the field came around the turn of the millennium. One of the largest obstacles of the corrole synthesis was the highly electron-rich nature of corroles leading them to be quite unstable and reactive. This could however be countered by attaching strong electron withdrawing substituents in the meso-positions, such as pentafluorophenyl or trifluoromethyl. The first one-pot syntheses of meso-substituted corroles was independently proposed by both Gross[28] and Paolesse[29] in 1999, and soon thereafter followed advances made by Gryko, such as synthetic routes towards A_2B corroles[30] and the all-famous water method.[31] The methods proposed by Gross and Paolesse in 1999 opened up the doors to relatively efficient corrole synthesis compared to the earlier methods, despite its modest yield ranging from 5-20 % - and this would ultimately mark the reignition of the scientific spark within corrole chemistry.

2.2 Synthesis

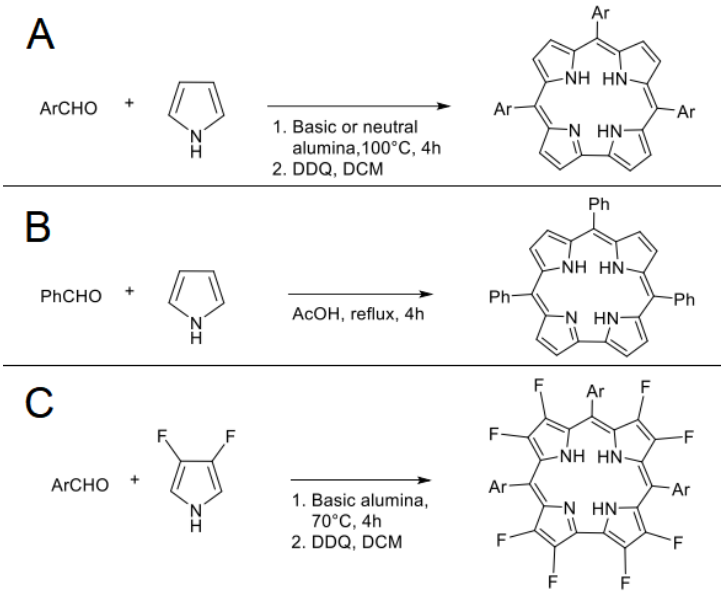

Figure 15. Overview of historical synthetic routes to meso-substituted free-base corroles. A) Gross[28], B) Paolesse[29], C) Ghosh[32].

Gross' and Paolesse's methods were both independently proposed in 1999, while Ghosh's method was a complementary expansion of Gross' method proposed four years later. While Gross' method was somewhat innovative using solid support with no solvent, Paolesse's method was simply a clever modification to the Rothemund porphyrin synthesis.[15] By using excess pyrrole in refluxing acetic acid for 4 hours, the corrole formation was found to be competitive with the formation of porphyrin, with a obtained 6 % yield of corrole and similar yields of porphyrin from the same one-pot synthesis.[29] The Ghosh group expanded the Gross method in 2003 to β-octafluorocorrole by using 3,4-difluoropyrrole instead of pyrrole, but under essentially the same reaction conditions with a reported yield of 6-8 %.[32]

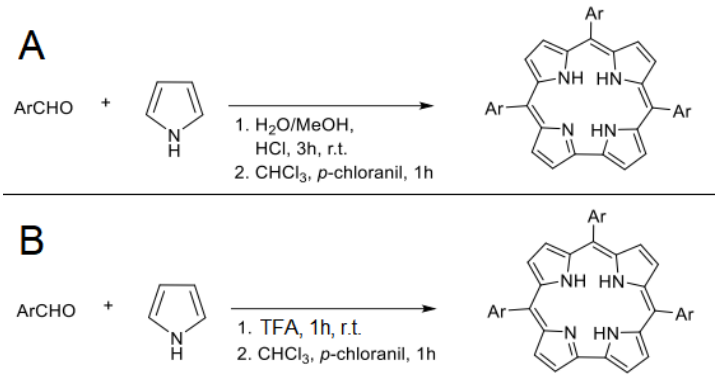

Figure 16. Presently used synthetic routes to meso-substituted free-base corroles. A) Koszarna and Gryko' water-methanol method[31], B) Example reaction of improved Paolesse' method.

Today, the Paolesse method have been improved by using trifluoroacetic acid or boron trifluoride etherate as catalysts instead of the acetic acid, and an additional oxidizing step with either DDQ or *p*-chloranil similar to the Gross' method has been implemented. Perhaps the overall most efficient synthesis of free-base corroles was proposed by Koszarna and Gryko in 2006 - with a reported record yield of 32 %.[31] The method was remarkably innovative by reacting the aldehyde and pyrrole in an acidified water-methanol solution. The resulting open-chain tetrapyrrolic structure *bilane*, could from there be extracted and oxidized to corrole with DDQ or *p*-chloranil. This is arguably also the most used method for synthesis of free-base corroles until now.

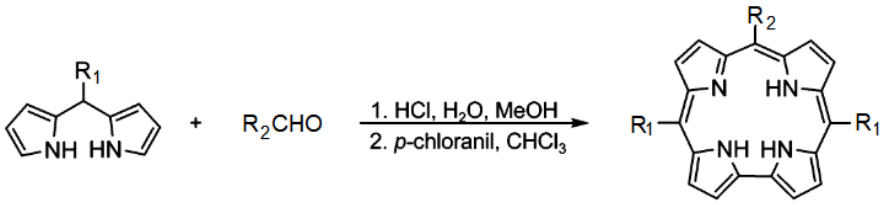

Figure 17. Synthesis of A_2B corroles proposed by Koszarna and Gryko in 2006.[31]

In the very same paper, Koszarna and Gryko proposed that the water method could also efficiently be used for synthesis of A_2B corroles, also named ABA corroles given the IUPAC numbering of the 5, 10 and 15 meso-positions. A_2B corroles were made from mixing two parts R_1-dipyrromethanes with one part R_2-aldehydes in an acidified water-methanol mixture. The A_2B bilane could then be extracted with chloroform and oxidized using *p*-chloranil to afford A_2B corroles in up to 56 % yield.[31] It is worth to note that calculated yield for non-A_3 corroles does not include the synthetic yield of the dipyrromethane.

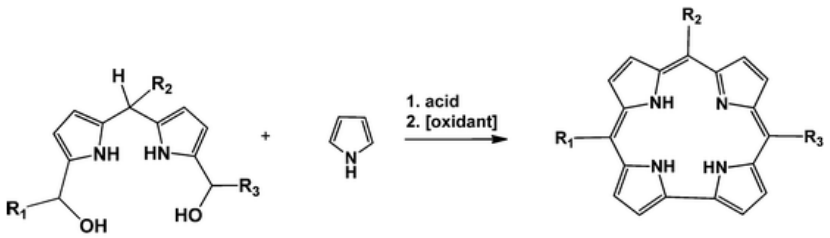

Figure 18. Synthesis of ABC corroles proposed by Geier and co-workers in 2004.[33]

The scientific interest in unusual free-base corroles also expanded to ABC corroles, where all three meso-substituents are different. A few synthetic routes towards the ABC corroles were proposed in the early 2000s - all with relatively different methods.[33] [34] [35] Paolesse and co-workers proposed the mixing of two different dipyrromethanes with one aldehyde. The reaction yielded not only ABC corroles, but also ABA and CBC corroles, which demonstrated the major difficulty with ABC corroles. However, Geier and co-workers proposed the use of dipyrromethanedicarbinols opposed to dipyrromethane, which establishes the ordering of the meso-substituents early in the synthesis - thus eliminating the ABA and CBC problematic.

2.3 Metallocorroles

2.3.1 Corrole Characteristics

The efficient synthetic routes of free-base corroles opened up the possibility of a scientific interest similar to when porphyrins were first synthesized, although to a much lesser extent. Corroles served as an undiscovered and novel porphyrinoid platform with interesting properties.

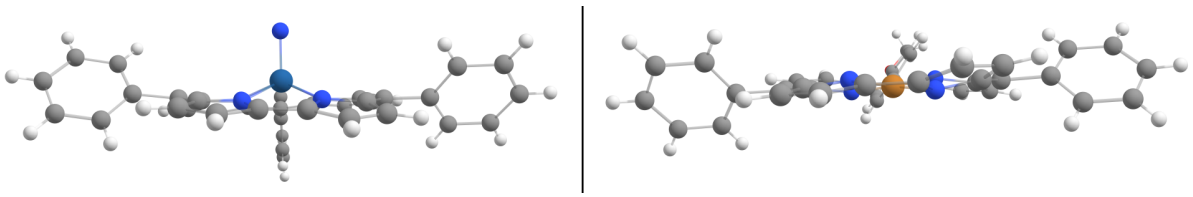

Figure 19. Examples of domed square pyramidal osmium-corrole[36] (left, DB identifier: LUMDON) and saddled square planar copper-corrole (right, DB identifier: POPTUL).[20]

Main physical differences of corroles compared to porphyrins is the trianionic structure, including the contraction of the N_4 cavity due to the lack of the fourth meso-position. Metalloporphyrins are often seen in an octahedral geometry as the porphyrin N_4 cavity is large enough to host many metals - on the contrary, corroles are often observed in square

pyramidal complexes as the N_4 cavity is often not large enough to host metals. It is therefore not uncommon to encounter slightly domed corroles, as it increases the orbital interaction with the central atom.

An example of significant geometric distortion in corroles are copper corroles, which are strongly saddled.[20] The saddling was found to be favorable in the example of the copper-corroles as the electron density of the HOMO could to a better extent overlap with the copper $d_{x^2-y^2}$ orbital - as a consequence, the copper was found to have a substantial Cu(II) character. The interaction between the copper and the corrole could therefore more accurately be described as $Cu^{II}[Cor^{\bullet 2-}]$, where the corrole bears the radical electron.

2.3.2 Ligand Innocence and Noninnocence

The phenomena of radical-bearing ligands are not unusual, and was first proposed over half a century ago as *ligand noninnocence*. It is not uncommon for the corrole ligand to exhibit the property of noninnocence - especially for first row metallocorroles, such as the known complexes of $Mn^{III}[Cor^{\bullet 2-}]Cl$, $Fe^{III}[Cor^{\bullet 2-}]Cl$ and $Cu^{II}[Cor^{\bullet 2-}]$. The corrole ligands which possess noninnocence are therefore best explained as partially oxidized, exhibiting a partial dianion-radical characteristic.

Corrole ligands involved in the metallobiscorrole framework are known to be innocent ligands, as they leave no doubt about the metal's oxidation state, which for the known molybdenum and tungsten metallobiscorroles are Mo^{VI} and W^{VI}. This means metallobiscorroles are respectively $4d^0$ and $5d^0$ species, meaning they would have to split a pair of lower energy electrons for the corrole ligand to become noninnocent. In contrast, $M^{V}[Cor]Cl_2$ (M = Mo, W) clearly demonstrated ligand noninnocence with a significant $M^{IV}[Cor^{\bullet 2-}]Cl_2$ character.[37] A rationale for the phenomena is the oxidation state of the central metal, as the Mo^{V} and W^{V} species are $4d^1$ and are thus perhaps more prone to give it away.

2.4 Corrole Coordination Chemistry

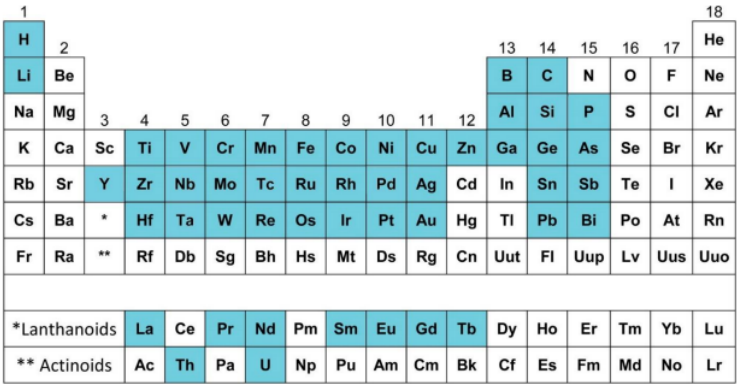

Figure 20. The periodic table of elements that are known to coordinate with corrole ligands. Reused with the permission of ref. 17.

Over the past 25 years, the elements known to coordinate with corrole ligands have been expanded to the vast majority of period 4, 5 and 6 transition metals and metalloids, s- and p-block elements, and multiple lanthanoids and actinoids. The contracted N_4 cavity of corroles has thus proven itself as a robust platform for coordination chemistry.

2.4.1 Coordination with Main Group Elements

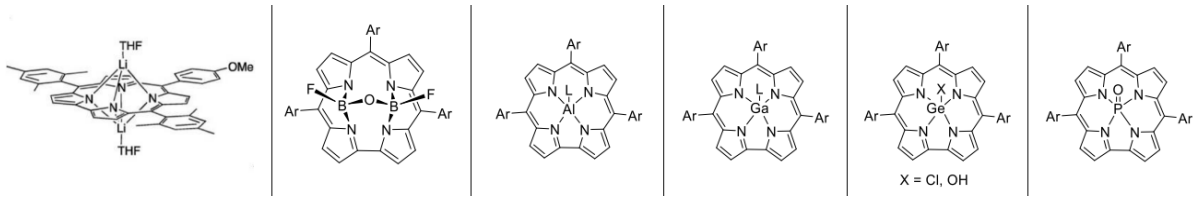

Figure 21. Some of the known corrole coordination complexes with s- and p-block elements.

Trivially, corroles coordinate with the s-block element hydrogen to form the free-base corrole. More interestingly, there has also been synthesized a lithium-coordinated corrole. The geometry can be depicted in Figure 21, with two lithium atoms sitting below and above the macrocycle plane.38 Additionally, several p-block elements have been coordinated to the corrole ligand. These mostly account for metalloids in period 13, 14 and 15 in the periodic table. Several of the known coordination complexes with metalloids can be depicted in Figure 21.

Most notably, is perhaps the diboron coordination chemistry, with both borons above the macrocycle plane bridged by an oxygen atom. There are in fact several known boron and diboron coordinated corrole complexes with a wide range of coordination motifs.39 Such

binuclear coordination motifs are much more common in porphyrins, and even more so in expanded porphyrins.[40]

Other heavier metalloids such as aluminium, gallium and lead, among others, have also successfully been coordinated to corrole ligands, usually seen in five coordinate complexes.[41] [42] [43] The scientific interest in p-block element corroles are primarily driven by their fluorescence properties, indicating that p-block element corroles could be applicable to bioimaging.

2.4.2 Coordination with Early d-Block Elements

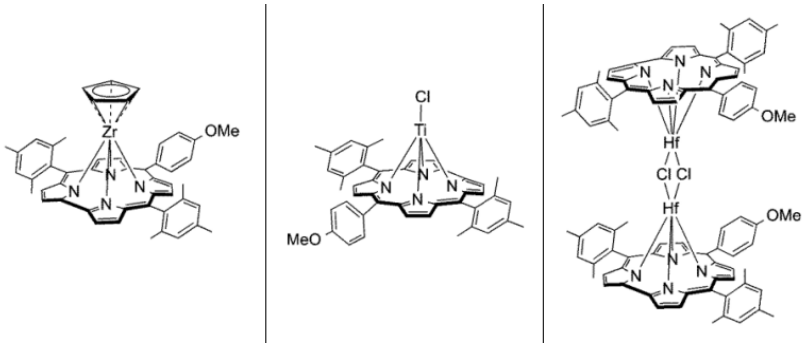

Figure 22. Some of the known corrole coordination complexes with early d-block elements.[44]

The field of early d-block elements coordinated to corrole ligands was primarily discovered by John Arnold and co-workers in the previous decade. As the atomic radius increases downwards and to the left in the periodic table, the early d-block metals are considered too large to fit in the contracted N_4 cavity of corroles. A clever method using the previously seen lithium corrole (Figure 21) reacted with early d-block metal salts was proposed to yield early d-block element corroles in high yields (41-79 %).[44] Similar to the lithium corroles, the early d-block elements were also five coordinate with the metal atom above the macrocycle plane - not surprising considering the atomic size of early d-block elements.

2.4.3 Coordination with Middle- and Late d-Block Elements

The majority of studied coordination chemistry with corrole ligands are performed on group 6 through 11 elements. Given that nature itself only inserts magnesium and period 4 transition metals into porphyrin coordination complexes, it is strongly suggestive of the favorance towards smaller coordination elements also (and especially) for corrole ligands. The middle and late d-block elements are significantly smaller than the early d-block elements found in group 4 and 5 - and are therefore more fit for corrole coordination chemistry.

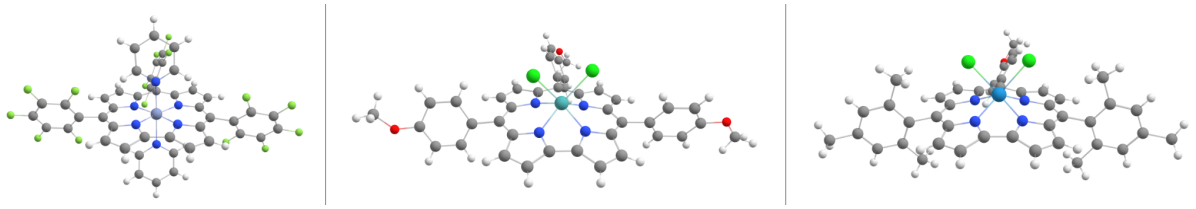

Figure 23. Examples of group 6 corrole coordination chemistry. Left: Chromium.[45] Middle: Molybdenum.[37] Right: Tungsten.[46]

Despite their sizes, all non-radioactive group 6 elements are known to coordinate with corrole ligands. Chromium, which is not much larger than other late d-block elements, is seen to fit inside the corrole N_4 cavity. The larger molybdenum and tungsten atoms however, are seen to be coordinated above the macrocycle plane due to their extensive size. Group 6 elements are commonly seen in complexes of high coordination due to their mostly unfilled d-orbitals. Notably, molybdenum, tungsten and very recently rhenium are the only elements found to yield biscorrole sandwich compounds.

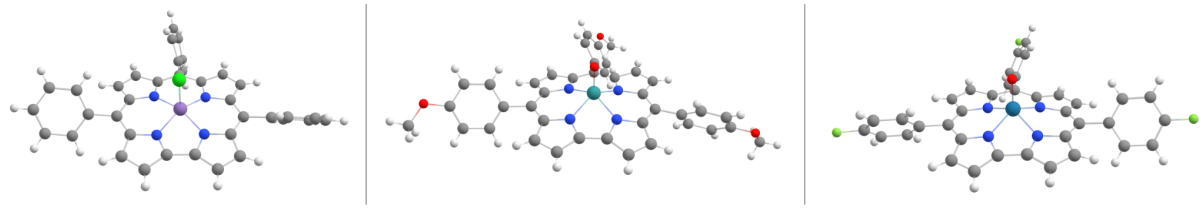

Figure 24. Examples of group 7 corrole coordination chemistry. Left: Manganese.[47] Middle: Technetium.[48] Right: Rhenium.[49]

Group 7 corrole coordination chemistry is also dominated by five coordinate complexes, as the size of technetium and rhenium are also considered too large for the N_4 cavity. Interestingly, the coordination complexes of rhenium corroles are quite complex - as oxidative metallation of free-base corrole with $Re_2(CO)_{10}$ under high heating produces a rhenium-rhenium quadruple bonded $\{Re[Cor]\}_2$ complex.[50] The same coordination motifs were found a few decades ago for molybdenum and tungsten in metalloporphyrins.[51] [52]

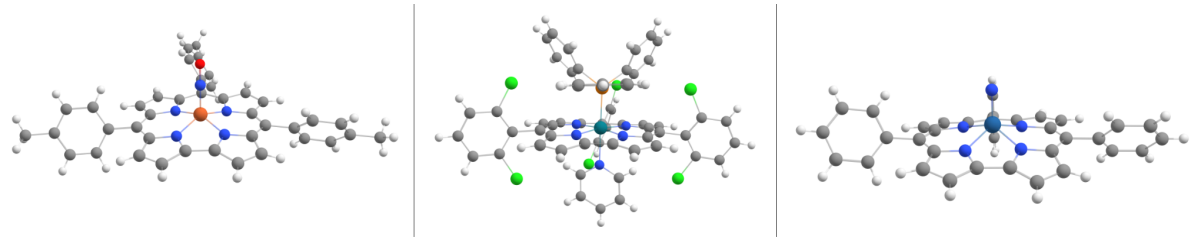

Figure 25. Examples of group 8 corrole coordination chemistry. Left: Iron.[53] Middle: Ruthenium.[54] Right: Osmium.[36]

Iron corroles are perhaps the most studied metallocorrole given the high biological interest of the analogous iron porphyrins. It is readily inserted into the contracted N_4 cavity of corrole given its smaller atomic size. Ruthenium, on the other hand naturally forms a ruthenium-ruthenium triple bonded $\{Ru[Cor]\}_2$ complex in the absence of other suitable ligands, much like the rhenium complex.[55] The very same dimerization happens also for osmium corroles when strongly heated in the absence of suitable ligands.[56] More interestingly, the non-dimerized osmium corroles exhibit near infrared phosphorescence and singlet oxygen sensitization.[36]

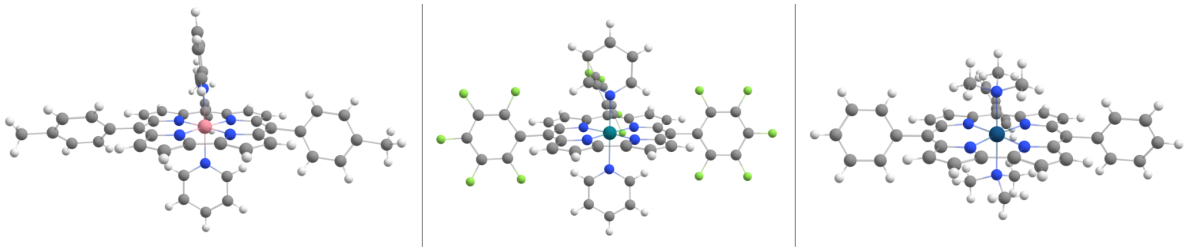

Figure 26. Examples of group 9 corrole coordination chemistry. Left: Cobalt.[57] Middle: Rhodium.[58] Right: Iridium.[59]

Cobalt corroles have, much like iron corroles, been thoroughly investigated due to the analogous cobalt corrin structure of vitamin B_{12}, which is of high biological importance. It is evident that as we approach smaller sized metals in group 9 and above, octahedral geometries start to dominate as the metal ion actually fits inside the corrole cavity - surprisingly also for iridium which belongs to period 6, and is therefore rather large. Rhodium corroles were also found to exhibit unusual coordination chemistry with corroles that were firstly refluxed with $COCl_2$ (phosgene). The carbon monoxide unit was found to coordinate with two of the cavity nitrogen. Upon addition of rhodium salts and PPh_3, the rhodium was found to coordinate with the remaining two cavity nitrogens without disturbance of the carbon monoxide unit.[58] Iridium corroles however, have been found to exhibit weak near infrared phosphorescence and strong singlet oxygen sensitization and thus may serve as a candidate platform for photodynamic therapy in the future.[59]

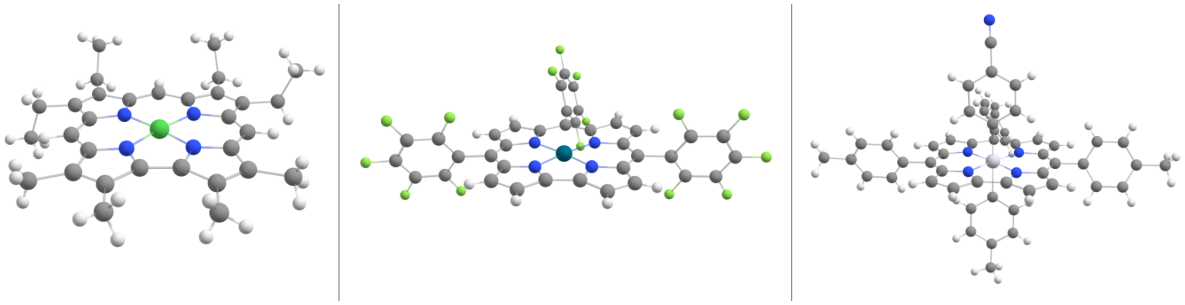

Figure 27. Examples of group 10 corrole coordination chemistry. Left: Nickel.[60] Middle: Palladium.[61] Right: Platinum.[62]

Free-base corroles reacted with nickel and palladium salts in the absence of other ligands were found to readily form square planar metallocorrole complexes. These complexes were some of the first metallocorroles investigated, but platinum corroles remained a mystery until a decade ago. Synthesis of platinum corroles was quite delicate, and involved microwaving free-base corrole and platinum salt in benzonitrile. Interestingly, the platinum liganded to one of the benzonitriles by C-H activation, instead of interacting with the nitrile group head-on. The platinum corrole was thus axially liganded with two benzonitriles, whereas one of them with the nitrile group, and the other with C-H activation of the benzo-ring. This complex was quite unstable, but the benzonitrile ligand which interacted with the nitrile group head-on was readily exchanged for *p*-toluene using aryl grignard reagent - yielding the first stable platinum corroles.[62]

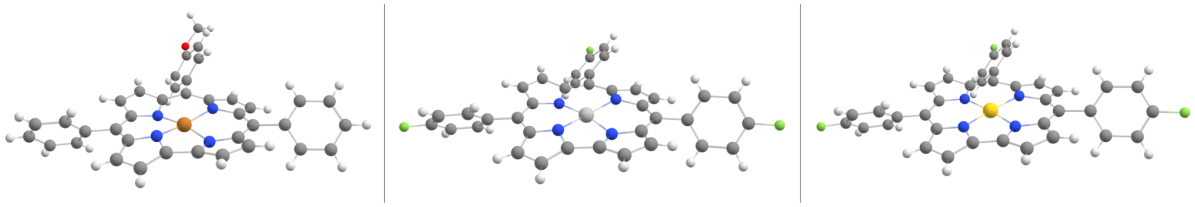

Figure 28. Examples of group 11 corrole coordination chemistry. Left: Copper.[20] Middle: Silver.[63] Right: Gold.[63]

Known metallocorroles of group 11 elements are found to highly distort the geometry of the corroles into a saddled geometry. The phenomena is induced by specific metal-corrole orbital interactions, which are increased in the order of Cu > Ag > Au, reflecting the large distortions of copper corroles compared to gold corroles. Copper corroles are also known to exhibit noninnocence, while this property progressively transitions into relative innocence for silver and gold corroles.[63]

Of group 12 elements, only zinc has been found to successfully coordinate with a radical corrole ligands.64 The group therefore remains underdeveloped - perhaps not caused by lack of scientific interest, but synthetic difficulty coordinating d^{10} elements to corroles.

3 UNUSUAL COORDINATION GEOMETRY IN METALLOCORROLES

3.1 Oxo-Bridged Metallocorroles

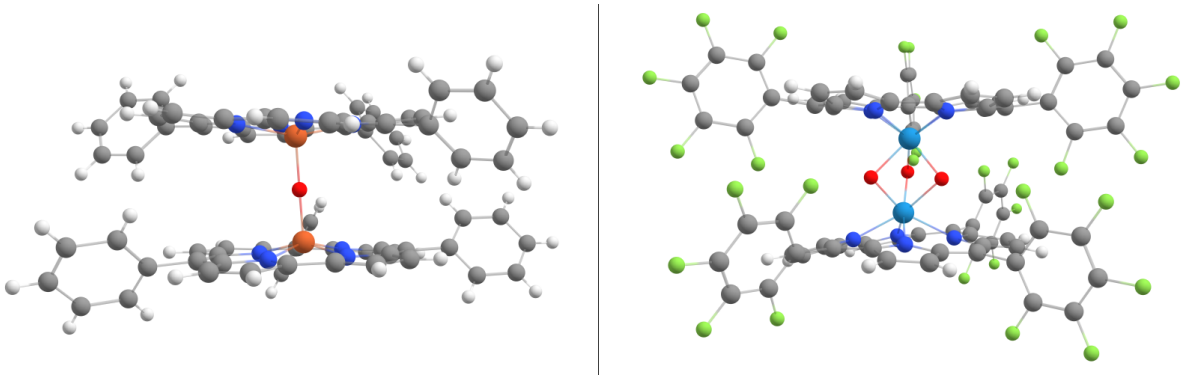

Figure 29. Two examples of μ-oxo bridged metallocorrole dimers. (Left65, DB identifier: MOTMOA. Right66, DB identifier: CAWVAZ).

Another common coordination motif in corrole chemistry is the μ-oxo bridged corrole dimers. Analogous complexes of metalloporphyrins have been thoroughly investigated due to the strong oxygen affinity displayed by metalloporphyrins. The μ-oxo bridged metalloporphyrinoids are commonly observed from reactions between some metal salts and free-base porphyrinoids in presence of high heat, sometimes treated with H_2O or a base. In fact, μ-oxo bridged corrole dimers are a major side-product of current biscorrole syntheses, where both high heat and base are present.

3.2 Dimeric Metallocorroles

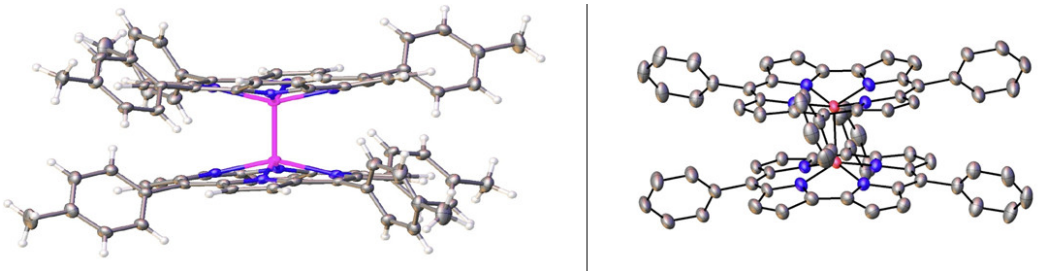

Figure 30. Two examples of dimeric metallocorroles. (Left50, DB identifier: ISUREW. Right56, DB identifier: YAQQOZ).

Dimeric metal-metal coordination motif in corrole chemistry has previously been mentioned as a product of oxidative metallation of corroles with ruthenium, rhenium and osmium. The

ruthenium metallocorrole dimer was first synthesized over 20 years ago[65], while the rhenium and osmium metallocorrole dimers are rather novel discoveries. Analogous coordination motifs in porphyrins have been known for many decades and are thoroughly studied.[66] [67]

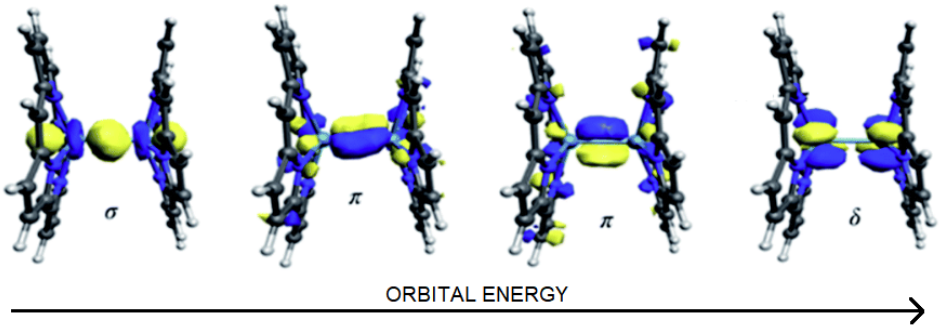

Figure 31. Kohn-Sham molecular orbitals of the $\{Re[Cor]\}_2$ complex. Reused with the permission of ref. [66].

Bond length, diamagnetism and DFT calculations suggested that the dimeric rhenium metallocorroles possessed a $\sigma^2\pi^4\delta^2$ metal-metal quadruple bond. In contrast, the dimeric group 8 ruthenium and osmium metallocorroles were found to possessed a $\sigma^2\pi^4\delta^2\delta^{*2}$ metal-metal triple bond.

3.3 Sandwich Metallocorroles

3.3.1 An Introduction

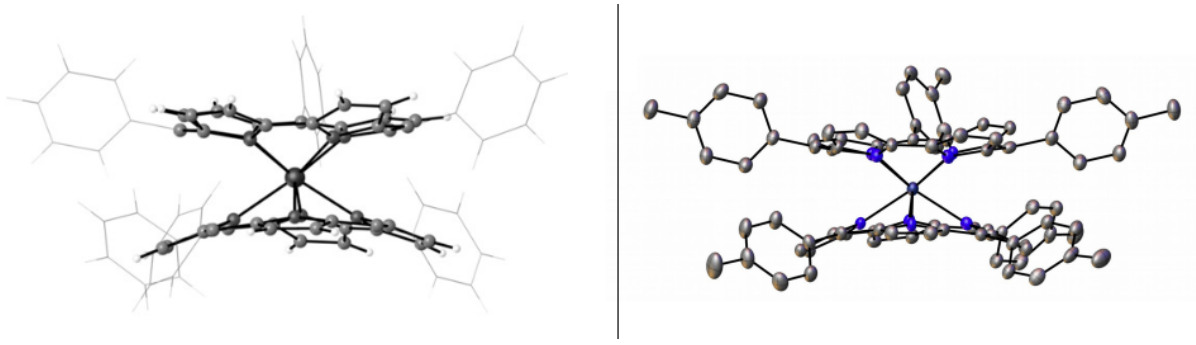

Figure 32. Examples of eight-coordinate sandwich metallocorroles. (Left[68], DB identifier: OKIJID. Right[69], DB identifier: HAPVEC).

The first eight coordinate biscorrole structure was discovered in 2016 - by accident. Reaction conditions analogous to the ones used to prepare $Os^{VI}N$ corroles were used with the exception of $W(CO)_6$ instead of $Os_3(CO)_{12}$.[56] [68] The reaction did however, not yield the

desired $W^{VI}N$ corrole (nor the tungsten biscorrole), and the solvent was changed from diethylene glycol monomethyl ether to decalin. Upon changing the solvent to decalin, the desired tungsten product was again not detected, but a compound with the mass consistent of a tungsten biscorrole was found. The original reaction conditions contained NaN_3 to induce a nitrogen ligand as the fifth coordinate, but was excluded as the focus shifted towards the newly discovered eight coordinate biscorrole sandwich compound.[68]

Soon afterwards, the success was also expanded to molybdenum biscorroles under identical reaction conditions. Perhaps not surprisingly as both tungsten and molybdenum are group 6 metals, but chromium biscorroles are however still unknown. Very recently, rhenium biscorrole sandwiches with a unique coordination motif were also discovered. The rhenium biscorroles are thought to be seven coordinate with one macrocycle proton still remaining - however, the proton could readily be removed upon treatment with a base.[70]

The major difficulty among all the discussed metallobiscorroles was the electronic interpretation, as the ^1H nuclear magnetic resonance spectroscopy proved to not be enlightening, with broad and overlapping peaks in the aromatic region. Variable temperature ^1H NMR spectroscopy also failed to shed light upon the electronic structure of metallobiscorroles. A major motivation in this thesis was therefore to make improvements in our understanding of the electronic structure of metallobiscorroles, and hopefully generate at least one assignable ^1H NMR spectrum.

3.3.2 Synthesis and Purification

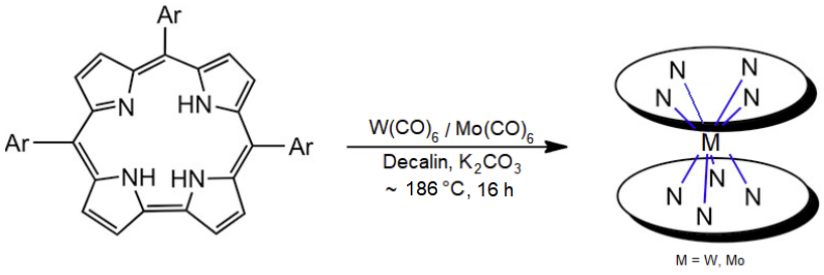

Figure 33. Synthetic route used for the first tungsten and molybdenum biscorroles.[68] [69]

The reaction conditions were changed to an interaction between *para*-substituted *meso*-triarylcorroles and $M(CO)_6$ (M = W, Mo) in refluxing decalin overnight at 186 °C, in an inert argon atmosphere using potassium carbonate as a base. The reported yields of tungsten biscorroles were 12-18 %, while the reported yields of molybdenum biscorroles

were 25-30 %. In oxidative metalation reactions, a suitable base is essential to pick up and neutralize the inner protons of the corrole - increasing the nucleophilicity of the corrole cavity.

Completion of the reaction was indicated by disappearance of the characteristic ~420 nm Soret band of free-base corrole, and an appearance of a new Soret band of ~360 nm. To remove the high boiling point solvent, the reaction mixture was eluted with hexane in a silica gel column. Afterwards, the biscorrole sandwich could be eluted with 3:2 n-hexane:dichloromethane, and all fractions with a Soret band of ~360 nm were collected. The collected fractions were then purified in another silica gel column, before lastly being purified with preparative thin-layer chromatography.

The synthesis and purification of tungsten and molybdenum *para*-substituted *meso*-triarylbiscorroles were thus established in respectable yields using the oxidative metalation protocol under high heat.

3.3.3 Symmetry and Chirality

Similarly to much of the other corrole chemistry, the discovery of metalloporphyrin sandwich complexes was decades old before it was reproduced with the corrole ligands. A particularly interesting difference of the corrole and porphyrin sandwich complexes is the tris (5, 10, 15) versus tetrakis (5, 10, 15, 20) meso-substitutions. As the tetrakis metalloporphyrin sandwich complexes possess an inability to form other stereogenic sandwich complexes under the square antiprismatic framework due to the high symmetry of the porphyrin ligands. On the other hand, metallocorrole sandwich complexes are highly dependent on the relative rotation of the corrole-corrole offset angle - which gives rise to two possible diastereomeric units.

Interestingly, the biscorrole sandwich compounds serve as a novel class of *inherent* chiral chromophores[71] [72] and the structures correspond to C_2 symmetry. Chirality is normally induced by a stereogenic center, which is bound to all different atoms or groups and thereby loses all its symmetry. Biscorroles however, do not possess such a stereogenic center, but still remain chiral. The inherent chirality in biscorroles is induced by the overall molecular geometry, known as either planar or axial chirality. Whether biscorroles are best described as planar chiral or axial chiral is debatable as they seem to fit both - the best description is therefore the collective term inherent chiral.

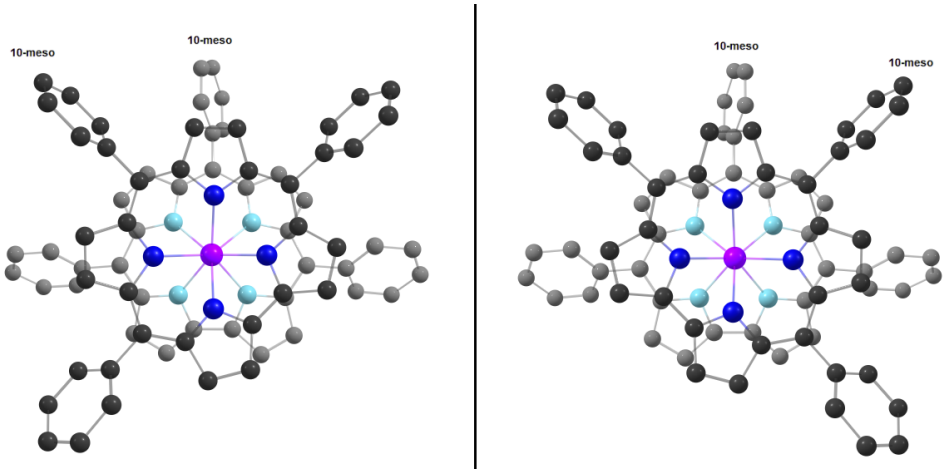

Figure 34. Top view of *meso*-triarylbiscorrole enantiomers. Hydrogens are omitted and the corrole units are shaded differently for visual reasons.

The molecular inherent chirality becomes evident as the biscorrole is mirror-planed. Each diastereomer thus possesses a pair of enantiomers as depicted in Figure 34. In addition to the corrole's rich photophysical properties, inherent chiral biscorroles may very well serve as a potential platform for chiral sensing, nonlinear optical materials or chiral liquid crystals.

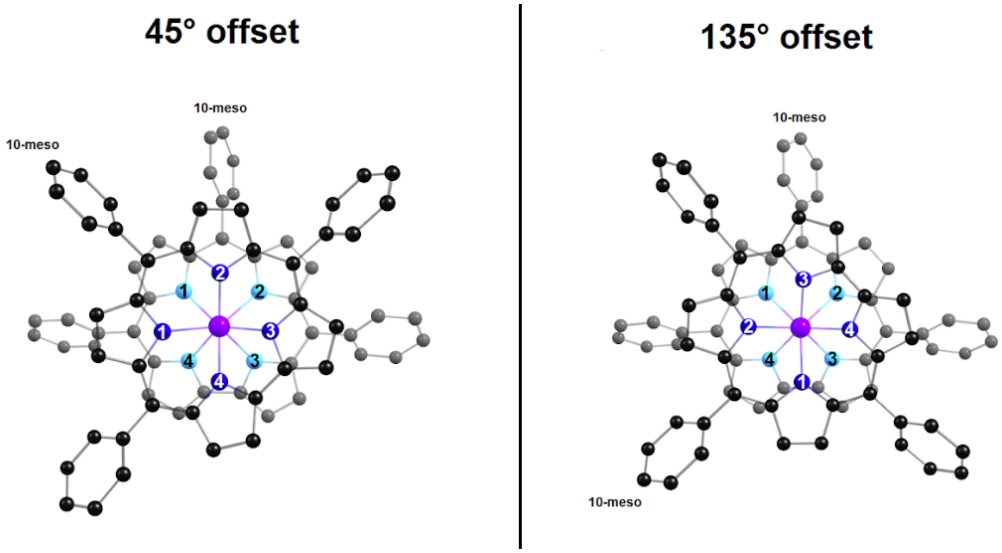

Figure 35. Top view of *meso*-triarylbiscorrole diastereomers. Hydrogens are omitted and the corrole units are shaded differently for visual reasons, including nitrogen numbering to display rotation.

As the eight coordinate square antiprismatic motif can be achieved in two distinct ways, biscorroles were believed to form two diastereomeric units, supported by density functional theory calculations suggesting they should be approximately equal in terms of ground state

energy. The doubly stereogenic units are best described using the relative corrole-corrole offset angle looking at the 10-meso positions, which corresponds to approximately 45° and 135°, as depicted in Figure 35. This doubly stereogenic behavior was although never observed, and the solved crystal structures only contained the 135° diastereomer.

This meant that not only could one reaction mixture contain two enantiomers, but it could contain two diastereomers - both possessing two enantiomers. The purification and analytic work thus grows rapidly in difficulty as this has to be taken into consideration.

Table 1. General degeneracy of analytical methods for enantiomers and diastereomers.

	UV-Vis	NMR	MS
Enantiomers	✔	✔	✔
Diastereomers	×	×	✔

As seen in Table 1, enantiomers are generally degenerate using spectroscopic methods such as UV-Vis, NMR and MS - with the exception of vibrational circular dichroism. Diastereomers however, can and usually will possess spectroscopic differences for both NMR and UV-Vis. They can also possess differences in electric dipole moment, leading diastereomers to potentially be separated by chromatography.

3.3.4 Theoretical Interpretation

As the discovery of biscorroles led to a completely new coordination motif in corrole chemistry, the systems were thoroughly investigated using computational methods. Scalar-relativistic density functional theory calculations were used to search for the ground state geometry of the biscorrole sandwich structure. The theoretical method accurately predicted the square antiprismatic geometry of the central atom, with an energetic favorance of 2.2 eV compared to the square-prismatic geometry. Square antiprismatic biscorroles were therefore proposed to be configurationally stable, and not capable of converting between geometries due to a large energetic rotational barrier of the relative corrole-corrole rotation.

The geometric calculations also suggested a very slight favorance of <0.1 eV towards the 135° diastereomer compared to the 45° diastereomer. This would suggest that both diastereomers should be experimentally observed in approximately equal proportions if there were no rotationally dependent intermediates, which seems rather unlikely, although no reaction mechanisms for the formation of metallobiscorroles have been proposed.

Time-dependent DFT calculations were used in an attempt to understand the electronic transitions responsible for the unique UV-Vis spectra with λ_{max} of ~360 and ~780 nm. The λ_{max} of ~360 nm was attributed to a series of transitions to high-energy unoccupied molecular orbitals, such as transitions to LUMO+5 and LUMO+6. On the other hand, the near-IR λ_{max} of ~780 nm was attributed to a ligand-metal charge transfer transition, almost entirely consisting of HOMO-1 to LUMO transition.

4 THEORETICAL AND DYNAMIC NUCLEAR MAGNETIC RESONANCE SPECTROSCOPY

In the following chapter, I have chosen a rather explicit and pedagogical approach as I think that there exist many skilled chemists who have not been subject to unusual anisotropic effects or dynamic NMR, and therefore do not possess a theoretical understanding of the processes which are key to a major part of the thesis. My motivation is thus to walk the readers carefully through the most critical aspects required to understand both anisotropic and dynamic effects in NMR.

4.1 Fundamental NMR Spectroscopy

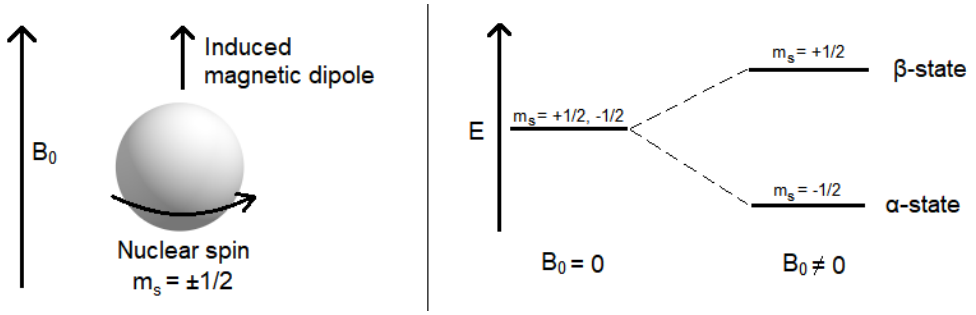

Figure 36. Principles of NMR spectroscopy and the Zeeman effect in an external magnetic field B_0.

Nuclear magnetic resonance spectroscopy begins when nuclei of certain sorts possess a quantum property of spin with ±½. A spinning charged nucleus generates a magnetic dipole, and in the presence of an external magnetic field (B_0), the induced magnetic dipoles can either align with or against the external magnetic field. The spin-state with the induced magnetic dipole aligned with the external magnetic field is lowered in energy, and hereby called the α-state. Similarly, the β-state denote the spin-state with the induced magnetic dipole aligned against the external magnetic field, and is therefore raised in energy.[73]

The energy gap between the α- and β-state can be attributed to the Zeeman effects:

$$\Delta E = h\nu = \frac{h\gamma B_0}{2\pi} \qquad \text{Eq. 1}$$

Where γ is the gyromagnetic ratio of the particular nucleus, h is Planck's constant and B_0 is the external magnetic field. Intuitively, in the absence of an external magnetic field ($B_0 = 0$),

the energy gap between the spin-states is zero. Similarly, a higher external magnetic field causes an increase in energy splitting between the spin-states - effectively increasing the spectroscopic resolution.[73]

Commonly studied nuclei in NMR are ^{1}H, ^{13}C, ^{19}F and ^{31}P. What they have in common is their odd mass numbers with spin numbers of ±½ - generating the magnetic dipole. Another nucleus of great interest is the ^{15}N, but the low natural abundance in addition to its low gyromagnetic ratio makes it essentially impossible to study unless the samples are enriched. ^{13}C NMR faces the same, but less severe difficulties, making its signal to noise ratio approximately four orders of magnitude lower than ^{1}H NMR.[73]

Other spectroscopic methods such as UV-Vis or IR have the advantage of studying chemical phenomena often in the range of 1-100 kcal/mol. NMR on the other hand, even with a well-equipped 500 mHz NMR spectrometer, only studies chemical phenomena in order of 5×10^{-5} kcal/mol. The sensitivity required to study such phenomena in NMR is therefore on a whole other level of theory compared to other spectroscopic methods.

The low energy is not only quantitatively difficult to measure, but also manifests itself in the population of spin states given by the Boltzmann distribution.[74]

$$\frac{N_\beta}{N_\alpha} = e^{-(\frac{\Delta E}{RT})} \qquad \text{Eq. 2}$$

Where N_α and N_β are the population of spin states, R is the Boltzmann constant and T is temperature in Kelvin. The energy term ΔE, is found in Eq. 1, and essentially brings the exponent of Eq. 2 close to zero - making the population of spin states N_α and N_β exceedingly close to equal. As a result, in the example of ^{1}H NMR in room temperature at 500 mHz - only 81 of 2 million protons are unequally distributed and are therefore susceptible to generate a NMR signal.[74]

It is therefore evident why NMR spectroscopy took much longer to develop than other spectroscopic methods. The combination of extreme sensitivity required to measure such small energy differences, and the exceedingly equal population spin states, makes NMR spectroscopy an incredibly insensitive method in comparison with other methods. On the other hand, NMR spectroscopy serves as perhaps the most versatile analytical method in chemistry as it gives extremely detailed descriptions of three-dimensional structural

confirmation, elucidation, determination, dynamics, among other highly important analytical aspects that arise from chemical shielding. [74]

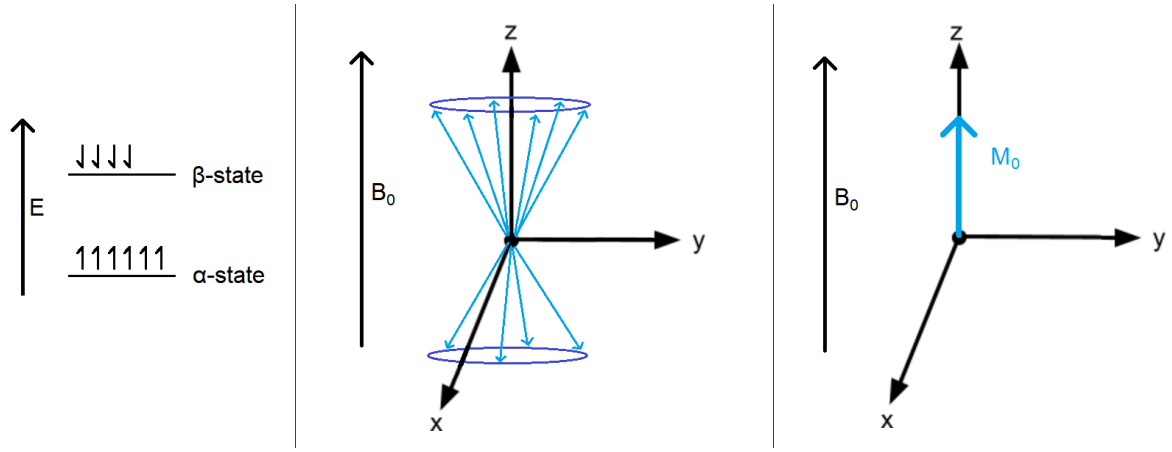

Figure 37. Representation and visualization of different spin states, including the net magnetization vector (M_0).

An ensemble of nuclei in presence of an external magnetic field (B_0) have been depicted to populate two different spin states, α- and β-state. The α-state is oriented along the external magnetic field, and is therefore lowered in energy compared to the β-state which is oriented against it and as a consequence raised in energy. Figure 37 depicts the situation, but is *grossly* overestimated in terms of the population between the two spin states - for a more accurate description, an ensemble of 2 million nuclei should be represented with a total of 81 of them being unequally distributed in the α-state.[73]

The individual nuclei spin around the z-axis at its Larmor frequency, which is a different frequency for every species. After accounting for a uniform distribution of spin states around the precession angle, a net magnetization vector (M_0) is aligned in the direction of the external magnetic field, in this case the z-axis. The net magnetization vector is in fact incredibly small considering its the sum of unequally distributed spin states.

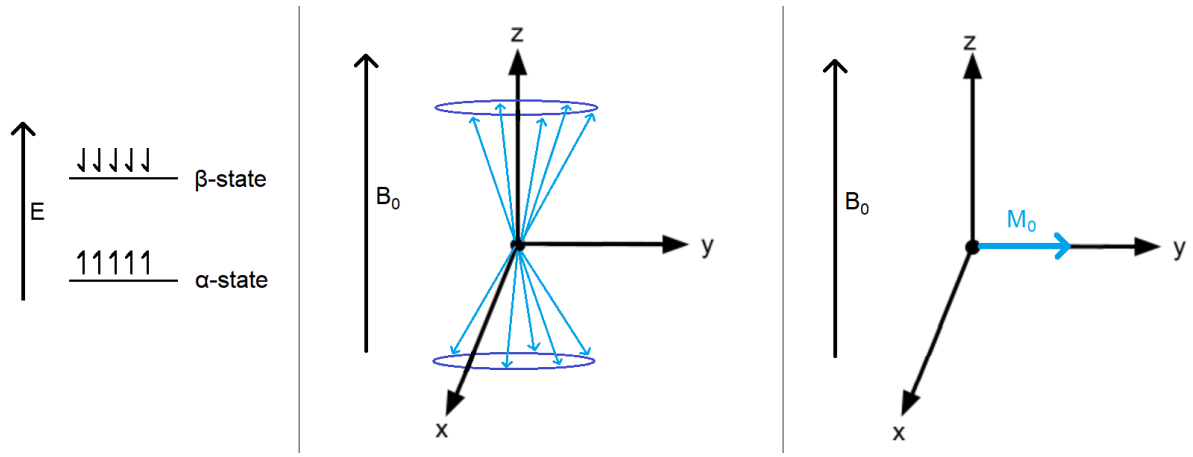

Figure 38. Representation and visualization of different spin states, including the net magnetization vector (M_0) after a 90° radiofrequency pulse is applied.

Fundamental generation of NMR signal lies in perturbations of the unequally populated spin states to generate equally populated spin states - and thereafter measuring the relaxation as the system goes back to the unequally populated spin states. The perturbation of the spin states happen through a radiofrequency (RF) pulse, often applied perpendicular to the external magnetic field. As a result of the perturbation, the α- and β-state comes equally populated as the net magnetization vector becomes perpendicular to the external magnetic field.[73]

As the RF pulse vanishes, the external magnetic field drives the system back to its natural unequally populated spin states - also called relaxation, more specifically longitudinal T_1 relaxation. The net magnetization vector will then rotate around and towards the z-axis, before it finally collapses and the system becomes completely relaxed. It is exactly the relaxation process of the net magnetization vector that generates the NMR signal as an electric current which is induced by the rotation, also called free induction decay. The electric current is then picked up and amplified, before digitized and further processed in a computer.

4.2 Chemical Shift

Chemical shift is the foundational measurement in NMR spectroscopy, generated by the spin precession of nuclei at certain frequencies. It can be seen as a fingerprint of the electronic environment around the nuclei. As for ^{1}H NMR, tetramethylsilane (TMS) is used as the reference, effectively resonating 300 million cycles per second in a 70500 Gauss magnetic field. A 70500 Gauss spectrometer would therefore be named *300 mHz*, as the naming convention is dependent on the resonant frequency of TMS - this is however a misleading naming convention for other nuclei such as ^{13}C which have a resonant frequency

approximately ¼ of ^{1}H. The resonant frequency is linearly dependent on the magnetic field strength, which establishes the relationship of higher resolute spectra for stronger magnetic fields.[74]

As an example, the chemical shift of methyl groups are often observed in the ~1 ppm region in NMR spectroscopy, which effectively means the ^{1}H nuclei of a methyl group are resonating an additional 300 cycles per second compared to TMS in a 300 mHz NMR spectrometer - a strikingly small difference. This attests to the insensitivity of NMR spectroscopy, where even the most contrasting ^{1}H nuclei such as aldehydes and methyls are only separated by a few thousands hertz on the grand scale of 300 mHz.

The chemical shifts are dependent on the electronic environment around the particular nuclei, and are therefore strongly influenced by changes to the system that perturb nearby electron density. As electrons oppose the applied magnetic field, nuclei located in electron rich environments will perceive less of the applied magnetic field, resulting in a lower chemical shift.

Table 2. ^{1}H chemical shift of methyl halides including the halide's electronegativity.[75] [76]

Compound	Chemical shift ppm	Electronegativity
CH_3I	2.2	2.7
CH_3Br	2.7	3.0
CH_3Cl	3.1	3.2
CH_3F	4.1	4.0

Methyl halides provide a good demonstration of how chemical shift is influenced by the electronic environment. As the electronegativity of the halogen increases, the methyl carbon becomes progressively more electron deficient. This leads to the methyl hydrogens being less electronically shielded, thus perceiving more the external magnetic field causing an increase of chemical shift.

4.3 Anisotropic Effects

With the exceptions of highly symmetrical and simple systems, anisotropic forces are in play during NMR spectroscopy. Anisotropic forces are very often overlooked, as most of the effects are simply included in chemical shift tables. Arguably, the most common example includes the aromatic region of ^{1}H NMR - where most chemists know that aromatic signals

generally show up in the ~7-8 ppm region, but have little idea of the nature behind the chemical shifts of the aromatic protons.

As the external magnetic field is only applied in *one* direction, the orientation of the molecules with respect to the external magnetic field becomes interesting for certain molecules. In reality, the individual molecules are rapidly tumbling around in solution, effectively averaging the chemical shift anisotropy into one distinct signal referred to as the isotropic chemical shift.

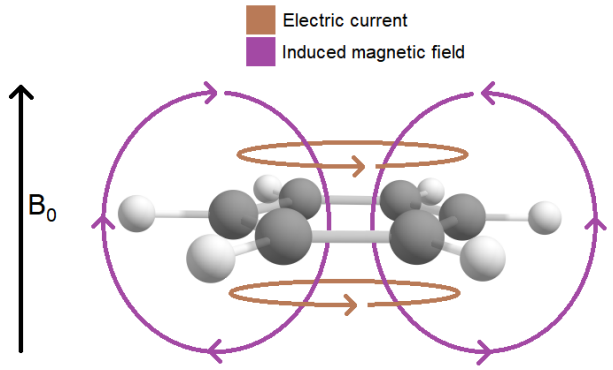

Figure 39. Visualization of anisotropic effects generated in benzene in an external magnetic field.

Aromatic systems in particular have a fascinating nature when exposed to external magnetic fields. The aromaticity allows the electrons to flow freely in a conjugated system of π-orbitals. When exposed to an external magnetic field, the aromatic electrons are compelled to move in a circular direction to generate an electric current around the aromatic system. Electrons can be seen as moving charged particles, which in turn creates its own induced magnetic field. The induced magnetic field generated by the aromatic electron flow will always oppose the external magnetic field. As seen in Figure 39, the inside core of a benzene molecule is therefore highly shielded, as the perceived net magnetic field will be lower than the external magnetic field. In contrast, the outside of the benzene ring is highly deshielded as the perceived net magnetic field is greater than the external magnetic field. As most aromatic hydrogens happen to lie in the deshielded region of aromatic systems, the general consensus is therefore that aromatic protons are found in the ~7-8 ppm region.[73]

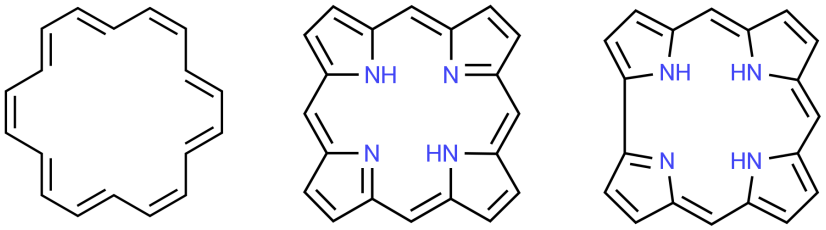

Figure 40. Aromatic systems with highly shielded internal protons.

There are however aromatic systems that contain internal protons in the highly shielded region, such as cyclooctadecanonaene, porphine and corrole as depicted in Figure 40. The larger aromatic systems act similarly to the benzene depicted in Figure 39 when exposed to an external magnetic field - resulting in a shielded internal region of the system. Hydrogens located in the internal region are therefore so highly shielded they commonly appear with negative ppm values with respect to TMS.

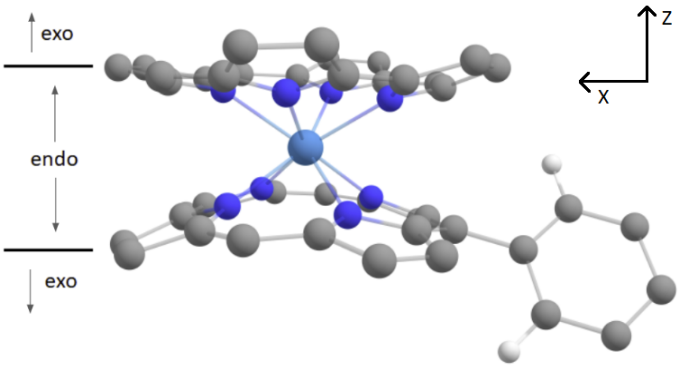

Figure 41. Biscorrole with substituents omitted for clarity, showing two *o*-phenyl hydrogens and exo- and endo-regions.

Interestingly, the biscorrole framework is believed to possess very different magnetic environments between the endo- and exo-regions. The endo-region of the biscorrole scaffold is thought to be exceptionally deshielded as the anisotropic magnetic field from both corrole moieties will act in conjunction. In contrast, the exo-region is thought to be less deshielded than normal aromatic systems as it is out of plane of the aromatic corrole moiety. As a result, the *o*-phenyl protons in biscorroles are proposed to be largely separated under ^{1}H NMR for non-rotating phenyl groups. Whether the biscorrole scaffold acts as one large aromatic system or two individual aromatic systems under an external magnetic field is still unknown, but the outcome would be consistent considering the directionality of the induced magnetic field.

4.3.1 Aromatic Solvent Induced Shifts

Overlapping and unsolvable NMR spectra can sometimes be significantly improved by introduction of aromatic solvents. The aromatic solvent induced shifts (ASIS) are caused by the anisotropic effects as the molecules of interest are solvated and often delicately coordinated with the aromatic solvent.

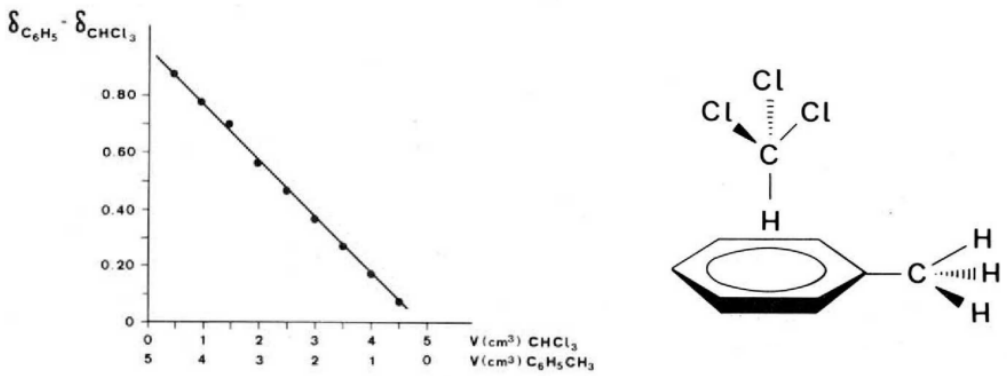

Figure 42. Variations of the chemical shift in ppm with relative proportions of toluene and chloroform, including the proposed toluene/chloroform “coordination complex”. Reused with the permission of ref. 77

NMR spectra of toluene and chloroform in different proportions serves as an empirical demonstration of the ASIS, where the hydrogen on the chloroform is coordinated directly above the electron-rich toluene core - resulting in progressively more shielded hydrogens as the toluene concentration is increased. The chemical shift of chloroform was found to decrease from 7.23 to 5.86 as the concentration of toluene was increased from 10 to 90 %. 77

On a general basis, aromatic systems are well known for being electron-rich, thus readily interacting with electropositive sites such as hydrogens. The highly shielded aromatic core is therefore pointed directly towards particular sites of the molecule of interest, and therefore influencing the perceived magnetic field.

It is however an overstatement to imply that these coordinating forces are strong enough to be present for every molecule in solution - but if they were, the chemical shifts would have extreme deviations in the order of several ppm upon changing to an aromatic solvent. It is therefore important to remember the extremely large ensemble of molecules present in an NMR sample, which collectively produce an average isotropic chemical shift. The statistical

distribution of spatial coordination states between the aromatic solvent and molecule of interest thus plays an important role.

4.4 Dynamic NMR Spectroscopy

Longitudinal T_1 relaxation times in NMR spectroscopy are often in the order of milliseconds to seconds time scale. In a chemical sense, the time frame may be perceived as an eternity with respect to the individual molecular motion such as translation, vibration or rotation. It is therefore evident that the generated NMR signals must be the average over countless molecular configurations. There are however some molecular processes which are sufficiently slow to be observed in the NMR time scale. Such molecular processes often involve conformational changes or strained bond rotation caused by either steric hindrance or electronically by partial double bond character. Dynamic NMR spectroscopy therefore covers the investigation of observable and reversible molecular processes which cause changes in the chemical shift. It is often associated with temperature-dependent NMR spectroscopy, as these molecular processes are generally highly temperature-dependent.

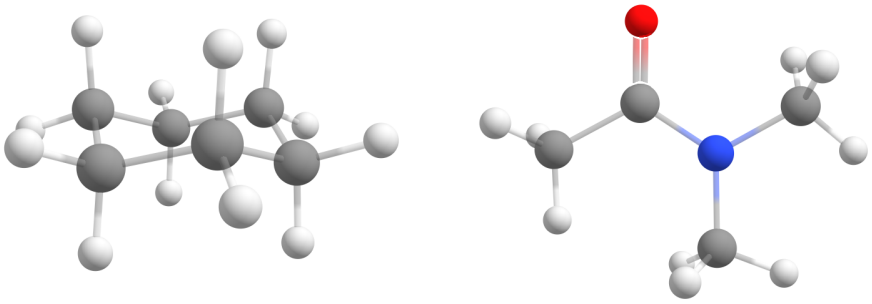

Figure 43. Example of molecules which possess observable dynamic NMR processes.

Most commonly, cyclohexane has been known for decades to undergo a ring inversion. The ring inversion goes through multiple transition states, with the largest energetic barrier of approximately 11 kcal/mol from chair conformation to half-chair conformation.[78] Room-temperature ^{1}H NMR produces one degenerate signal at 1.43 ppm - consistent with the chemical shifts for secondary alkanes with a uniform electronic environment.[75] However, the axial and equatorial hydrogens are certainly not in an uniform electronic environment. The room-temperature ^{1}H NMR therefore suggests a rapid ring inversion, effectively moving each individual hydrogen between two electronic environments sufficiently fast to be detected as one degenerate signal. Interestingly, the ring inversion can be slowed down to produce two distinct signals in ^{1}H NMR at temperatures below 240 K, where the axial and equatorial hydrogens are no longer degenerate.[79]

Amides such as N,N-dimethylacetamide depicted in Figure 43, are commonly studied using dynamic NMR spectroscopy as the carbon-nitrogen bond is partially restricted from rotation. At first glance, the carbon-nitrogen bond might seem completely free for rotation, but in reality the bond has a partial conjugated π-bond character as the amide group allows for two resonance structures. Rotation about the carbon-nitrogen bond is therefore sufficiently slowed in room temperature to produce two distinct signals in ^{1}H NMR (excluding the methyl group bond to the carbonyl carbon), as one of the methyl groups is in proximity of the carbonyl oxygen which gives peripheral chemical shielding. The energetic barrier for rotation of common amides are generally observed in the range of ∽16-18 kcal/mol. As most amides already produce two distinct signals at room temperature, the sample must be heated to observe the dynamic behavior. Upon heating N,N-dimethylacetamide above 340 K, the two distinct signals become one degenerate signal as the carbon-nitrogen bond starts rotating rapidly.[80]

4.4.1 Fast Fourier Transforms

Fourier Transform is arguably the most important algorithm of all time, and it was invented in 1805 by the French mathematician Jean-Baptiste Joseph Fourier. Today, Fourier transforms are highly abundant in modern life as most technological devices and applications utilize it. It is best known as an immensely powerful mathematical tool used to transform signals between time- and frequency-domains. The earlier version of the Fourier transforms suffered from a high computational scaling of N^2, where N is the number of discrete data points. Although the signal may be continuous, a partitioning into discrete data points has to be done at some point during digitalization. A major breakthrough came in the 60's by the American mathematicians James Cooley and John Turkey, as the Fast Fourier transform (FFT) was invented. The FFT exploited the symmetry of sinusoidal functions to skip redundant data points - thus reducing the computational scaling to $N\log_2 N$.[81]

Early days NMR spectroscopy was often done by slowly sweeping every frequency of the spectrum. This was done to reduce the complexity of the signal output as there were no available tools to interpret such outputs. In modern NMR machines however, the entire frequency spectrum is generated by a single radiofrequency pulse as the complex output signal is effectively transformed into the frequency-domain with the use of FFT.[82]

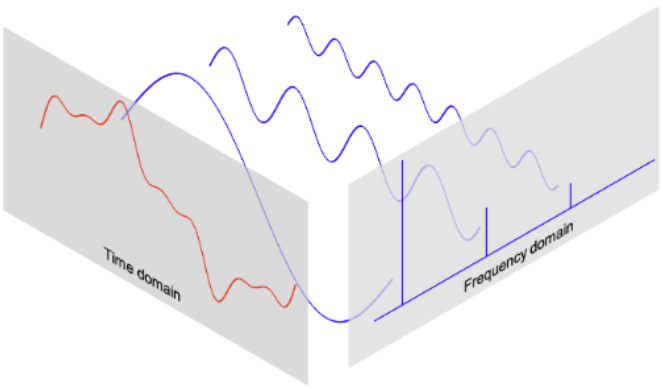

Figure 44. Illustration of three sinusoidal waves in the time- and frequency domain.[83]

Signal processing in the time domain can be quite complicated, as the composition of just three sinusoidal wave functions as depicted in Figure 44 makes the domain essentially impossible to interpret. The frequency domain however, is seen to be a much more preferable domain to interpret the sinusoidal functions. Similarly, the FFT in NMR spectroscopy receives the free induction decay signal in the time domain, and transforms it into the frequency domain where the user effectively reads the chemical shift.

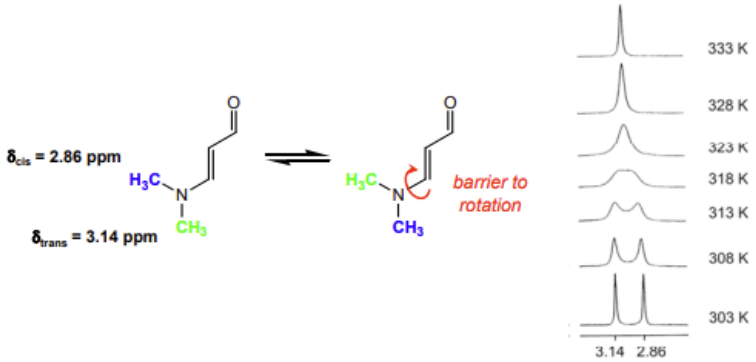

Figure 45. Dynamic NMR spectroscopy of 3-dimethylaminoacrolein.[84]

Dynamic NMR spectroscopy in combination with the discretization of FFT gives rise to interesting effects observed in NMR spectra. In room temperature, the methyl groups bound to the amino-nitrogen gives rise to two separate signals as the exchange between the δ_{cis} and δ_{trans} states are sufficiently slow. As the exchange rate increases with temperature, the rate of exchange hits *coalescence* at 318 K where FFT is no longer able to distinguish the difference in frequencies. A further increase in temperature produces a sharp uniform signal as the methyl groups are seen as equivalent on the NMR timescale.

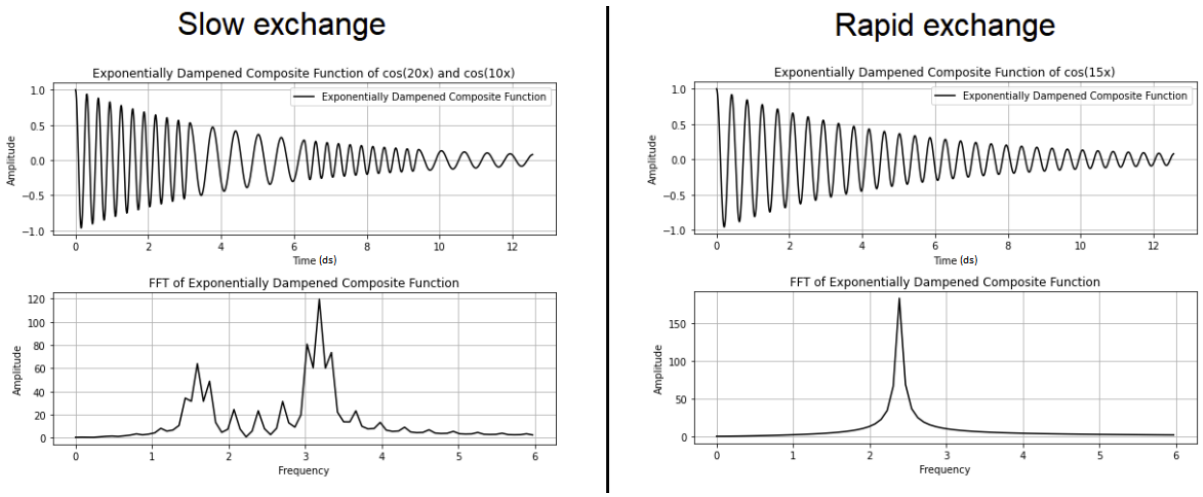

Figure 46. Illustration of NMR free induction decay of a single nucleus under slow and rapid exchange processes, including their respective Fourier transforms. Own work, Appendix 800.

Importantly, Figure 46 depicts the behavior of a single spin nuclei, e.g. a single hydrogen under ^{1}H NMR. In combination with the exponential decay of the signal, this gives rise to the artifact of the asymmetry of the FFT for slow exchange, which would otherwise be averaged out in a sample with millions of hydrogens. Aside from that, Figure 46 serves as an overall demonstration of the free induction decay which is generated from every single nuclei under both slow and fast exchange processes.

Dynamic processes we observe as slow exchange processes on the NMR timescale, are therefore processes which are sufficiently slow to at least complete one oscillation before being exchanged to a different magnetic environment. In the slow exchange depicted in Figure 46, the rate of exchange is slow enough to produce multiple oscillations per exchange, thus giving rise to two distinct frequencies after a FFT.

As the exchange rate increases, the exchanges are bound to happen multiple times within each oscillation. At the coalescence exchange rate, this is responsible for the broad FFT output as there are no distinct frequencies present. If the exchange rate is further increased, a sharp and uniform frequency will appear, as the free induction decay signal becomes increasingly smooth. Upon rapid exchange, the frequency thus becomes an average of the distinct environments δ_A and δ_B, which can be seen in Figure 45 and 46. In fact, rapid exchange processes are incredibly common in NMR spectroscopy, where rotation of methyl groups is arguably the most common example. The energetic rotational barrier of methyl groups is extremely low, which leads to rotations far too fast to observe on the NMR

timescale. Signals of methyl groups are thus observed as sharp and uniform - although the three hydrogen positions usually lie in different magnetic environments in a frozen molecule.

4.4.2 Eyring Equation

The Eyring equation emerged from transition state theory as a Boltzmann population of molecules being able to cross an energy barrier.

$$k = K(\frac{k_b T}{h})e^{-\Delta G^{\ddagger}/RT} \qquad \text{Eq. 3 [74]}$$

Where k is the rate constant, K transmission constant, k_b Boltzmann distribution, T temperature, h Planck's constant, $\Delta G^{\ddagger}$ activation energy and R universal gas constant. The Eyring equation therefore offers an approximation of the relationship between the molecular rate constant and the free energy, which is of particular interest when studying dynamic NMR processes. Measuring the empirical rate constant or free energy is however complicated, but the NMR timescale opens a backdoor to the rate constant.

At coalescence, the NMR signals are broadened out to the point where it is no longer possible to detect two separate frequencies. The lifetime at coalescence can therefore be derived from the width of the signals.

$$\Delta\nu\tau = \frac{2}{\sqrt{2}\,\pi} \Leftrightarrow \tau \approx \frac{0.450}{\Delta\nu} \qquad \text{Eq. 4 [74]}$$

Where $\Delta\nu$ is the separation of chemical shift for δ_A and δ_B given in Hertz, τ is the lifetime of the molecular states and the constant serves as a mathematical definition of the line broadening happening at coalescence. The lifetime at coalescence can thus be seen to be inversely proportional to the separation of chemical shift, meaning molecular states which are close in chemical shift (small $\Delta\nu$) needs a longer lifetime to coalesce. From there, the lifetime approximation at coalescence gives us a direct solution to the rate constant - and by Eq. 3, also the activation energy.

$$k = \frac{1}{\tau} \qquad \text{Eq. 5 [74]}$$

There are however limitations to the dynamic processes that are observable in the NMR timescale. If the lifetimes of the molecular states are not able to be manipulated into the order of 1-100 ms, the dynamic behavior is generally not observable. It is therefore just a

small scope of molecules that possess dynamic behaviors in the NMR timescale, and they generally have activation energies of 10-20 kcal/mol - as there are limitations to both equipment and solvents at extreme temperatures. Table 3 expresses that dynamic behavior generally becomes observable at low temperatures for activation energies of 10 kcal/mol, at room temperature for activation energies of 15 kcal/mol and high temperatures for activation energies of 20 kcal/mol.[74]

Table 3. Typical range of observable dynamic NMR processes with free energies and temperatures in relation to lifetimes (τ).[74]

$\Delta G^{\ddagger}$ (kcal/mol)	**223 K**	**298 K**	**373 K**
10	1 ms	3.5×10^{-3} ms	9.3×10^{-5} ms
15	10.8×10^{4} ms	16 ms	7.9×10^{-2} ms
20	8.6×10^{9} ms	7.5×10^{4} ms	68 ms

5 COMPUTATIONAL CHEMISTRY

Some of the work within this chapter has been used in the course KJE-3102 Computational Chemistry, Autumn 2022 hosted by University of Tromsø.

5.1 Density Functional Theory

Finding a complete solution to the Schrödinger equation for many-body systems is often impossible, and density functional method elegantly approximates such a solution using the electron probability density. The foundation of the density functional theory we use today comes from the Hohenberg-Kohn theorems proposed in 1964.[85]

$$\widehat{H}\boldsymbol{\Psi} = E\boldsymbol{\Psi} \qquad \text{Eq. 6 [86]}$$

$$\boldsymbol{\psi} = \boldsymbol{\psi}(\boldsymbol{x}_1, \boldsymbol{x}_2, \ldots, \boldsymbol{x}_N), \ \textit{where}\ \boldsymbol{x}_i = \{\boldsymbol{r}_i, \sigma_i\} \qquad \text{Eq. 7 [86]}$$

It can thus be seen that solving the Schrödinger equation becomes increasingly difficult with a larger number of particles as each $\boldsymbol{x}_i$ is dependent on three spatial coordinates ($\boldsymbol{r}_i$) and one spin coordinate (σ_i) of every particle in the system. The DFT method takes another approach using the one-electron probability density $p(\boldsymbol{r})$ to obtain the *ground-state electron density* in comparison to other methods that compute the ground-state N-electron wave function.

$$p(\boldsymbol{r}) = \int |\boldsymbol{\psi}(\boldsymbol{r}, \sigma, \boldsymbol{x}_2, \ldots, \boldsymbol{x}_N)|^2 d\sigma d\boldsymbol{x}_2, \ldots, d\boldsymbol{x}_N \qquad \text{Eq. 8 [86]}$$

The ground-state density can thus be seen to reduce the complexity of the problem to depend only on three electronic coordinates. Considering the electronic Hamiltonian, one finds that it contains *two* system-independent and *one* system-dependent term:

$$\widehat{H} = \widehat{H}_{[v]} = \widehat{T} + \widehat{W} + \sum_N \widehat{v}(\boldsymbol{r_i}) \qquad \text{Eq. 9 [86]}$$

$$\widehat{v}(\boldsymbol{r_i}) = -\sum \frac{Z_a}{|r_i - R_A|} \qquad \text{Eq. 10 [86]}$$

Where T is the kinetic energy operator, W is the electron-electron repulsion potential energy operator and $v(\boldsymbol{r}_i)$ is the system-dependent electron-nucleus attraction potential energy

operator, also called the *external potential*. It is therefore evident that the Hamiltonian depends on both the position and charge of atomic nuclei.

Hohenberg and Kohn were the first to establish the connection between external potential, wave function and probability density when they were able to prove a unique, one-to-one mapping between these properties. Before this proof was presented it was therefore not trivial whether a unique $p(\boldsymbol{r})$ would lead to a unique wave function, and the potential problems associated with it.[87]

$$p(\boldsymbol{r}) \Leftrightarrow v_p(\boldsymbol{r}) + c \Leftrightarrow \gamma\boldsymbol{\Psi}(\boldsymbol{r}, \ldots, \boldsymbol{r}_N) \qquad \text{Eq. 11 [86]}$$

Where c is an additive undetermined constant and γ is an undetermined phase factor with the property: $\gamma^*\gamma$ = 1. This theorem together with the well known Rayleigh-Ritz variational principle proved that DFT also could be solved variationally.

$$E_v = min_p(F^{HK}[p] + (v|p)) \qquad \text{Eq. 12 [86]}$$

$$F^{HK}[p] = \langle \boldsymbol{\Psi}_p \left| \widehat{T} + \widehat{W} \right| \boldsymbol{\Psi}_p \rangle \qquad \text{Eq. 13 [86]}$$

$F^{HK}[p]$ is the *universal Hohenberg-Kohn density functional*, and solving the ground-state energy E_v using the exact functional would lead to an exact energy solution without even involving wave functions. Whereas other computational methods employ several approximations, the density functional method is up until this point considered exact. The first approximation is introduced using a non-exact functional, since the exact functional for exchange and correlation is not known.

5.1.1 Exchange-Correlation Functionals

The choice of *exchange-correlated* (XC) functional is crucial for reliable DFT calculations, as the functionals are often tailored to perform well on specific systems or for specific properties. The exchange-correlation energy is the difference between the classical- and quantum-mechanical electron-electron repulsion, in addition to a smaller difference in kinetic energy between non-interacting and interacting systems.[88] The exchange energy arises as an effect from the electron-electron repulsion due to electric charge, whilst the correlation energy arises from the correlated movement of the electrons to avoid the electrostatic repulsion.[89]

The first and simplest functionals were the *local density approximation* (LDA) and its descendant *local spin-density approximation* (LSDA). These functionals uses the electron density $p(\boldsymbol{r})$, as the only variable, and the electron density is treated as an uniform electron gas.[89] The LSDA method gives a reasonable accuracy for geometric structures such as bond lengths and angles, but the approach has systematic errors considering molecular energies.[88] In order to improve the LSDA method, the electron density derivatives were introduced to improve the functionals by making them dependent on the locally changing density gradient, considering the electron density is not uniform for real chemical systems. This was the rise of *generalized gradient approximation* (GGA) functionals, which not only depended on the electron density - but also the gradient of the electron density, $\nabla p(\boldsymbol{r})$.[89] One such functional is the PBE (Perdew-Burke-Ernzerhof), which enhances the LSDA functional:

$$\varepsilon_{xc}^{PBE} = \varepsilon_{x}^{LSDA} F(x) + \varepsilon_{c}^{LSDA} + H(t) \qquad \text{Eq. 14 [89]}$$

Where ε_{xc} is the exchange-correlation energy, ε_{x} is the exchange energy, ε_{c} is the correlation energy, $F(x)$ and $H(t)$ are non-empirical enhancement factors applied directly to the LSDA calculations. Other GGA functionals such as LYP (Lee, Yang, Parr) use parameters that are empirically determined. A common pitfall with empirically fitted functionals is their inability to give reliable results for various systems or properties, although they usually are satisfactory within their "fitted" area.[88] Despite this common pitfall, the empirical B3LYP functional has proven to be a decent choice of functional for a variety of systems and properties, and was found to be the most used functional in a 2007 study.[90]

The *adiabatic connection approximation* was used to further improve the GGA functionals. The approximation uses a smooth conversion of electron-electron interactions between the non-interacting and interacting systems.[88] Setting the interaction parameter $\lambda = 0$ equals a non-interacting system with no correlation energy. In this case, the exact wave function is given by a single Slater determinant made of Kohn-Sham orbitals - the exchange energy is therefore exactly given by the Hartree-Fock theory.[88] The smooth conversion from $\lambda = 0$ to $\lambda = 1$ gives rise to an energy profile describing how strongly correlated the system is, and this connection can be used to parameterize *hybrid* functionals such as PBE0.

$$\varepsilon_{xc} = (1 - a)\varepsilon_{xc}^{DFT} + a\varepsilon_{x}^{HF}, \; where \; a = 1 - z \qquad \text{Eq. 15 [88]}$$

$$\varepsilon_{xc}^{PBE0} = \frac{1}{4}\varepsilon_{x}^{HF} + \frac{3}{4}\varepsilon_{x}^{PBE} + \varepsilon_{c}^{PBE} \qquad \text{Eq. 16 [89]}$$

Where z is the parameter fitted from the energy profile of the correlation energy. The PBE0 functional is therefore seen as an improvement over the original PBE functional, by introducing 25 % exact exchange energy from Hartree-Fock theory combined with 75 % exchange energy from the DFT PBE functional in addition to the entire correlation energy. The introduction of Hartree-Fock theory to the DFT functionals does however come with an increase of computational scaling from N^3 up to N^4, but the improved accuracy is usually worth it.[88]

5.2 Magnetic Properties

5.2.1 Pauli Equation

All elements are prone to relativistic effects as the electrons approach velocities near the speed of light, especially for elements of greater atomic numbers. Particles are thus required to be described by four coordinates for a relativistic description, whereas three of them are spatial and one is a time coordinate. The Pauli equation can be written as:

$$\left(\frac{\hat{\mathbf{p}}^2}{2m} + \hat{\mathbf{V}} - \frac{\hat{\mathbf{p}}^4}{8m^3c^2} + \frac{Z\hat{\mathbf{s}}\cdot\hat{\mathbf{l}}}{2m^2c^2r^3} + \frac{Z\pi\delta(\mathbf{r})}{2m^2c^2}\right)\boldsymbol{\Psi}_L = E\boldsymbol{\Psi}_L \qquad \text{Eq. 19 [89]}$$

$$\text{Mass-velocity correction} = -\frac{\hat{\mathbf{p}}^4}{8m^3c^2} \qquad \text{Eq. 20}$$

$$\text{Spin-orbit correction} = \frac{Z\hat{\mathbf{s}}\cdot\hat{\mathbf{l}}}{2m^2c^2r^3} \qquad \text{Eq. 21}$$

$$\text{Darwin correction} = \frac{Z\pi\delta(\mathbf{r})}{2m^2c^2} \qquad \text{Eq. 22}$$

Where the two first terms of Eq. 19 correspond to non-relativistic kinetic and potential energy operators. The three following terms are all relativistic, where '**p**' is the momentum operator, 'm' is the mass, 'c' is the speed of light, 'Z' is the atomic number, '**s**' is the electron spin, '**l**' is the orbital angular momentum operator ($\mathbf{r} \times \mathbf{p}$) and '$\delta(\mathbf{r})$' is the Dirac delta function.[89]

The mass-velocity correction term (Eq. 20) calculates the relativistic effects caused by the electrons' velocity, resulting in the electrons' relativistic mass being greater than their non-relativistic mass as the velocity approaches the speed of light. As their relativistic mass increases, their radii shrink and electron distribution contracts (for s- and p-orbitals) towards the positively charged nucleus. Arnold Sommerfeld proposed that for 1s orbital electrons, the radial velocity of the electron should be increasing proportional to the atomic number of the

element - thus causing larger mass-velocity corrections for higher atomic number elements.[91]

The Darwin correction (Eq. 22) comes from the positively charged proton's potential acting upon the electron, which is not seen as a particle, but rather a cloud of charge. The potential strength is thus not felt uniformly in the electron cloud due to spatial orientation. A great simplicity of the Darwin correction term is that it only affects orbital angular momentum states of zero (ℓ=0). The mass-correction term together with the Darwin correction term leads to the *scalar relativity effects*, which is an approximation of the full relativistic treatment, neglecting the spin-orbit interaction.[89]

The spin-orbit correction (Eq. 21) is a relativistic effect caused by the electron spin coupled to the potential field generated by the proton. Electrons are as we know negatively charged particles which have angular momentum from their spin property. Such charged particles with angular momentum generate a magnetic field, thus having a magnetic dipole moment ($\boldsymbol{\mu}$), and such magnetic dipole moments will interact with other external magnetic fields (***B***) found in the same region of space. From the nucleus perspective there is only an electric field generated by the negatively charged electrons. However, from the electron perspective there is a mixture of electric and external magnetic field generated as the electron's velocity increases, causing the nucleus to orbit the electron faster from the electron perspective. The electron's magnetic dipole moment will now couple with the external magnetic field, resulting in the spin-orbit interaction energy being proportional to the scalar product of the magnetic dipole moment with the external magnetic field ($\boldsymbol{\mu} \cdot \mathbf{B}$).[89]

5.2.2 Chemical Shielding

As the somewhat less complicated electric field perturbation only adds a potential energy term to the Hamiltonian operator, the magnetic field perturbation changes the kinetic energy operator. This is due to the generated movement of electrons in the magnetic field perturbations, and the *canonical* momentum operator is defined as:

$$\pi = \hat{\boldsymbol{p}} - q\boldsymbol{A} \qquad \text{Eq. 23 [89]}$$

Where 'π' is the canonical momentum operator, '***p***' is the mechanical momentum given as the minus imaginary gradient ($-\, i\nabla$), 'q' is the elementary charge of the electron and '***A***' is the vector potential in relation to the flux density generated by the magnetic field '***B***'.

$$\mathbf{B} = \boldsymbol{\nabla} \times \mathbf{A}$$ Eq. 24 [89]

Using the Born-Oppenheimer approximation allows for a rewriting of (Eq. 23) considering only the charge for electrons (q = -1).

$$\pi = \hat{\boldsymbol{p}} + \boldsymbol{A}$$ Eq. 25 [89]

Defining the vector potential '***A***' does however run into a technical issue called the *gauge problem* due to the curl of a gradient always being zero, thus not uniquely defining the vector potential.

$$\mathbf{A}_{ext}(\boldsymbol{r}) = \frac{1}{2}\mathbf{B}_{ext} \times (\boldsymbol{r} - \mathbf{R}_g)$$ Eq. 26 [89]

Where '***r***' is the position and '$\boldsymbol{R_g}$' is the *gauge origin*. The gauge origin is defined as the center of the vector potential, and the kinetic energy operator demands that an origin must be chosen for the calculations. It is apparent that the magnetic field itself is independent of the chosen gauge origin, but the calculated magnetic properties may however largely depend on the choice of gauge origin. As a rule of thumb, the gauge position should never be chosen at the position of the atom one wants to observe. Neither should the gauge vector be specifically tailored or overfit to one's narrative.

There are several strategies and methods to minimize errors which originate from the choice of gauge origin. In our experiment we have chosen the gauge origin to be on either atoms, and also using the *gauge-including atomic orbital* (GIAO) method, which incorporates the gauge origin into the atomic basis functions removing the reference to an absolute gauge origin, but rather uses a distributed origin. Choosing the gauge origin to be positioned on either atom is a rather simplistic approach, and is generally not a good strategy. The GIAO method is however a more sophisticated method for dealing with the gauge problem.[89]

The nuclear magnetic shielding property can be calculated using the second-order derivative of electronic energy with respect to the magnetic field '***B***' and the nuclear magnetic moment '***I***' based on the Taylor expanded energy equation:

$$E(\tilde{\lambda}) = E(0) + \frac{\partial E}{\partial \tilde{\lambda}}\tilde{\lambda} + \frac{1}{2}\frac{\partial^2 E}{\partial^2 \tilde{\lambda}}\tilde{\lambda}^2 + \frac{1}{6}\frac{\partial^3 E}{\partial^3 \tilde{\lambda}}\tilde{\lambda}^3 + \ldots$$ Eq. 27 [89]

The perturbation 'ƛ' is usually a vector, which means the first order term will also be a vector, the second derivative will be a matrix and the third derivative will be a third-order tensor. Upon doing perturbations to the magnetic field and nuclear magnetic moment simultaneously, the energy is proportional to the mixed derivative equation:

$$NMR\ shielding \propto \frac{\partial^2 E}{\partial \mathbf{B} \partial \mathbf{I}} \qquad \text{Eq. 28 [89]}$$

In contrast to real life NMR experiments, chemical shielding calculations need to be computed in multiple spatial directions to account for the anisotropic effects which are effectively averaged out by tumbling in the real experiments. Many chemists seem to overlook the importance of the molecular tumbling in NMR experiments, thus considering the chemical shift to be a single-valued quantity when it in fact is a tensor quantity. During chemical shielding calculations, there is no such inherent tumbling which smoothly averages out the anisotropic forces. Computational methods therefore make use of applying the external magnetic field in the x, y and z direction to form a chemical shift tensor.

$$\sigma = \begin{bmatrix} \sigma_{xx} & \sigma_{xy} & \sigma_{xz} \\ \sigma_{yx} & \sigma_{yy} & \sigma_{yz} \\ \sigma_{zx} & \sigma_{zy} & \sigma_{zz} \end{bmatrix} \qquad \text{Eq. 29 [92]}$$

$$\sigma_{iso} = \frac{1}{3}(\sigma_{xx} + \sigma_{yy} + \sigma_{zz}) \qquad \text{Eq. 30 [92]}$$

Each tensor quantities can be explained as $\sigma_{\alpha\beta}$ where α represents the chemical shift in the α-direction, when the external magnetic field is applied in the β-direction. An entire 3x3 array is thus built in the three dimensions around each nuclei to form the chemical shielding tensor. The average of the diagonal elements from the chemical shielding tensor is therefore the value most chemists refer to as the (isotropic) chemical shift.[92]

A major challenge with chemical shielding calculations is however the “snapshot” nature of it, where quantum chemistry programs do not provide a rationale for chemical phenomena as bond rotations during a shielding calculation as molecules are frozen in space. It is therefore necessary to have a strong chemical intuition to bridge the gap between computational and experimental observations in NMR spectroscopy.

6 RESULTS AND DISCUSSION

6.1 Synthesis and Characterization

6.1.1 Optimized Reaction Conditions

The first discovered metallobiscorroles were synthesized in adequate yields of ~15 %, upon interacting free-base corrole with 3 equimolar of tungsten hexacarbonyl and excess potassium carbonate at ~190 °C in decalin solvent. Similarly, the molybdenum biscorroles were prepared using the same synthetic method with even greater yields up to 30 %. All of the earlier prepared metallobiscorroles were either meso-substituted with plain phenyl groups, or *para*-substituted phenyl groups - in other words, with little steric crowding.

My thesis started with synthesizing tungsten biscorroles with 5,10,15-tris(pentafluorophenyl) free-base in the hopes that reducing the number of hydrogen atoms in the metallobiscorrole would reduce the complexity of the ^{1}H NMR. The yield of this metallobiscorrole was however incredibly low (< 1 %) and not sustainable using the same reaction conditions as above. Several of the reaction conditions were attempted to be changed such as the solvent system, equimolar amounts and prolonged reaction time - without any indication of improved yields. However, an increased reaction temperature to 220 °C consistently increased the yields to above 1 % for the particular metallobiscorrole. Fortunately, the increase of temperature also improved the yields of the latter synthesized metallobiscorroles, thus elevated reaction temperatures of 220-240 °C became the norm.

Despite improving the yields, the best experiments barely reached above 10 % for the meta-substituted metallobiscorroles, and were still extremely low for ortho-substituted metallobiscorroles. The level of steric hindrance from para, meta and ortho-substitutions therefore gave a potential rationale for the progressively lower yields.

Another challenging aspect of the metallobiscorrole synthesis was the relatively high yields of μ-oxo bridged metallocorrole dimers, as the formation of these complexes reduced the free amounts of corrole free-base in the reaction. An attempt to reduce the formation included that the synthesis was done under anaerobic atmosphere by continuously running argon gas through the reaction flask, with the main goal of reducing available oxygen to form μ-oxo bridged metallocorrole dimers. Despite these efforts, the formation of μ-oxo bridged metallocorrole dimers still remained relatively high. Upon examining the reactants, potassium carbonate was found to be the only source of oxygen atoms in the reaction.

Potassium carbonate was used as the base reactant to pick up internal protons of the corrole free-base to convert it into its anionic and reactive form. Other bases such as 2,6-lutidine and 1,8-diazabicyclo(5.4.0)undec-7-ene (BDU) were therefore attempted as they contained no oxygen atoms. Despite their steric hindrance towards the corrole free-base cavity, it was confirmed by UV-Vis analysis that they were in fact capable of stealing the internal protons from the corrole at room temperature. Upon following analogous reaction conditions as before with 2,6-lutidine or BDU as base, the reaction did not progress and corrole free-base could be recovered by silica gel column.

Adding potassium carbonate to an already deprotonated reaction mixture in >180 °C led to the discovery of an intermediate oxo-metallocorrole M[Cor]O (M = Mo, W), as the reaction mixture was consecutively analyzed by mass spectrometry with short time intervals. It was therefore apparent that the decomposition of potassium carbonate was the source of available oxygen. As the other bases did not progress the reaction, potassium carbonate was speculated to be a necessary reactant in the formation of metallobiscorroles, despite fueling the formation of μ-oxo bridged metallocorrole dimers. In fact, the oxo tungsten metallocorrole is an unknown compound, but attempts to isolate it led to decomposition of the metallocorrole, yielding free-base corrole after silica gel chromatography.

6.1.2 *o*-Substituted Metallobiscorroles

As dynamic effects on the ^{1}H NMR was observed and believed to be caused by rotations of the meso-phenyl substituents, attempts to synthesize rotationally locked metallobiscorroles became a major interest. Introducing large atoms or chemical groups in the ortho-positions of the *meso*-phenyl substituents would effectively lock the possibility of rotation about the corrole-phenyl bond, and perhaps yield ^{1}H NMR spectra without or with significantly slowed dynamic effects.

In the light of this, two tungsten metallobiscorroles were attempted synthesized with 2,6-dichlorophenyl and 2,6-dimethoxyphenyl as meso-substituents. Unfortunately, after several attempts, the idea had to be abandoned due to extremely low yields as an ^{1}H NMR sample would require approximately 5 mg of the compound.

6.1.3 Diastereomerism

The first sign of diastereomerism was observed in the purification of tungsten 5,10,15-tris(3,5-bis(trifluoromethyl)phenyl) biscorrole as the compound made a slightly wider than usual band on the preparative TLC plate. Out of curiosity, the upper and lower fractions

of the band were scraped separately, and to our surprise revealed indifferent UV-Vis spectra with consistent mass spectra! ^{1}H NMR analysis confirmed that the separated compounds indeed were different, and the indifferences in UV-Vis spectra were not caused by other compounds or impurities in the sample. The success was then repeated with molybdenum 5,10,15-tris(3,5-bis(trifluoromethyl)phenyl) biscorrole, and thereafter tungsten 5,10,15-tris(3,5-dimethoxyphenyl) biscorrole.

Attempts to carefully separate diastereomers of the other synthesized metallobiscorroles on preparative TLC yielded no results as the UV-Vis spectra could not be distinguished. It was therefore concluded that either (I) the second diastereomer does not synthesize in high enough yields to be separated, (II) the second diastereomer does not possess large orbital energetic changes causing the UV-Vis spectra to be indifferent or (III) the second diastereomer were present, but inseparable on preparative TLC.

It is worth to note that the above points could be investigated further using ^{1}H NMR analysis, but with the low yielding syntheses it would be quite a laborious task. Personally, I have come to believe that both diastereomers are always synthesized, and are thus one of the main reasons for the reputation of uninterpretable ^{1}H NMR spectra of metallobiscorroles.

Earlier studied molybdenum biscorroles could also suggest that both diastereomers were in fact present, as the near-IR UV-Vis spectra possessed two electronic transitions separated by approximately 100 nm.[69] The calculations however, did not give an assignment for the second electronic transitions, and it was thus attributed to a vibronic band. This could suggest that the observed second electronic transitions in reality belonged to the second diastereomer, as the UV-Vis sample may have been a mixture of the two.

6.1.4 UV-Vis

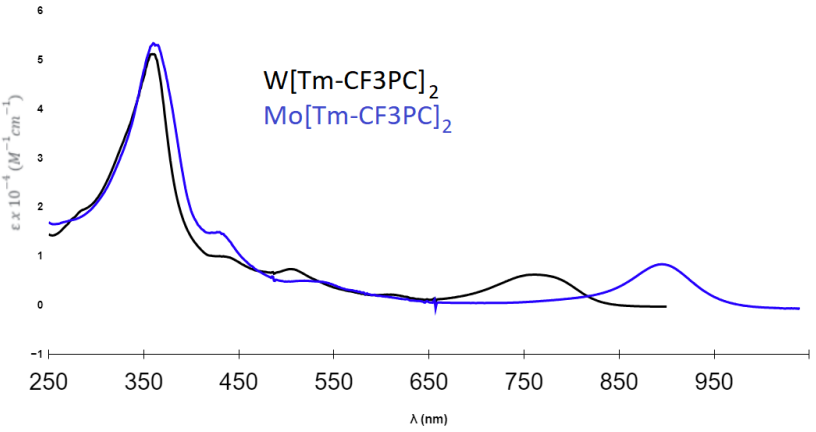

Figure 47. UV-Vis comparison of tungsten and molybdenum biscorroles.

UV-Vis spectra of metallobiscorroles possess some clear characteristics of a highly blueshifted Soret transition (in comparison to the corrole free-base) in the 360 nm region and its near-IR features, which is attributed by TDDFT calculations to be a ligand-to-metal charge transfer transition into the empty $5d_z^2$ LUMO.

The characteristic UV-Vis spectra are thus of high importance in the analytical investigation of the diastereomers. Considering we were unable to produce X-ray quality crystals of the second diastereomer, the UV-Vis characteristics almost guarantees that both compounds in fact are eight-coordinate square antiprismatic sandwich complexes - directly implying they must be diastereomers. The argument for diastereomerism is thus significantly strengthened by the implication of eight-coordinate square antiprismatic geometry of both compounds.

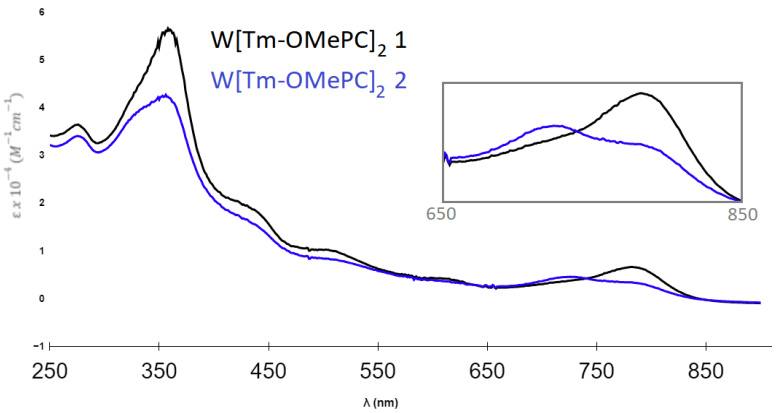

Figure 48. UV-Vis spectrum of W[T*m*-OMePC]$_2$ 1 and 2.

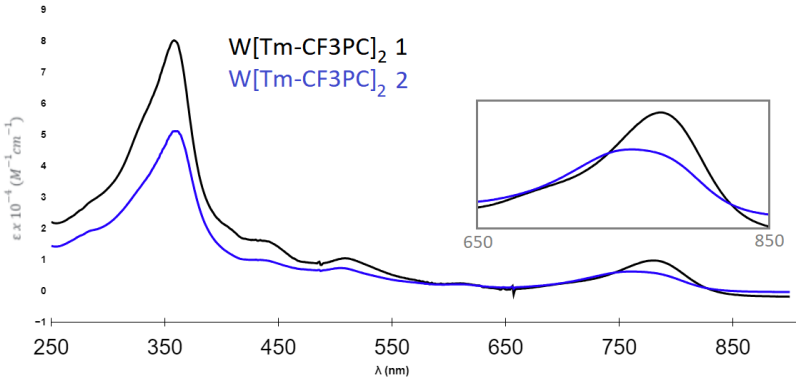

Figure 49. UV-Vis spectrum of W[T*m*-CF_3PC]$_2$ 1 and 2.

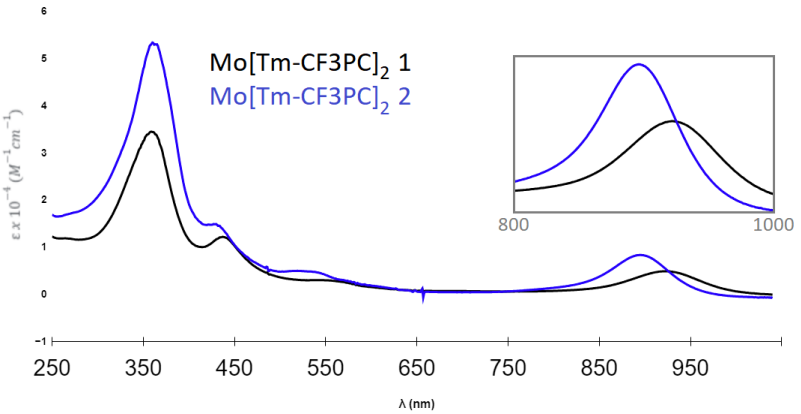

Figure 50. UV-Vis spectrum of Mo[T*m*-CF_3PC]$_2$ 1 and 2.

The largest difference of near-IR features were found in W[T*m*-OMePC]$_2$ 1 and 2 where they were separated by approximately 50 nm. It was also evident that the separation of diastereomers was only partially successful as W[T*m*-OMePC]$_2$ 2 seemed to have a weak transition in the 780 nm region attributed to the other diastereomer.

6.1.5 X-ray Crystallography

Notes from the crystallographers which worked on the samples:

> "Due to the reflection intensity decreasing significantly at higher resolution, the data was cut to a resolution of 0.90 Å, as this was determined to be the highest resolution shell with an R_{int} lower than 25 %. In order to make aspects of the molecule behave (in particular the CF_3 groups), the SADI and RIGU restraints were employed, along with the ISOR and DFIX constraints. Lastly, a solvent mask was applied within the Olex2 software package to remove undetermined and poorly resolved outer sphere solvent molecules.
>
> It is the opinion of the crystallographers that worked on these structures that these models are best utilized for demonstrating general information about packing, shape, size, etc. However, bond distances and angles will not be particularly "trustworthy," for lack of a better word, and if statements wish to be made about bond lengths and angles, it would be best to grow new crystals for better data collection if possible."

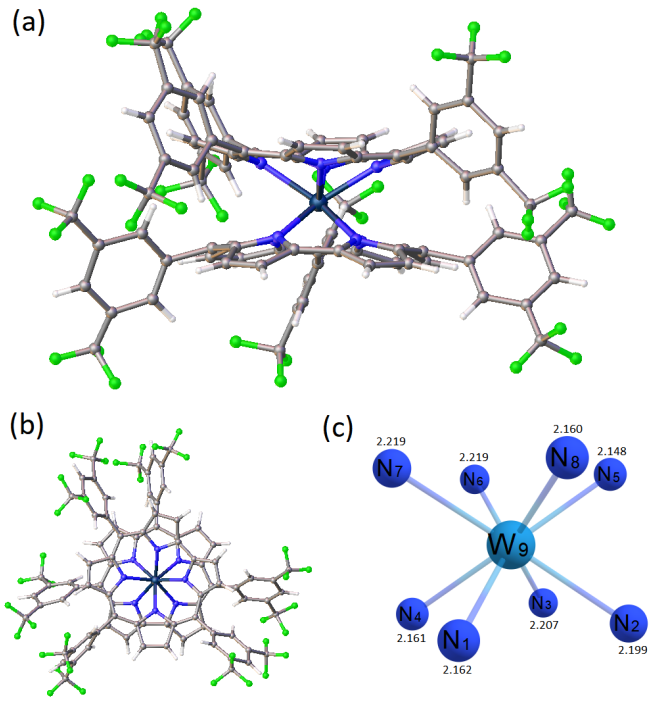

Figure 51. X-ray crystal structure of W[T*m*-CF_3PC]$_2$ 1 (a) side and (b) top view, with (c) W-N distances (Å).

Table 5. X-ray crystallographic data for W[T*m*-CF_3PC]$_2$ 1.

Sample	**W[T*m*-CF_3PC]$_2$ 1**
Chemical Formula	$C_{86}H_{34}F_{36}N_8W$
Formula mass	2047.03
Crystal system	Triclinic
Space group	$P\bar{1}$
λ [Å]	0.90
a [Å]	13.9669(15)
b [Å]	16.1457(17)
c [Å]	22.215(2)
α [°]	70.499(4)
β [°]	76.662(4)
γ [°]	80.166(4)
Z	2
Z'	1
V [Å^3]	4570.8(8)
Measured reflections	71593

R_{int}	0.0807
R_1, wR_2 all data	0.0766, 0.2308

Despite the crystallographer's concern for precise bond lengths and angles, the crystal structure of W[T*m*-CF_3PC]$_2$ 1 clearly demonstrated the most important properties of the metallobiscorrole sandwich - as the conformational structure is not influenced by that level of precisement. The crystal structure of W[T*m*-CF_3PC]$_2$ 1 revealed that the compound was the 135 degree sandwich, where the two corrole moieties had the meso-10 positions approximately rotated by 135 degrees relative to each other. It was also evident that the corrole moieties were strongly domed, as seen in previously solved metallobiscorrole X-ray structures, thought to be partially caused by the size mismatch between the metal and contracted corrole cavity and steric repulsions of the meso-phenyls.

Unfortunately, we were only able to obtain one X-ray crystal structure during the course of my thesis - despite that a major part of the synthetic efforts consisted of crystallization experiments. Well above hundred crystallization experiments was set up during a period of one year, where approximately 30 promising samples were sent to collaborators at Advanced Light Source at the Lawrence Berkeley National Laboratory and Dr. Y. Rousselin at the Institute of Molecular Chemistry of the University of Burgundy. Feedback on failed crystal samples was that they were either not crystalline, or not diffracting enough.

Common crystallization techniques such as vapor and liquid diffusion were attempted with plenty of different solvent systems for all the synthesized metallobiscorrole compounds with no luck. Ironically, the only crystal experiment that was solved, was evaporated until dryness and was sent as dry crystals to the crystallographer. This is generally not a preferable technique, as important solvate molecules in the crystal structure can evaporate and severely degrade the quality of the crystals. A major issue with crystallization of the metallobiscorrole sandwiches was the poor synthetic yield, which severely limited the numbers of crystallization experiments.

6.2 NMR

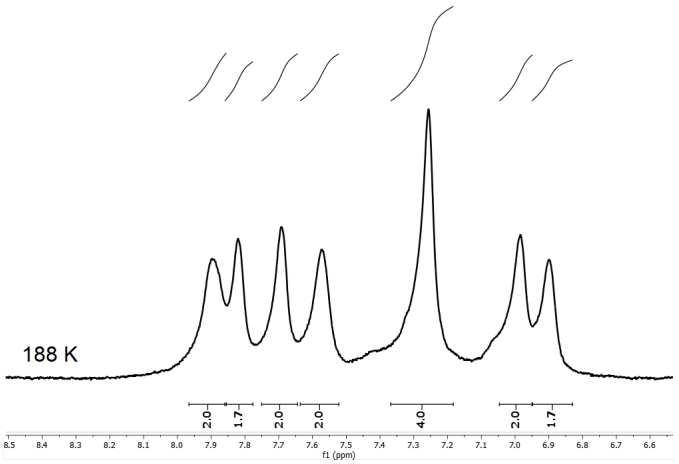

Figure 52. ^{1}H NMR spectrum of W[TPFPC]$_2$ obtained at 188 K.

Replacement of peripheral hydrogens with fluorines on the phenyl groups with the W[TPFPC]$_2$ biscorrole led to the first successful ^{1}H NMR spectrum of biscorroles as the temperature was lowered to 188 K. All corrole β-protons appeared in the ~7-8 ppm region as previous ^{1}H NMR analyses of biscorroles also suggested, given that the large overlaps and unclear NMR signals belonged to this region. Notably, the β-protons of biscorroles were highly upfield shifted compared to other metallocorrole complexes where they are generally found in the ~8-10 ppm region, possibly indicating weaker aromaticity in biscorroles.

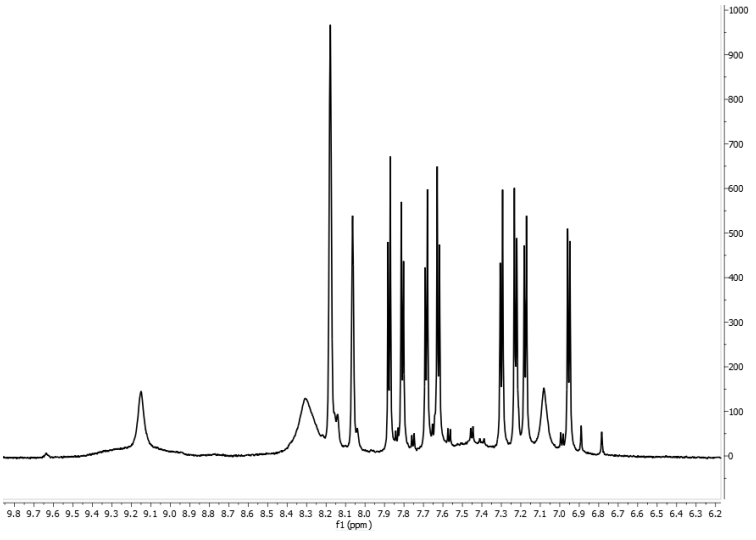

Figure 53. ^{1}H NMR spectrum of W[T*m*-CF$_3$PC]$_2$ 1 obtained at room temperature.

A major milestone was reached as both diastereomers of W[T*m*-CF$_3$PC]$_2$ and Mo[T*m*-CF$_3$PC]$_2$ produced high quality ^{1}H NMR spectra in room temperature. The ^{1}H NMR

spectrum at room temperature of W[T*m*-CF_3PC]$_2$ 1 gave a clear indication of a C_2 symmetric structure considering the chemical environment of the corrole β-hydrogens, as the corrole β-hydrogens overlapped in eight pairs with each an integral equal to two. Notably, as the compounds had *meta*-substituted phenyls at the meso-positions, none of the phenyl hydrogens would possess J-coupling effects. This gave a simple assignment of the corrole β-hydrogens as the only eight J-coupled signals which appeared in the spectrum.

Furthermore, the *p*-phenyl hydrogens was then detected in the 8.1 and 8.2 ppm region with respective integrals of two and four, giving indication of meso-10 *p*-phenyl hydrogens overlapping in the 8.1 ppm region, and meso-5 and -15 *p*-phenyl hydrogens overlapping in the 8.2 ppm region. These findings were also consistent with the C_2 symmetry of the metallobiscorrole sandwich. The only remaining ^{1}H NMR signals would then have to be attributed to the *o*-phenyl hydrogens, which consisted of broad peaks in the 7.1, 8.3 and 9.2 ppm region. A series of low temperature ^{1}H NMR down to 193 K gave a remarkable unveiling of the compound's dynamic structure and explanation of the broad *o*-phenyl hydrogen NMR signals.

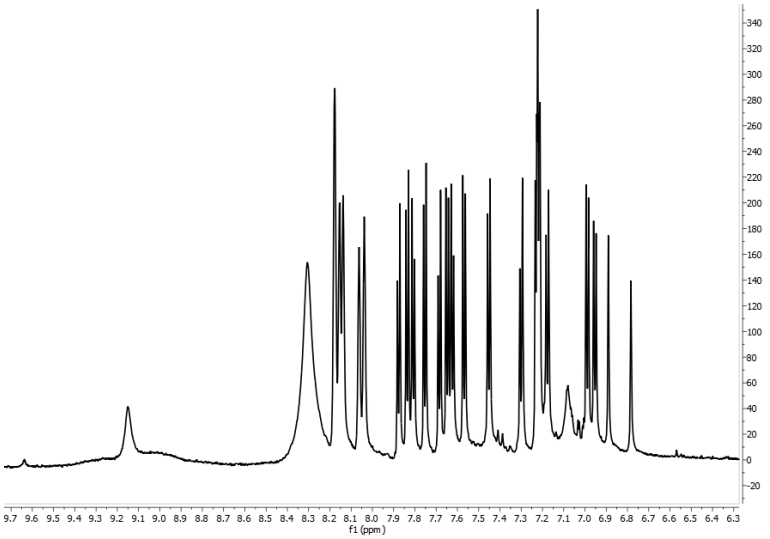

Figure 54. ^{1}H NMR spectrum of W[T*m*-CF_3PC]$_2$ 2 obtained at room temperature.

To our surprise, ^{1}H NMR analysis of the second diastereomer suggested it was not C_2 symmetric, as the β-hydrogens were no longer paired, but rather appeared as 16 distinct signals. Despite this, the ^{1}H NMR spectrum was fully open to interpretation with a similar approach as with the first diastereomer. ^{1}H NMR analysis of the Mo[T*m*-CF_3PC]$_2$ sandwich complexes also suggested that the first diastereomer was C_2 symmetric, while the second diastereomer was not.

6.2.1 Aromatic Solvent Induced Shift

In attempts to reduce the overlapping in the aromatic region of certain ^{1}H NMR spectra, several different solvents were screened. Dichloromethane was early found to be an excellent solvent for ^{1}H NMR of biscorroles as the solubility was high and the solvent shift did not interfere with the spectra. Introduction of aromatic solvents was thus proposed as a potential improvement - it would however be inevitable that the solvent shift would interfere with the aromatic region, thus potentially making the ^{1}H NMR spectra worse.

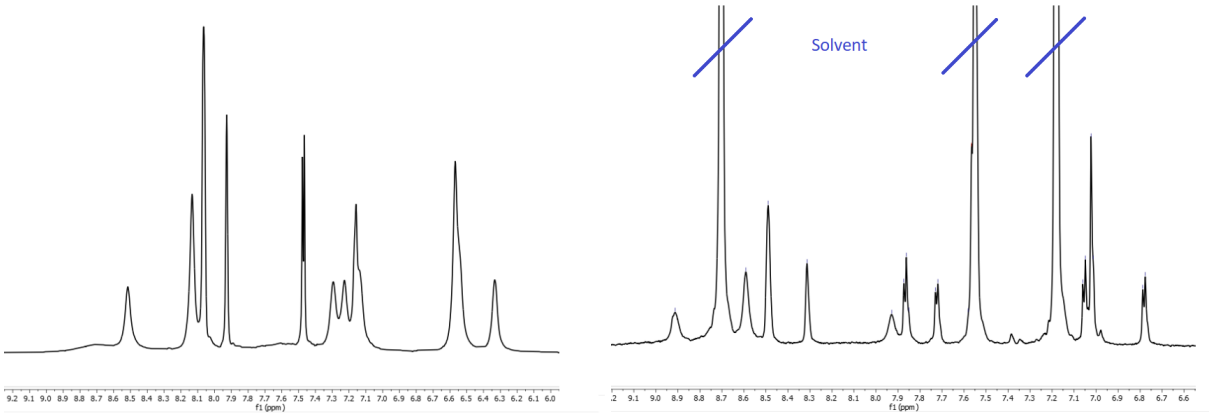

Figure 55. ^{1}H NMR spectra of Mo[T*m*-CF_3PC]$_2$ in (left) dichloromethane and (right) pyridine.

Mo[T*m*-CF_3PC]$_2$ were found to have sufficient solubility in pyridine, which introduced ASIS due to its aromaticity. The spectra obtained in dichloromethane and pyridine were clearly different, with a less overlapping aromatic region in pyridine. However, one of the solvent shifts from pyridine did overlap with one of the metallobiscorrole shifts in the 7.55 ppm region. Nevertheless, the spectra obtained in pyridine was overall an improvement as higher quality peaks with J-coupling could be seen, in addition to less overlapping signals. Introduction of aromatic solvents thus proved to be a slight improvement for certain biscorrole ^{1}H NMR spectra, often as a complementary method as solvent shift overlaps could introduce difficulties with the interpretation.

6.2.2 Variable Temperature NMR

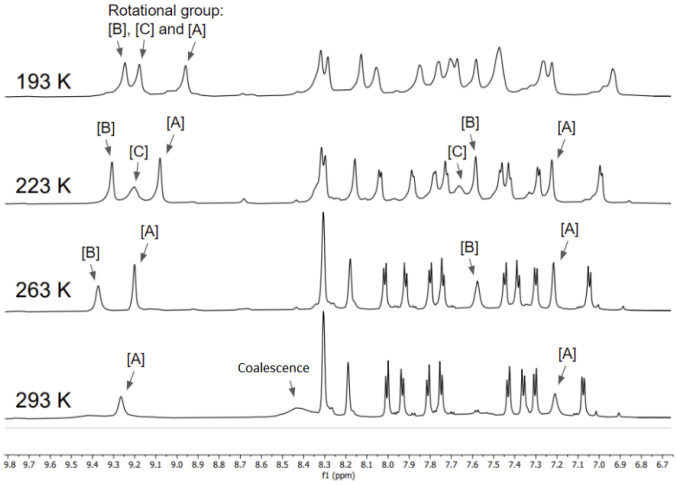

Figure 56. Variable temperature ^{1}H NMR spectra of W[T*m*-CF_3PC]$_2$ 1.

As room temperature ^{1}H NMR analysis overall produced high quality spectra of the W[T*m*-CF_3PC]$_2$ and Mo[T*m*-CF_3PC]$_2$ biscorrole sandwiches, the *o*-phenyl hydrogens had abnormal chemical shifts and lineshapes. It quickly became apparent that the sandwich complexes were subject to dynamic NMR effects as the temperature was progressively lowered towards ~ 190 K. What appeared as a broad signal at 8.4 ppm was the coalescence signal of the *o*-phenyl hydrogens, and the smaller peaks at 7.2 and 9.3 ppm was confirmed by TOCSY NMR to be all four *o*-phenyl hydrogens in the meso-10 positions of the sandwich complex. Directly implying that the phenyls at the meso-10 positions are exchanging (i.e. rotating) slower than the 5- and 15-meso positions. In light of the X-ray crystal structure obtained of W[T*m*-CF_3PC]$_2$ 1, we can conclude that this effect is not driven by higher steric crowding in the meso-10 positions. The effects of slower rotation of meso-10 phenyls are thus believed to be caused by a higher double bond character between the corrole and phenyl units compared to meso-5 and -15 phenyls.

Given C_2 symmetry of the W[T*m*-CF_3PC]$_2$ 1 complex, the six phenyl groups would form a total of three symmetric phenyl environments, as depicted in Figure 56 by rotational groups *A*, *B* and *C*, where *A* is the *o*-phenyls in the meso-10 position. As the rotational exchange was slowed down by reduction of the temperature, other *o*-phenyl hydrogens *B* and *C* started to appear in the 7.6 and 9.3 ppm area, which were the remaining meso-5 and -15 *o*-phenyl hydrogens.

The Eyring's equation (Eq. 3) was used to approximate the energetic barrier of rotation for the W[T*m*-CF_3PC]$_2$ 1 complex.

Table 4. Rotational barriers of meso-phenyls (group: A, B, C) in W[T*m*-CF_3PC]$_2$ 1, calculated using the Eyring's equation. (a) Estimation of coalescence temperature based on shape and size of NMR signal at 293 K.

Rotational group	Rotational barrier [kcal/mol]	Coalescence frequency [Hz]	Coalescence temperature [K]	Chemical shift [ppm]
10-meso phenyls [A]	14.1	1867	323[a]	7.2, 9.3
5- and 15-meso phenyls [B]	13.3	1600	303[a]	7.6, 9.4
5- and 15-meso phenyls [C]	11.1	1422	253	7.7, 9.3

6.2.3 Chemical Shielding Analysis

A major contribution to deciphering the unnatural ^{1}H NMR spectra of biscorroles came from shielding calculations, which suggested that half of the *o*-phenyl hydrogens should be highly deshielded in the ~ 9 ppm region. Upon closer investigation, the respective *o*-phenyl hydrogens were all found in the endo-region of the biscorrole structure. Realizing that the chemical structure wasn't static like X-ray crystal structures or geometry optimization structures, but rather a dynamic system involving phenyl rotations, generated a large interest in computing the chemical shielding of the trajectory of the *o*-phenyl hydrogens.

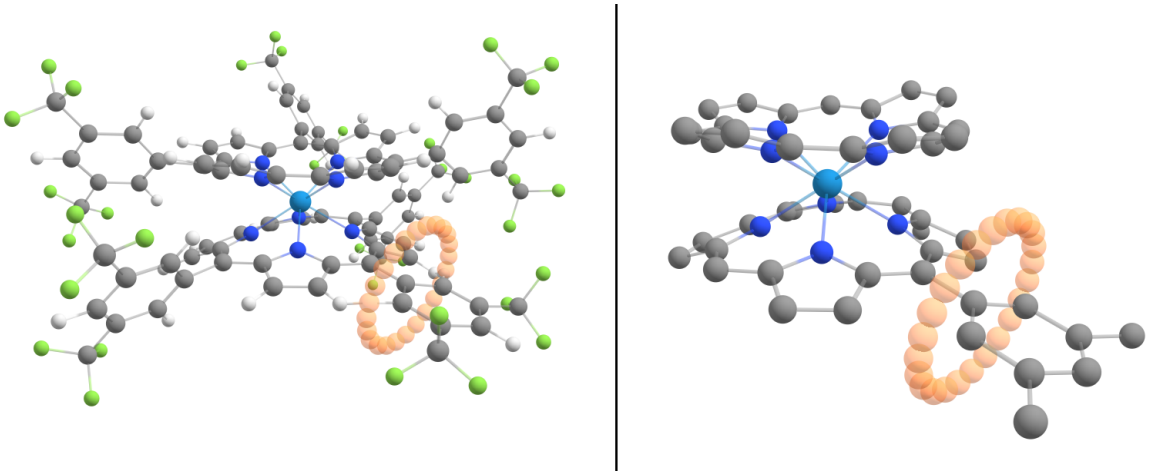

Figure 57. Ghost atoms are represented as orange. Left: Full biscorrole structure used with the chemical shielding calculations. Right: Biscorrole structure with omitted substituents.

The studied phenyl group was forced into an unnatural planar state with respect to the corrole moiety to reduce interference along the trajectory - as the chemical shielding rises to extreme values as the ghost atom is placed in close proximity to other atoms. Upon doing some trial calculations, the planar state was already similarly disturbed as the corrole β-hydrogens was too close to the trajectory. Additionally, the chemical shielding in the planar state was not of great interest as the structure was not believed to ever stay there for

prolonged time, but rather quickly transitioning through. Rotating the phenyl group planar to the corrole moiety thus allowed for better chemical shielding calculations in the endo- and exo-regions, which was the major interest.

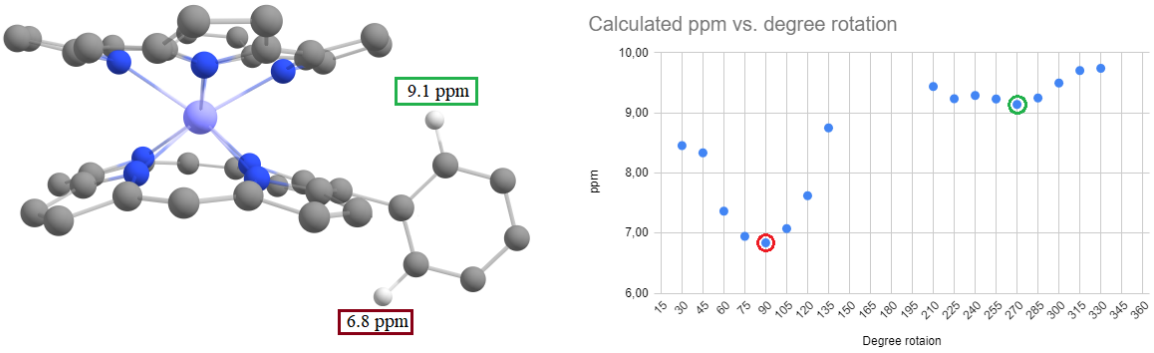

Figure 58. Biscorrole structure with omitted substituents for clarity, including chemical shielding calculations in the trajectory of the *o*-phenyl hydrogens.

The calculations suggested that the *o*-phenyl hydrogens were separated by approximately 2 ppm at the most extreme positions perpendicular to the corrole moiety. As discussed previously, the data points in proximity to the planar structure are not shown as they get significantly influenced by the nearby nuclei. As corroles and biscorroles exhibit their lowest energy state at a 45-60 degree rotation of the phenyl substituents, induced by the partial overlap of π-orbitals, the findings seemed consistent with the empirical ^{1}H NMR data which suggested 7.1 and 9.2 ppm for the respective *o*-phenyl hydrogens. It therefore became evident that the rotational position of the phenyl groups played a significant part in the ^{1}H NMR data, and upon rapid rotations, would create dynamic effects.

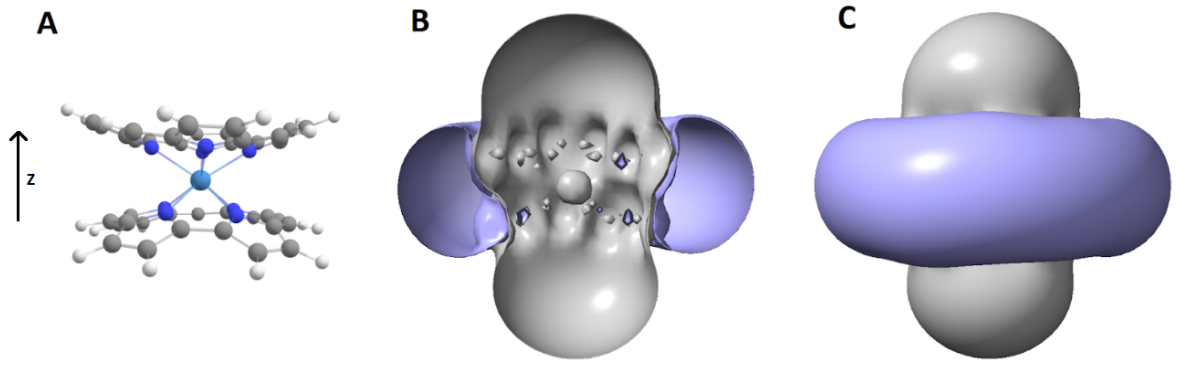

Figure 59. (A) Unsubstituted biscorrole structure used for calculations. (B) Cross section of isotropic ICSS. (C) Full isotropic ICSS.

Table 6. Isotropic chemical shielding in the ZX-plane located directly above the central tungsten (**W**) atom in the biscorrole structure.

z									
	8	0.1	0.4	0.9	1.5	1.8	1.5	1.2	0.5	0.2
	6					3.7				
	4	−0.4	−0.4	1.3	7.0	8.5	7.4	2.1	−0.1	−0.3
	2					16,5				
	0	−0.8	−1.1	4.0	15.7	**W**	15.2	2.3	−1.7	−0.9
	-2					16.6				
	-4	−0.3	−0.1	3.4	7.5	8.5	8.2	2.8	−0.5	−0.4
	-6					3,7				
	-8	0.2	0.5	1.0	1.5	1.8	1.5	0.9	0.4	0.1
	Å	**-8**	**-6**	**-4**	**-2**	**0**	**2**	**4**	**6**	**8**
						x				

An unsubstituted biscorrole structure was used to reduce the peripheral interference of the ICSS, as the main question was if the biscorrole structure acted as one large aromatic system or two independently aromatic systems under an external magnetic field. It is worth to note that the unsubstituted biscorrole was not geometry optimized after removing the substituents, as a change to the aromatic systems was unwanted. However, the consequences of this were believed to be minuscule, as we were not actively interested in the chemical shielding of particular nuclei, but rather the space surrounding them.

The gray area in Figure 59 depicts higher isotropic chemical shielding (lower chemical shift), while violet area depicts lower isotropic chemical shielding (higher chemical shift). In other words, as an external magnetic field is applied in the Z-direction, the gray area has an induced magnetic field directed in the negative Z-direction, while the violet area has an induced magnetic field directed in the positive Z-direction. Hydrogens positioned in the gray area would therefore perceive the external magnetic field as $B_{tot} = B_{ex} - B_{ind}$, while hydrogens positioned in the violet area would perceive the external magnetic field as $B_{tot} = B_{ex} + B_{ind}$.

The results unambiguously suggested that the biscorrole structures behaved as one larger aromatic system as the higher chemical shielding area (violet) consisted of one solid torus. If the structure behaved as two independently aromatic systems, the violet area should have

consisted of two adjoint toruses in the same area. The calculations also revealed, similarly to what was covered in Section 4.3, that the δ_{zz} chemical shielding tensor was the major contributor to the isotropic shift - almost to the point where it was the only contributor, i.e. $\delta_{iso} = \frac{1}{3}\delta_{zz}$.

The upfield shifted experimental chemical shift of metallobiscorroles compared to other metallocorroles is likely caused by weaker aromaticity in the biscorrole system. A possible explanation is that the aromaticity is partially strained as the independent aromatic corrole units are linked by a single atom, meaning electrons have to flow in both directions through the same atom. Interestingly, metallobiscorroles are possibly 3D aromatic structures and they do in fact satisfy the 6n+2 electron rule for 3D aromaticity with its 44 π-electrons.[93]

6.2.4 SpinWorks 4 NMR Simulation

The SpinWorks 4 program was used to further investigate and validate the dynamic effects observed in ^{1}H NMR spectra of the metallobiscorroles. Given the complexity of having three symmetrical dynamic processes occurring simultaneously, such as in W[T*m*-CF_3PC]$_2$ 1, only one of the symmetric rotational groups was analyzed in depth. Rotational group C (ref. Fig. 56 & Table 4) was chosen as it displayed the full range of dynamic behavior going from a single broad signal at room temperature, disappearing at coalescence and into two signals separated by a couple ppm in low temperatures.

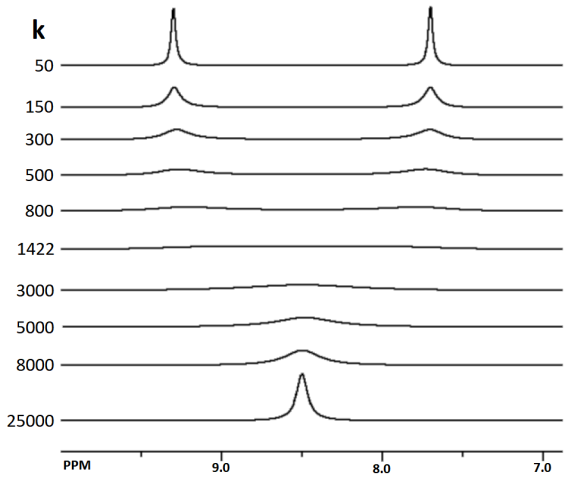

Figure 60. Dynamic ^{1}H NMR simulation with parameters similar to rotational group C in W[T*m*-CF_3PC]$_2$ 1, where *k* is the exchange rate per second.

Simulation criteria was configured similarly to the properties of rotational group C, with two ^{1}H located at 7.7 and 9.3 ppm while undergoing a mutual exchange of magnetic environments at the rate *k* (sec^{-1}). Simulating over a large range of *k* resulted in the plot depicted in Figure 60, with many similarities to what was observed in the ^{1}H NMR spectra. An interesting detail is how the signal almost disappeared at coalescence as a result of the large chemical shift separation - precisely as observed in the ^{1}H NMR spectra. Figure 61 depicts a matching of theoretical simulation data (*k*) and empirical ^{1}H NMR spectrum of W[T*m*-CF_3PC]$_2$ 1.

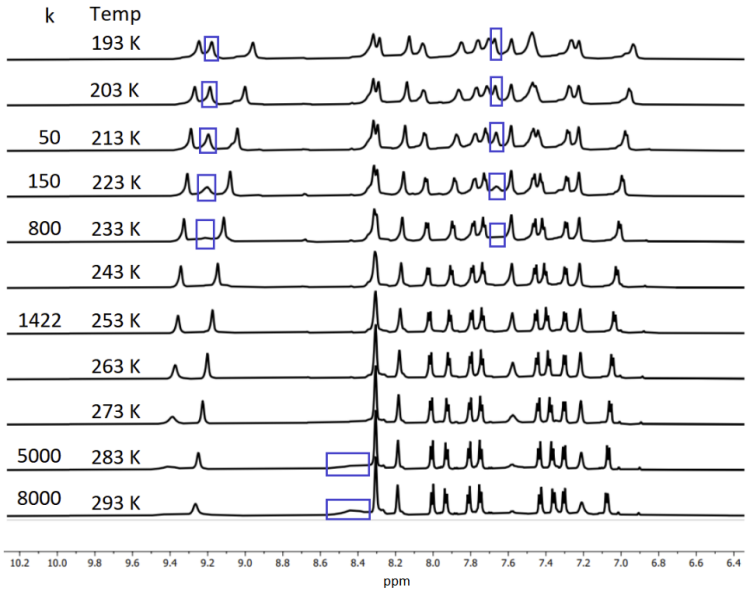

Figure 61. Variable temperature ^{1}H NMR spectrum of W[T*m*-CF_3PC]$_2$ 1, with matching exchange rates of rotational group C, which is marked with blue boxes.

6.3 Symmetry

Despite the relatively high molecular complexity of metallobiscorrole sandwiches they are still approximately C_2 symmetric as seen in previously solved X-ray crystal structures. Our solved X-ray crystal structure of W[T*m*-CF_3PC]$_2$ 1 also proved to be approximately C_2 symmetric, as the ^{1}H NMR data also strongly suggested. The lack of success to solve the structure of W[T*m*-CF_3PC]$_2$ 2 was however a major challenge during the thesis, not only because it would be the first X-ray crystal structures of diastereogenic metallobiscorroles, but the ^{1}H NMR data indicated surprisingly that the structure in fact was not C_2, but C_1. All DFT calculations suggested that optimization under C_2 symmetry was satisfactory, and in attempts to break the symmetry, the optimization would lead back to approximate C_2. A handful of calculations were also started far away from the optimized structure with respect to tilting and bending of the corrole planes to scan the phase space for other energy minima, but also these optimizations led back to the approximate C_2 structure.

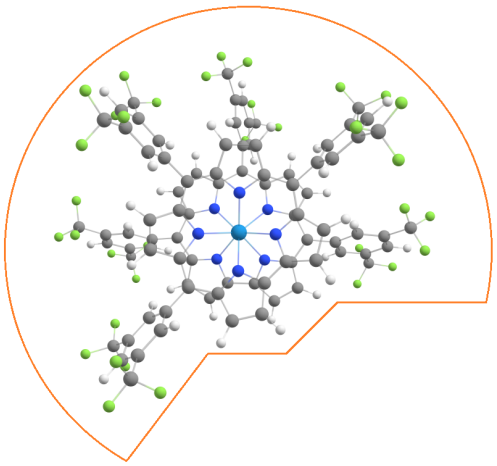

Figure 62. Geometry optimized structure of 45 degree diastereomer of W[T*m*-CF_3PC]$_2$ with peripheral steric crowding marked in orange.

Our perhaps strongest line of reasoning for the loss of C_2 symmetry in W[T*m*-CF_3PC]$_2$ 2 is slightly tilting of the corrole planes, caused by the uneven peripheral steric crowding of the bulky meso-substituents. Tilting of the corrole planes by "pinching" the non-crowded region would therefore create more space in the steric crowded region of the molecule for the meso-substituents to rotate freely. This would lead to small changes in metal-corrole bonds compared to a planar metallobiscorrole, which again could be a reason for the difference in UV-Vis spectra. In fact, if the geometry is slightly distorted by the dynamic behavior, DFT calculations would not capture the full picture as it is a still image of the lowest energy state, which in this case would be misleading. In the case for the 135 degree diastereomer of W[T*m*-CF_3PC]$_2$, there are no obvious regions the sandwich could be "pinched" to allow for relieving of the peripheral steric crowding. Interestingly, the room temperature spectra of W[T*m*-CF_3PC]$_2$ 1 and 2 (Fig. 53 & 54) revealed that W[T*m*-CF_3PC]$_2$ 2 had a greater exchange rate as the coalescence signal (8.3 ppm) was significantly larger - directly indicating that the meso-substituents of W[T*m*-CF_3PC]$_2$ 2 rotated more freely. It is again important to emphasize that the above arguments are mere speculations, and the true nature of the metallobiscorrole sandwiches will likely remain a mystery until a crystal structure is solved.

6.4 Conclusion

Our improved synthetic method has yielded several new metallobiscorrole compounds, where some of them display potential diastereomeric behavior after yielding two analogous compounds, separated by preparative thin-layer chromatography. Previously, one of the

major challenges with the metallobiscorrole framework was the low quality ^{1}H NMR spectra. In this thesis we present a handful of high quality ^{1}H NMR spectra, for the first time revealing the in depth electronic structure of metallobiscorroles. The ^{1}H NMR data also included dynamic effects as the phenyl meso-substituents are found to be rotating about the corrole-phenyl bond, and special anisotropic effects as a result of the unusual coordination motif.

As only one of the compounds was successfully solved by X-ray crystallography, the suggestion of diastereomerism is not fully concluded. There are however no reasonable doubts that the proposed compounds are diastereomers, as all analytical evidence points towards it. As the pair of compounds are separable by preparative thin-layer chromatography, there must exist a difference in electric dipole moment. Mass spectrometry also suggests the pair of compounds to have the identical mass, along with the optical spectrometry which strongly suggests both compounds to be eight-coordinate square antiprismatic complexes. Lastly, the ^{1}H NMR data clearly distinguishes the pair of compounds, while showing direct similarities. Under all these assumptions, there are only two ways to assemble the metallobiscorrole compounds - where one of the compounds has a corrole-corrole rotational angle of 45 degrees and the other has a 135 degrees, where the latter structure was solved by X-ray crystallography.

6.5 Further Work

As of synthetic and analytical concern, the primary motivation for future work within the metallobiscorrole framework remains to successfully crystallize what is proposed as the 45 degree diastereomer. At this time, electron crystallography seems like the most promising option to pursue, as the method can generate high quality diffractions from very small crystals even on nanometer scale, whereas X-ray crystallography generally requires at least millimeter scale crystals.

Application of metallobiscorroles still remains undeveloped, but as an inherently chiral chromophore it has potential applications such as chiral liquid crystals, nonlinear optical materials or chiral sensing.

7 EXPERIMENTAL AND CHARACTERIZATION

7.1 Synthesis and Characterization of Tungsten Biscorroles

7.1.1 Tungsten 5,10,15-tris(pentafluorophenyl) biscorrole

Decalin (10 mL), H_3[TPFPC] (0.065 mmol; i.e., 52 mg), $W(CO)_6$ (0.39 mmol, 137 mg) and potassium carbonate (150 mg) were added to a 50 mL three-necked round-bottom flask equipped with a reflux condenser and a magnetic stirring bar. The contents were deoxygenated with a flow of argon for 1 hour under stirring and then heated at reflux (225 °C) overnight with constant stirring under Ar. Completion of the reaction was indicated by the appearance of a new Q-band absorption in the 780 nm region. The reaction mixture was then loaded directly on to a silica gel column with n-heptane as the mobile phase. The decalin was first removed by eluting with pure n-heptane, and the tungsten biscorrole were then eluted with 3:1 n-heptane/dichloromethane. All fractions with λ_{max} ~780 nm were collected and dried. The resulting crude product was then purified by a second silica gel column with 5:1 n-heptane/dichloromethane as eluent, again collecting all fractions with λ_{max} ~780 nm. The fractions were then dried, before finally purified with preparative thin-layer chromatography with 2:1 n-heptane/dichloromethane as eluent. The tungsten biscorrole showed up as a distinct brown band on thin-layer chromatography. Yields (based on the free-base corrole) and analytical details of the individual complexes are as follows.

W[TPFPC]$_2$: Yield 1.6 mg (2.78 %). ^{1}H NMR (400 MHz, CD_2Cl_2, -85 °C) δ 7.89 (m, 2H), 7.82 (m, 2H), 7.69 (m, 2H), 7.57 (m, 2H), 7.26 (m, 4H), 6.98 (m, 2H), 6.90 (m, 2H). ^{19}F NMR (377 MHz, CD_2Cl_2) δ -128.70 – -132.04 (m, 4F, *o*-F), -137.10 (m, 4F, *o*-F), -153.07 – -153.85 (m, 6F, *p*-F), -161.86 – -162.67 (m, 12F, *m*-F). UV/Vis (CH_2Cl_2): λ_{max} ($\varepsilon\times10^{-4}$): 353 (5.22), 507 (0.66), 788 nm (0.82 M^{-1} cm^{-1});

7.1.2 Tungsten 5,10,15-tris(3,5-bis(trifluoromethyl)phenyl) biscorrole

Decalin (15 mL), H_3[T*m*-CF_3PC] (0.055 mmol; i.e., 51 mg), $W(CO)_6$ (0.33 mmol, 116 mg) and potassium carbonate (150 mg) were added to a 50 mL three-necked round-bottom flask equipped with a reflux condenser and a magnetic stirring bar. The contents were deoxygenated with a flow of argon for 1 hour under stirring and then heated at reflux (240 °C) overnight with constant stirring under Ar. Completion of the reaction was indicated by the appearance of a new Q-band absorption in the 750-800 nm region. The reaction mixture was then loaded directly on to a silica gel column with n-heptane as the mobile phase. The decalin was first removed by eluting with pure n-heptane, and the tungsten biscorrole were then eluted with 3:1 n-heptane/dichloromethane. All fractions with λ_{max} ~770 nm were

collected and dried. The resulting crude product was then purified by a second silica gel column with 10:1 n-heptane/dichloromethane. All fractions with λ_{max} ~770 nm were collected and dried, before a methanol extraction was carried out. The crude product mixture was then finally purified with preparative thin-layer chromatography with 4:1 n-heptane/dichloromethane as eluent. The tungsten biscorrole showed up as a broad brown band on thin-layer chromatography, which upon further analysis resulted in two distinct absorption spectra on UV-Vis. The brown tungsten biscorrole band on thin-layer chromatography was divided in two (top fraction **1**, bottom fraction **2**), and stored separately. Yields (based on the free-base corrole) and analytical details of the individual complexes are as follows.

W[T*m*-CF_3PC]$_2$ 1: Yield 3.2 mg (5.73 %). ^{1}H NMR (400 MHz, CD_2Cl_2) δ 9.40 (s, 1H, 5- or 15-o), 9.26 (s, 2H, 10-o), 8.42 (s, 3H, 5,15-o), 8.31 (s, 4H, 5,15-p), 8.19 (s, 2H, 10-p), 8.00 (d, *J* = 4.6 Hz, 2H, β-H), 7.93 (d, *J* = 4.6 Hz, 2H, β-H), 7.81 (d, *J* = 4.6 Hz, 2H, β-H), 7.75 (d, *J* = 4.6 Hz, 2H, β-H), 7.43 (d, *J* = 4.9 Hz, 2H, β-H), 7.35 (d, *J* = 4.8 Hz, 2H, β-H), 7.30 (d, *J* = 4.8 Hz, 2H, β-H), 7.21 (s, 2H, 10-o), 7.08 (d, *J* = 4.7 Hz, 2H, β-H). ^{19}F NMR (377 MHz, $CDCl_3$) δ -62.19 – -63.42 (m). UV/Vis (CH_2Cl_2): λ_{max} ($\varepsilon\times10^{-4}$): 358 (8.02), 509 (1.05), 780 nm (0.98 M^{-1} cm^{-1});

W[T*m*-CF_3PC]$_2$ 2: Yield 2.7 mg (4.83 %). ^{1}H NMR (400 MHz, CD_2Cl_2) δ 9.28 (s, 1H, 10-*o*), 8.43 (s, 6H, 5,10,15-*o*), 8.33 – 8.25 (m, 4H, 5,15-*p*), 8.19 (s, 1H, 10-*p*), 8.17 (s, 1H, 10-*o*), 8.01 (d, *J* = 4.6 Hz, 1H, β-H), 7.97 (d, *J* = 4.6 Hz, 1H, β-H), 7.94 (d, *J* = 4.6 Hz, 1H, β-H), 7.88 (d, *J* = 4.7 Hz, 1H, β-H), 7.81 (d, *J* = 4.6 Hz, 1H, β-H), 7.78 (d, *J* = 4.6 Hz, 1H, β-H), 7.75 (d, *J* = 4.6 Hz, 1H, β-H), 7.70 (d, *J* = 4.7 Hz, 1H, β-H), 7.58 (d, *J* = 4.7 Hz, 1H, β-H), 7.43 (d, *J* = 4.9 Hz, 1H, β-H), 7.38 – 7.33 (m, 3H, β-H), 7.31 (d, *J* = 4.8 Hz, 1H, β-H), 7.21 (s, 1H, 10-o), 7.12 (d, *J* = 4.7 Hz, 1H, β-H), 7.08 (d, *J* = 4.7 Hz, 1H, β-H), 7.02 (s, 1H), 6.91 (s, 1H). ^{19}F NMR (377 MHz, $CDCl_3$) δ -62.18 – -63.42 (m). UV/Vis (CH_2Cl_2): λ_{max} ($\varepsilon\times10^{-4}$): 359 (5.12), 506 (0.74), 760 nm (0.63 M^{-1} cm^{-1});

7.1.3 Tungsten 5,10,15-tris(3,5-dimethoxyphenyl) biscorrole

Decalin (15 mL), H_3[T*m*-OCH_3PC] (0.197 mmol; i.e., 139 mg), $W(CO)_6$ (1.18 mmol, 415 mg) and potassium carbonate (300 mg) were added to a 50 mL three-necked round-bottom flask equipped with a reflux condenser and a magnetic stirring bar. The contents were deoxygenated with a flow of argon for 1 hour under stirring and then heated at reflux (225 °C) overnight with constant stirring under Ar. Completion of the reaction was indicated by the appearance of a new Q-band absorption in the 750-800 nm region. The reaction mixture was then loaded directly onto a silica gel column with n-heptane as the mobile phase. The

decalin was first removed by eluting with pure n-heptane, and the tungsten biscorrole were then eluted with 10:1 n-heptane/acetone. All fractions with λ_{max} ~750 nm were collected and dried. The resulting crude product was then purified by two consecutive heptane extractions, before finally purified with two consecutive preparative thin-layer chromatography with 1:1 and 3:2 n-heptane/acetone as eluent. The tungsten biscorrole showed up as a brown band with a red impurity hugging from below on preparative thin-layer chromatography. Upon further investigation, the upper and lower brown band resulted in two distinct UV-Vis spectra. The brown tungsten biscorrole band was then divided in two (top fraction **1**, bottom fraction **2**), and stored separately. Yields (based on the free-base corrole) and analytical details of the individual complexes are as follows.

W[T*m*-OCH$_3$PC]$_2$ 1: Yield 1.8 mg (1.15 %). ^{1}H NMR (400 MHz, CD_2Cl_2) δ 7.8-6.3 (m), 4.4 – 3.5 (m). UV/Vis (CH2Cl2): λ_{max} ($\varepsilon\times10^{-4}$): 358 (5.66), 502 (1.03), 782 nm (0.66 M^{-1} cm^{-1});

Crystallization of W[T*m*-OCH$_3$PC]$_2$ 1: A small amount, approximately 1 mg of W[T*m*-OCH$_3$PC]$_2$ 1 was dissolved in 500 µl chloroform and transferred to a 1 ml vial. The vial was then sealed with a screw cap, but not tightened to let the solvent undergo slow evaporation. Over the course of a week, all solvent had evaporated and deposited crystals in the vial.

Crystallography of W[T*m*-OCH$_3$PC]$_2$ 1: Several crystal samples of different metallobiscorrole compounds were sent to Advanced Light Source at Lawrence Berkeley National Laboratory for X-ray crystallography, where only the above sample gave interpretable diffraction.

W[T*m*-OCH$_3$PC]$_2$ 2: Yield 1.1 mg (0.70 %). ^{1}H NMR (400 MHz, CD_2Cl_2) δ 7.8-6.3 (m), 4.4 – 3.5 (m). UV/Vis (CH_2Cl_2): λ_{max} ($\varepsilon\times10^{-4}$): 356 (4.27), 502 (0.84), 731 nm (0.46), 782 nm (0.34 M^{-1} cm^{-1});

7.1.4 Tungsten 5,10,15-tris(2,6-dichlorophenyl) biscorrole

Dichlorobenzene (20 mL), H$_3$[T*o*-ClPC] (0.165 mmol; i.e., 121 mg), W(CO)$_6$ (0.97 mmol, 340 mg) and potassium carbonate (350 mg) were added to a 50 mL three-necked round-bottom flask equipped with a reflux condenser and a magnetic stirring bar. The contents were deoxygenated with a flow of argon for 1 hour under stirring and then heated at reflux (225 °C) overnight with constant stirring under Ar. The reaction mixture was then loaded directly onto a silica gel column with n-heptane as the mobile phase. The dichlorobenzene was first removed by eluting with pure n-heptane, and the tungsten biscorrole were then eluted with

methanol. All fractions with λ_{max} ~750-800 nm were collected and dried. The resulting crude product was then purified by an additional silica gel column eluted with 3:1 n-heptane:dichloromethane. As the yields were incredibly low, the product was not amenable to full characterization.

W[T*o*-ClPC]$_2$: Confirmed by UV-Vis and mass spectrometry.

7.1.5 Tungsten 5,10,15-tris(2,6-dimethoxyphenyl) biscorrole

Decalin (10 mL), H_3[T*o*-OCH_3PC] (0.035 mmol; i.e., 25 mg), $W(CO)_6$ (0.105 mmol, 37 mg) and potassium carbonate (75 mg) were added to a 50 mL three-necked round-bottom flask equipped with a reflux condenser and a magnetic stirring bar. The contents were deoxygenated with a flow of argon for 1 hour under stirring and then heated at reflux (225 °C) overnight with constant stirring under Ar. The reaction mixture was then loaded directly onto a silica gel column with n-heptane as the mobile phase. The decalin was first removed by eluting with pure n-heptane, and the tungsten biscorrole were then eluted with 1:1 n-heptane:dichloromethane. All fractions with λ_{max} ~750-800 nm were collected and dried. The resulting crude product was then purified by an additional silica gel column eluted with 3:1 n-heptane:dichloromethane. As the yields were incredibly low, the product was not amenable to full characterization.

W[T*o*-OCH_3PC]$_2$: Confirmed by UV-Vis and mass spectrometry.

7.2 Synthesis and Characterization of Molybdenum Biscorroles

7.2.1 Molybdenum 5,10,15-tris(pentafluorophenyl) biscorrole

Dichlorobenzene (10 mL), H_3[TPFPC] (0.027 mmol; i.e., 22 mg), $Mo(CO)_6$ (0.14 mmol, 36 mg) and potassium carbonate (50 mg) were added to a 50 mL three-necked round-bottom flask equipped with a reflux condenser and a magnetic stirring bar. The contents were deoxygenated with a flow of argon for 1 hour under stirring and then heated at reflux (225 °C) overnight with constant stirring under Ar. The reaction mixture was then loaded directly onto a silica gel column with n-heptane as the mobile phase. The dichlorobenzene was first removed by eluting with pure n-heptane, and the molybdenum biscorrole were then eluted with 1:1 n-heptane:dichloromethane. All fractions with λ_{max} ~900 nm were collected and dried. The resulting crude product was then purified by an additional silica gel column eluted with 3:1 n-heptane:dichloromethane. As the yields were incredibly low, the product was not amenable to full characterization.

Mo[TPFPC]$_2$: Confirmed by UV-Vis and mass spectrometry.

7.2.2 Molybdenum 5,10,15-tris(3,5-bis(trifluoromethyl)phenyl) biscorrole

Decalin (10 mL), H_3[T*m*-CF_3PC] (0.043 mmol; i.e., 39.6 mg), $Mo(CO)_6$ (0.265 mmol, 70 mg) and potassium carbonate (150 mg) were added to a 50 mL three-necked round-bottom flask equipped with a reflux condenser and a magnetic stirring bar. The contents were deoxygenated with a flow of argon for 1 hour under stirring and then heated at reflux (225 °C) overnight with constant stirring under Ar. Completion of the reaction was indicated by the appearance of a new Q-band absorption in the 900 nm region. The reaction mixture was then loaded directly on to a silica gel column with n-heptane as the mobile phase. The decalin was first removed by eluting with pure n-heptane, and the molybdenum biscorrole were then eluted with 6:2:1 n-heptane/dichloromethane/acetone. All fractions with λ_{max} ~900 nm were collected and dried. The crude product mixture was then finally purified with two consecutive preparative thin-layer chromatography with 4:1 n-heptane/dichloromethane and 10:2:1 n-heptane/dichloromethane/acetone as eluent. The molybdenum biscorrole showed up as a broad brown band on thin-layer chromatography, which upon further analysis resulted in two distinct absorption spectra on UV-Vis. The brown molybdenum biscorrole band on thin-layer chromatography was divided in two (top fraction **1**, bottom fraction **2**), and stored separately. Yields (based on the free-base corrole) and analytical details of the individual complexes are as follows.

Mo[T*m*-CF_3PC]$_2$ 1: Yield 9.6 mg (6.77 %). ^{1}H NMR (400 MHz, CD_2Cl_2) δ 8.52 (s, 2H, 10-o), 8.13 (s, 4H, 5- and 15-o), 8.06 (s, 4H, 5- and 15-p), 7.93 (s, 2H, 10-p), 7.47 (d, *J* = 4.7 Hz, 2H, β-H), 7.30 (s, 2H, β-H), 7.23 (s, 2H, β-H), 7.15 (s, 4H, β-H), 6.57 (s, 6H, β-H), 6.33 (s, 2H, 10-o); UV/Vis (CH_2Cl_2): λ_{max} (ε×10^{-4}): 359 (3.45), 437 (1.22), 923 nm (0.49 M^{-1} cm^{-1}).

Mo[T*m*-CF_3PC]$_2$ 2: Yield 5.2 mg (3.66 %). ^{1}H NMR (400 MHz, CD_2Cl_2) δ 8.43 (s, 3H), 8.17 (s, 4H, 5- and 15-o), 8.11 (s, 4H, 5- and 15-o), 8.06 (s, 2H, 5- or 15-p), 8.02 (s, 2H, 5- or 15-p), 7.95 (s, 2H, 10-p), 7.31 (m), 7.15 (m), 6.95 – 6.41 (m); UV/Vis (CH_2Cl_2): λ_{max} (ε×10^{-4}): 360 (5.31),430 (1.49), 895 nm (0.84 M^{-1} cm^{-1});

7.2.3 Molybdenum 5,10,15-tris(2-thiophene) biscorrole

Trichlorobenzene (12 mL), H_3[T2-TC] (0.257 mmol; i.e., 140 mg), $Mo(CO)_6$ (1.54 mmol, 407 mg) and potassium carbonate (500 mg) were added to a 50 mL three-necked round-bottom

flask equipped with a reflux condenser and a magnetic stirring bar.The contents were deoxygenated with a flow of argon for 1 hour under stirring and then heated at reflux (225 °C) overnight with constant stirring under Ar. Completion of the reaction was indicated by the appearance of a new Q-band absorption in the 900 nm region. The reaction mixture was then loaded directly on to a silica gel column with n-heptane as the mobile phase. The trichlorobenzene was first removed by eluting with pure n-heptane, and the molybdenum biscorrole were then eluted with 3:1 n-heptane/dichloromethane. All fractions with λ_{max} ~900 nm were collected and dried. The resulting crude product was then purified by an additional silica gel column eluted with 2:1 n-heptane:dichloromethane. The crude product mixture was then finally purified with preparative thin-layer chromatography with 10:2:1 n-heptane/dichloromethane/acetone as eluent. Yields (based on the free-base corrole) and analytical details of the individual complexes are as follows.

Mo[T2-TPC]$_2$: Yield 4.3 mg (2.84 %). ^{1}H NMR (400 MHz, CD_2Cl_2) δ 8.98 (s), 7.88 – 6.60 (m). UV/Vis (CH_2Cl_2): λ_{max} ($\varepsilon\times10^{-4}$): 364 (3.57), 426 (2.06), 912 nm (0.57 M^{-1} cm^{-1});

7.3 Computational Method

7.3.1 Geometry Optimization of W[T*m*-CF_3PC]$_2$

All ADF calculations were done in collaboration with Prof. Jeanet Conradie.

Density functional theory study on the compounds (45 and 135 degree diastereomers) was done in the gas phase under C_2 symmetry with the scalar relativistic ZORA (Zeroth Order Regular Approximation to the Dirac equation) Hamiltonian[94] [95] [96], and the OLYP[97] [98] exchange-correlation functional, including Grimme's D3 dispersion correction.[99] The STO ZORA TZ2P all-electron relativistic basis set was used, together with a strict convergence criteria and a grid of 6 were used during the geometry optimization. All other details as implemented in the ADF 2019 program.[100] [101]

7.3.2 Chemical Shielding Analysis of W[T*m*-CF_3PC]$_2$

Chemical shielding of *o*-phenyl rotation was studied by using an already geometry optimized structure from section 7.3.1. A series of ghost atoms with a spacing of 15 degrees were implemented in the rotational trajectory of the *o*-phenyl hydrogens of one of the 10-meso position substituents. The phenyl group was then rotated to an unnatural flat configuration with respect to the corrole plane to reduce interference with the ghost atoms. NMR calculations were then carried out in the Gaussian 16 program[102] together with the

B3LYP[103] [97] [104] [105] exchange-correlation functional and Def2-TZVP basis set.[106] All other details as implemented in the Gaussian 16 program.

Iso-chemical shielding surfaces (ICSS) was studied to see how the aromaticity of the biscorrole scaffold behaves under an external magnetic field by introducing ghost atoms with a spacing of 0.5 Å in a 20 x 20 x 20 Å grid (e.g. 64 000 ghost atoms) around the biscorrole structure with pyAroma.[107] The geometry optimized structure from section 7.3.1 was used, but meso-substituents were replaced by hydrogens to reduce interferences with the ICSS map. The NMR calculations were then carried out similarly to the chemical shielding calculations above, and the visual ICSS was generated in ChimeraX.[108]

7.3.3 SpinWorks 4 NMR Simulation

To investigate dynamic NMR properties of the studied biscorroles, the SpinWorks 4 NMR simulation tool[109] was used together with the built-in MEXICO simulation algorithm, with appropriately setup spin systems with respect to the studied molecules. The exchange rate *k* was adjusted to reflect the physical exchange between δ_A and δ_B states, which is temperature dependent.

References

(1) Bury, C. R. LANGMUIR'S THEORY OF THE ARRANGEMENT OF ELECTRONS IN ATOMS AND MOLECULES. Journal of the American Chemical Society 1921, 43 (7), 1602-1609.

(2) Periodic Table. https://ptable.com/#Electrons/OxidationStates (accessed.

(3) Z., E. s,p,d,f Orbitals. 2013; Vol. 2023.

(4) Hausinger, R. P. Fe (II)/α-ketoglutarate-dependent hydroxylases and related enzymes. Critical reviews in biochemistry and molecular biology 2004, 39 (1), 21-68.

(5) Kutzelnigg, W. Hans Bethe (1906–2005) and Ligand Field Theory. 2005.

(6) Griffith, J.; Orgel, L. Ligand-field theory. Quarterly Reviews, Chemical Society 1957, 11 (4), 381-393.

(7) Hass, K. 4.1.2: Introduction to Ligand Field Theory (Octahedral complexes). 2020; Vol. 2023.

(8) Pollice, R.; Friederich, P.; Lavigne, C.; dos Passos Gomes, G.; Aspuru-Guzik, A. Organic molecules with inverted gaps between first excited singlet and triplet states and appreciable fluorescence rates. Matter 2021, 4 (5), 1654-1682.

(9) Darensbourg, M. Y. Transition Metal Coordination Chemistry. Chemistry 362: Spring 2019. Vol. 2023.

(10) Berg, J. M.; Tymoczko, J. L.; Stryer, L. Biochemistry; 2006.

(11) Fischer, H. Chlorophyll. Chemical Reviews 1937, 20 (1), 41-68.

(12) Perutz, M. Structure of hemoglobin. In Brookhaven symposia in biology, 1960; Vol. 13, pp 165-183.

(13) Einrem, R. F. New Building Blocks for Cancer Phototherapeutics: 5d Metallocorroles. 2022. (accessed 5 October 2023).

(14) Nobelprize.org. Hans Fischer Facts. https://www.nobelprize.org/prizes/chemistry/1930/fischer/facts/ (accessed 2023 5 October).

(15) Lindsey, J. S.; Schreiman, I. C.; Hsu, H. C.; Kearney, P. C.; Marguerettaz, A. M. Rothemund and Adler-Longo reactions revisited: synthesis of tetraphenylporphyrins under equilibrium conditions. The Journal of Organic Chemistry 1987, 52 (5), 827-836.

(16) Gomes, C.; Peixoto, M.; Pineiro, M. Modern Methods for the Sustainable Synthesis of

Metalloporphyrins. Molecules 2021, 26 (21), 6652.

(17) Adler, A. D.; Longo, F. R.; Kampas, F.; Kim, J. On the preparation of metalloporphyrins. Journal of Inorganic and Nuclear Chemistry 1970, 32 (7), 2443-2445.

(18) Dean, M. L.; Schmink, J. R.; Leadbeater, N. E.; Brückner, C. Microwave-promoted insertion of Group 10 metals into free base porphyrins and chlorins: scope and limitations. Dalton Transactions 2008, (10), 1341-1345.

(19) Kingsbury, C. J.; Senge, M. O. The shape of porphyrins. Coordination Chemistry Reviews 2021, 431, 213760.

(20) Alemayehu, A. B.; Gonzalez, E.; Hansen, L. K.; Ghosh, A. Copper corroles are inherently saddled. Inorganic chemistry 2009, 48 (16), 7794-7799.

(21) Thomas, K. E.; Conradie, J.; Hansen, L. K.; Ghosh, A. Corroles cannot ruffle. Inorganic Chemistry 2011, 50 (8), 3247-3251.

(22) Scott, E. E.; He, Y. A.; Wester, M. R.; White, M. A.; Chin, C. C.; Halpert, J. R.; Johnson, E. F.; Stout, C. D. An open conformation of mammalian cytochrome P450 2B4 at 1.6-Å resolution. Proceedings of the National Academy of Sciences 2003, 100 (23), 13196-13201.

(23) Nebert, D. W.; Russell, D. W. Clinical importance of the cytochromes P450. The Lancet 2002, 360 (9340), 1155-1162.

(24) Spigset, O. Cytokrom P-450-systemet. Tidsskriftet 2001.

(25) Torstensen, K. Cytochrome P450 Monooxygenase. 2023.

(26) Rittle, J.; Green, M. T. Cytochrome P450 compound I: capture, characterization, and CH bond activation kinetics. Science 2010, 330 (6006), 933-937.

(27) Kumar, A.; Kim, D.; Kumar, S.; Mahammed, A.; Churchill, D. G.; Gross, Z. Milestones in corrole chemistry: historical ligand syntheses and post-functionalization. Chemical Society Reviews 2023.

(28) Gross, Z.; Galili, N.; Saltsman, I. The first direct synthesis of corroles from pyrrole. Angewandte Chemie International Edition 1999, 38 (10), 1427-1429.

(29) Nurco, D. J.; Smith, K. M. 5, 10, 15-Triphenylcorrole: a product from a modified Rothemund reaction. Chemical Communications 1999, (14), 1307-1308.

(30) Gryko, D. T.; Koszarna, B. Refined methods for the synthesis of meso-substituted A 3-and trans-A 2 B-corroles. Organic & biomolecular chemistry 2003, 1 (2), 350-357.

(31) Koszarna, B.; Gryko, D. T. Efficient synthesis of meso-substituted corroles in a H2O− MeOH mixture. The Journal of organic chemistry 2006, 71 (10), 3707-3717.

(32) Steene, E.; Dey, A.; Ghosh, A. β-Octafluorocorroles. Journal of the American Chemical Society 2003, 125 (52), 16300-16309.

(33) Geier, G. R.; Chick, J. F. B.; Callinan, J. B.; Reid, C. G.; Auguscinski, W. P. A survey of acid catalysis and oxidation conditions in the two-step, one-flask synthesis of meso-substituted corroles via dipyrromethanedicarbinols and pyrrole. The Journal of Organic Chemistry 2004, 69 (12), 4159-4169.

(34) Paolesse, R.; Marini, A.; Nardis, S.; Froiio, A.; Mandoj, F.; Nurco, D. J.; Prodi, L.; Montalti, M.; Smith, K. M. Novel routes to substituted 5, 10, 15-triarylcorroles. Journal of Porphyrins and Phthalocyanines 2003, 7 (01), 25-36.

(35) Gust, D.; Moore, T.; Kadish, K.; Smith, K.; Guilard, R. The Porphyrin Handbook. Academic Press, San Diego, CA 2000, 8, 153-190.

(36) Alemayehu, A. B.; Gagnon, K. J.; Terner, J.; Ghosh, A. Oxidative metalation as a route to size‐mismatched macrocyclic complexes: Osmium corroles. Angewandte Chemie International Edition 2014, 53 (52), 14411-14414.

(37) Vazquez-Lima, H.; Conradie, J.; Johansen, M. A.; Martinsen, S. R. I.; Alemayehu, A. B.; Ghosh, A. Heavy-element–ligand covalence: ligand noninnocence in molybdenum and tungsten Viking-helmet Corroles. Dalton Transactions 2021, 50 (37), 12843-12849.

(38) Buckley, H. L.; Chomitz, W. A.; Koszarna, B.; Tasior, M.; Gryko, D. T.; Brothers, P. J.; Arnold, J. Synthesis of lithium corrole and its use as a reagent for the preparation of cyclopentadienyl zirconium and titanium corrole complexes. Chemical Communications 2012, 48 (87), 10766-10768.

(39) Albrett, A. M.; Thomas, K. E.; Maslek, S.; Młodzianowska, A.; Conradie, J.; Beavers, C. M.; Ghosh, A.; Brothers, P. J. Mono-and diboron corroles: factors controlling stoichiometry and hydrolytic reactivity. Inorganic Chemistry 2014, 53 (11), 5486-5493.

(40) Majumder, S.; Borah, B. P.; Bhuyan, J. Rhenium in the core of porphyrin and rhenium bound to the periphery of porphyrin: synthesis and applications. Dalton Transactions 2020, 49 (25), 8419-8432.

(41) Mahammed, A.; Gross, Z. Aluminum corrolin, a novel chlorophyll analogue. Journal of Inorganic biochemistry 2002, 88 (3-4), 305-309.

(42) Weaver, J. J.; Sorasaenee, K.; Sheikh, M.; Goldschmidt, R.; Tkachenko, E.; Gross, Z.; Gray, H. B. Gallium (III) corroles. Journal of Porphyrins and Phthalocyanines 2004, 8 (01), 76-81.

(43) Schöfberger, W.; Lengwin, F.; Reith, L. M.; List, M.; Knör, G. n. Lead corrole complexes in solution: Powerful multielectron transfer reagents for redox catalysis. Inorganic Chemistry Communications 2010, 13 (10), 1187-1190.

(44) Padilla, R.; Buckley, H. L.; Ward, A. L.; Arnold, J. Synthesis, structure and reactivity of

group 4 corrole complexes. Chemical Communications 2014, 50 (22), 2922-2924.

(45) Meier-Callahan, A. E.; Di Bilio, A. J.; Simkhovich, L.; Mahammed, A.; Goldberg, I.; Gray, H. B.; Gross, Z. Chromium corroles in four oxidation states. Inorganic chemistry 2001, 40 (26), 6788-6793.

(46) Padilla, R.; Buckley, H. L.; Ward, A. L.; Arnold, J. Preparation and characterization of a tungsten (V) corrole dichloride complex. Journal of Porphyrins and Phthalocyanines 2015, 19 (01n03), 150-153.

(47) Ganguly, S.; McCormick, L. J.; Conradie, J.; Gagnon, K. J.; Sarangi, R.; Ghosh, A. Electronic structure of manganese corroles revisited: X-ray structures, optical and X-ray absorption spectroscopies, and electrochemistry as probes of ligand noninnocence. Inorganic Chemistry 2018, 57 (16), 9656-9669.

(48) Einrem, R. F.; Braband, H.; Fox, T.; Vazquez‐Lima, H.; Alberto, R.; Ghosh, A. Synthesis and molecular structure of 99Tc Corroles. Chemistry–A European Journal 2016, 22 (52), 18747-18751.

(49) Einrem, R. F.; Gagnon, K. J.; Alemayehu, A. B.; Ghosh, A. Metal–ligand misfits: facile access to rhenium–oxo corroles by oxidative metalation. Chemistry–A European Journal 2016, 22 (2), 517-520.

(50) Alemayehu, A. B.; McCormick-McPherson, L. J.; Conradie, J.; Ghosh, A. Rhenium Corrole Dimers: Electrochemical Insights into the Nature of the Metal–Metal Quadruple Bond. Inorganic Chemistry 2021, 60 (11), 8315-8321.

(51) Collman, J. P.; Harford, S.; Franzen, S.; Eberspacher, T.; Shoemaker, R. K.; Woodruff, W. H. Spectroscopic Comparisons of MoW (porphyrin) 2 Heterodimers with Homologous Mo2 and W2 Quadruple Bonds: A Dynamic NMR and Resonance Raman Study. Journal of the American Chemical Society 1998, 120 (7), 1456-1465.

(52) Collman, J. P.; Woo, L. K. Rotational barrier of a molybdenum-molybdenum quadruple bond. Proceedings of the National Academy of Sciences 1984, 81 (8), 2592-2596.

(53) Joseph, C. A.; Lee, M. S.; Iretskii, A. V.; Wu, G.; Ford, P. C. Substituent effects on nitrosyl iron corrole complexes Fe (Ar3C)(NO). Inorganic chemistry 2006, 45 (5), 2075-2082.

(54) Simkhovich, L.; Goldberg, I.; Gross, Z. The effects of bulky ortho-aryl substituents in corroles, tested by X-ray crystallography of the rhodium complexes and catalysis thereby. Journal of Porphyrins and Phthalocyanines 2002, 6 (06), 439-444.

(55) Kadish, K. M.; Burdet, F.; Jérôme, F. o.; Barbe, J.-M.; Ou, Z.; Shao, J.; Guilard, R. Synthesis, physicochemical and electrochemical properties of metal–metal bonded ruthenium corrole homodimers. Journal of organometallic chemistry 2002, 652 (1-2), 69-76.

(56) Alemayehu, A. B.; McCormick, L. J.; Vazquez-Lima, H.; Ghosh, A. Relativistic Effects on a Metal–Metal Bond: Osmium Corrole Dimers. Inorganic chemistry 2019, 58 (4), 2798-2806.

(57) Ganguly, S.; Conradie, J.; Bendix, J.; Gagnon, K. J.; McCormick, L. J.; Ghosh, A. Electronic structure of cobalt–corrole–pyridine complexes: noninnocent five-coordinate Co (II) corrole–radical states. The Journal of Physical Chemistry A 2017, 121 (50), 9589-9598.

(58) Saltsman, I.; Simkhovich, L.; Balazs, Y.; Goldberg, I.; Gross, Z. Synthesis, spectroscopy, and structures of new rhodium (I) and rhodium (III) corroles and catalysis thereby. Inorganica chimica acta 2004, 357 (10), 3038-3046.

(59) Thomassen, I. K.; McCormick-McPherson, L. J.; Borisov, S. M.; Ghosh, A. Iridium corroles exhibit weak near-infrared phosphorescence but efficiently sensitize singlet oxygen formation. Scientific reports 2020, 10 (1), 7551.

(60) Will, S.; Lex, J.; Vogel, E.; Schmickler, H.; Gisselbrecht, J. P.; Haubtmann, C.; Bernard, M.; Gorss, M. Nickel and Copper Corroles: Well‐Known Complexes in a New Light. Angewandte Chemie International Edition in English 1997, 36 (4), 357-361.

(61) Chen, Q. C.; Fridman, N.; Diskin‐Posner, Y.; Gross, Z. Palladium complexes of corroles and sapphyrins. Chemistry–A European Journal 2020, 26 (43), 9481-9485.

(62) Alemayehu, A. B.; Vazquez-Lima, H.; Beavers, C. M.; Gagnon, K. J.; Bendix, J.; Ghosh, A. Platinum corroles. Chemical Communications 2014, 50 (76), 11093-11096.

(63) Thomas, K. E.; Alemayehu, A. B.; Conradie, J.; Beavers, C.; Ghosh, A. Synthesis and molecular structure of gold triarylcorroles. Inorganic Chemistry 2011, 50 (24), 12844-12851.

(64) Schweyen, P.; Brandhorst, K.; Wicht, R.; Wolfram, B.; Bröring, M. The corrole radical. Angewandte Chemie 2015, 127 (28), 8331-8334.

(65) Jérôme, F. o.; Billier, B. a.; Barbe, J. M.; Espinosa, E.; Dahaoui, S.; Lecomte, C.; Guilard, R. Evidence for the formation of a RuIII− RuIII bond in a ruthenium corrole homodimer. Angewandte Chemie International Edition 2000, 39 (22), 4051-4053.

(66) Obies, M.; Hussein, A. A. The nature of metal–metal bonding in Re-, Ru-and Os-corrole dimers. RSC advances 2022, 12 (29), 18728-18735.

(67) Collman, J. P.; Barnes, C. E.; Woo, L. K. Systematic variation of metal—metal bond order in metalloporphyrin dimers. Proceedings of the National Academy of Sciences 1983, 80 (24), 7684-7688.

(68) Alemayehu, A. B.; Vazquez-Lima, H.; Gagnon, K. J.; Ghosh, A. Tungsten Biscorroles: New Chiral Sandwich Compounds. Chemistry-a European Journal 2016, 22 (20), 6914-6920. DOI: 10.1002/chem.201504848.

(69) Alemayehu, A. B.; Vazquez-Lima, H.; McCormick, L. J.; Ghosh, A. Relativistic effects in metallocorroles: comparison of molybdenum and tungsten biscorroles. Chemical Communications 2017, 53 (43), 5830-5833. DOI: 10.1039/c7cc01549f.

(70) Alemayehu, A. B.; Abernathy, M. J.; Conradie, J.; Sarangi, R.; Ghosh, A. Rhenium Biscorrole Sandwich Compounds: XAS Evidence for a New Coordination Motif. Inorganic Chemistry 2023.

(71) Moscowitz, A. Advances in Chemical Physics, edited by I. Prigogine Vol. IV. 1962.

(72) Berova, N.; Polavarapu, P. L.; Nakanishi, K.; Woody, R. W. Comprehensive Chiroptical Spectroscopy, Volume 2: Applications in Stereochemical Analysis of Synthetic Compounds, Natural Products, and Biomolecules; 2012.

(73) Claridge, T. D. W. High-Resolution NMR Techniques in Organic Chemistry; 2009.

(74) Nowick, J. S. Organic Spectroscopy 203. 2011. http://ocw.uci.edu/courses/chem_203_organic_spectroscopy.html (accessed 2023 31. October).

(75) T.Yamazaki, M. N., T.Saito, T.Yamaji, K.Hayamizu, M.Yanagisawa and O.Yamamoto. Spectral Database for Organic Compounds SDBS. 2023. (accessed 2023 30.10.2023).

(76) Allred, A. L. Electronegativity Values from Thermochemical Data. Journal of Inorganic & Nuclear Chemistry 1961, 17 (3-4), 215-221. DOI: Doi 10.1016/0022-1902(61)80142-5.

(77) Cavaleiro, J. A. " Solvent" effects in 1H NMR spectroscopy: A simple undergraduate experiment. Journal of Chemical Education 1987, 64 (6), 549.

(78) Clayden, J.; Greeves, N.; Warren, S. Organic Chemistry; 2012.

(79) Ross, B. D.; True, N. S. NMR spectroscopy of cyclohexane. Gas-phase conformational kinetics. Journal of the American Chemical Society 1983, 105 (15), 4871-4875.

(80) Gasparro, F. P.; Kolodny, N. H. NMR determination of the rotational barrier in N, N-dimethylacetamide. A physical chemistry experiment. Journal of Chemical Education 1977, 54 (4), 258.

(81) Duhamel, P.; Vetterli, M. Fast Fourier transforms: a tutorial review and a state of the art. Signal processing 1990, 19 (4), 259-299.

(82) Gupta, R. K.; Ferretti, J. A.; Becker, E. D. Rapid scan Fourier transform NMR spectroscopy. Journal of Magnetic Resonance (1969) 1974, 13 (3), 275-290.

(83) Kong, Q.; Siauw, T.; Bayen, A. Python programming and numerical methods: A guide for engineers and scientists; 2020.

(84) Taton, A. Dynaimc Effects on NMR Spectra. http://www1.chem.umn.edu/groups/taton/chem8361/Handouts/9_26.pdf (accessed 2023 18th November).

(85) Koch, W.; Holthausen, M. C. A chemist's guide to density functional theory; 2015.

(86) Repisky, M. Computational Chemistry – Density Functional Theory (KJE-8102/3102). 2022.

(87) Helgaker, T. The Role of the Hohenberg–Kohn Theorem in Density-Functional Theory. 2016. https://trygvehelgaker.no/Presentations/GrandForks_2016.pdf (accessed 2023 9th November).

(88) Cramer, C. J. Essentials of computational chemistry: theories and models; 2013.

(89) Jensen, F. Introduction to computational chemistry; 2017.

(90) Sousa, S. r. F.; Fernandes, P. A.; Ramos, M. J. General performance of density functionals. The Journal of Physical Chemistry A 2007, 111 (42), 10439-10452.

(91) Pitzer, K. S. Relativistic effects on chemical properties. Accounts of Chemical Research 1979, 12 (8), 271-276.

(92) Facelli, J. C. Chemical shift tensors: Theory and application to molecular structural problems. Progress in nuclear magnetic resonance spectroscopy 2011, 58 (3-4), 176.

(93) El Bakouri, O.; Szczepanik, D. W.; Jorner, K.; Ayub, R.; Bultinck, P.; Solà, M.; Ottosson, H. Three-Dimensional Fully π-Conjugated Macrocycles: When 3D-Aromatic and When 2D-Aromatic-in-3D? Journal of the American Chemical Society 2022, 144 (19), 8560-8575.

(94) Lenthe, E. v.; Baerends, E.-J.; Snijders, J. G. Relativistic regular two-component Hamiltonians. The Journal of chemical physics 1993, 99 (6), 4597-4610.

(95) van Lenthe, E.; Baerends, E.-J.; Snijders, J. G. Relativistic total energy using regular approximations. The Journal of chemical physics 1994, 101 (11), 9783-9792.

(96) Van Lenthe, E.; Ehlers, A.; Baerends, E.-J. Geometry optimizations in the zero order regular approximation for relativistic effects. The Journal of chemical physics 1999, 110 (18), 8943-8953.

(97) Handy, N. C.; Cohen, A. J. Left-right correlation energy. Molecular Physics 2001, 99 (5), 403-412.

(98) Lee, C. T.; Yang, W. T.; Parr, R. G. Development of the Colle-Salvetti Correlation-Energy Formula into a Functional of the Electron-Density. Physical Review B 1988, 37 (2), 785-789. DOI: DOI 10.1103/PhysRevB.37.785.

(99) Grimme, S.; Antony, J.; Ehrlich, S.; Krieg, H. A consistent and accurate ab initio parametrization of density functional dispersion correction (DFT-D) for the 94 elements H-Pu. Journal of Chemical Physics 2010, 132 (15). DOI: Artn 154104
Pmid 20423165
10.1063/1.3382344.

(100) te Velde, G.; Bickelhaupt, F. M.; Baerends, E. J.; Guerra, C. F.; Van Gisbergen, S. J. A.; Snijders, J. G.; Ziegler, T. Chemistry with ADF. Journal of Computational Chemistry 2001, 22 (9), 931-967. DOI: DOI 10.1002/jcc.1056.

(101) Fonseca Guerra, C.; Snijders, J.; Te Velde, G. t.; Baerends, E. J. Towards an order-N DFT method. Theoretical Chemistry Accounts 1998, 99, 391-403.

(102) Gaussian 16 Rev. C.01; 2016. (accessed.

(103) Becke, A. D. Density-Functional Thermochemistry .1. The Effect of the Exchange-Only Gradient Correction. Journal of Chemical Physics 1992, 96 (3), 2155-2160. DOI: Doi 10.1063/1.462066.

(104) Vosko, S. H.; Wilk, L.; Nusair, M. Accurate Spin-Dependent Electron Liquid Correlation Energies for Local Spin-Density Calculations - a Critical Analysis. Canadian Journal of Physics 1980, 58 (8), 1200-1211. DOI: DOI 10.1139/p80-159.

(105) Stephens, P. J.; Devlin, F. J.; Chabalowski, C. F.; Frisch, M. J. Ab-Initio Calculation of Vibrational Absorption and Circular-Dichroism Spectra Using Density-Functional Force-Fields. Journal of Physical Chemistry 1994, 98 (45), 11623-11627. DOI: DOI 10.1021/j100096a001.

(106) Weigend, F.; Ahlrichs, R. Balanced basis sets of split valence, triple zeta valence and quadruple zeta valence quality for H to Rn: Design and assessment of accuracy. Physical Chemistry Chemical Physics 2005, 7 (18), 3297-3305.

(107) Wang, Z. py.Aroma 4. https://wongzit.github.io/program/pyaroma/. (acccessed 18th Dec. 2023).

(108) Meng, E. C.; Goddard, T. D.; Pettersen, E. F.; Couch, G. S.; Pearson, Z. J.; Morris, J. H.; Ferrin, T. E. UCSF ChimeraX: Tools for structure building and analysis. Protein Science 2023, 32 (11), e4792.

(109) Marat, K. SpinWorks. 2006.

APPENDIX

100 - W[TPFPC]$_2$

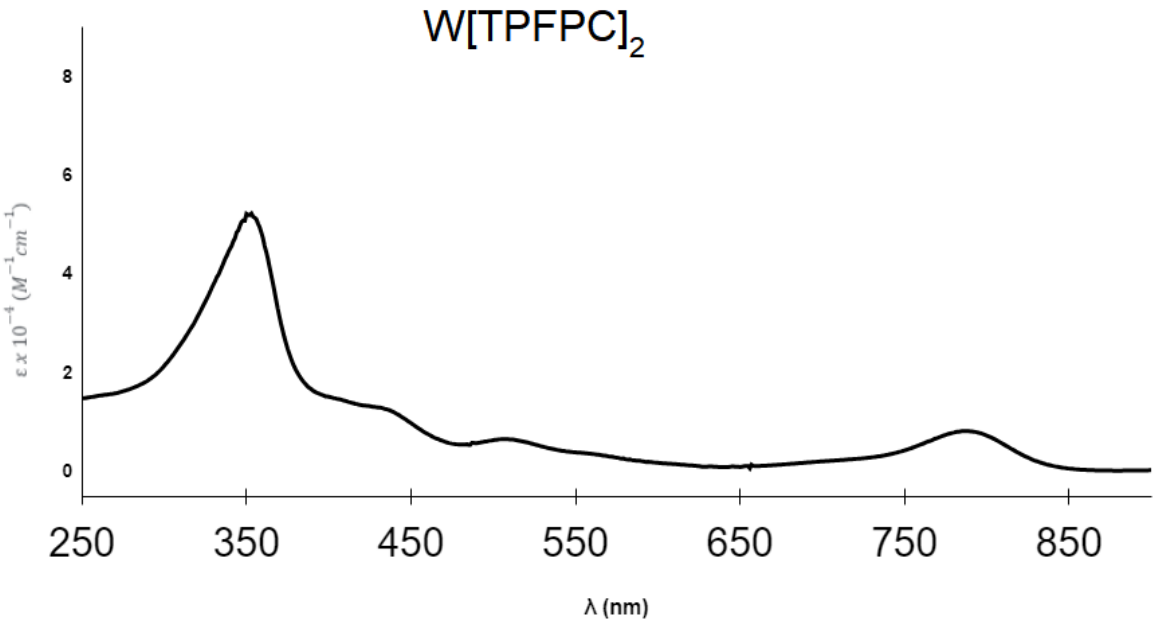

Figure 100. UV-Vis spectrum of W[TPFPC]$_2$ in dichloromethane.

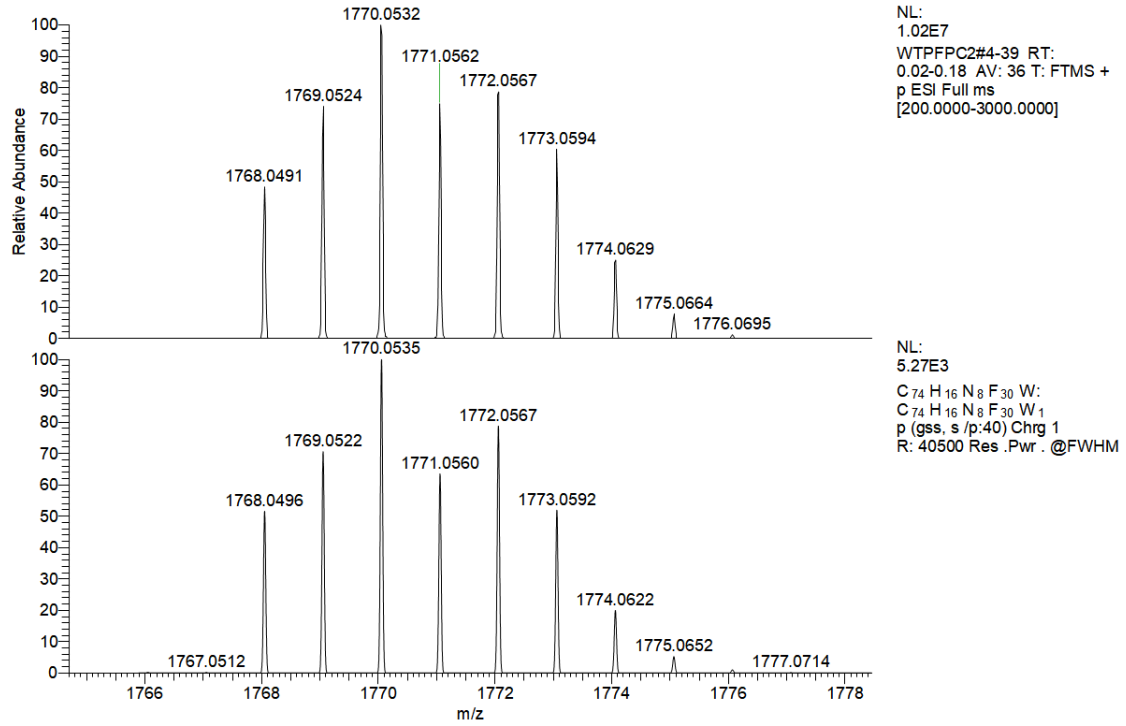

Figure 101. Mass spectrometry of W[TPFPC]$_2$ (top) and theoretical mass spectrometry of W[TPFPC]$_2$ (bottom).

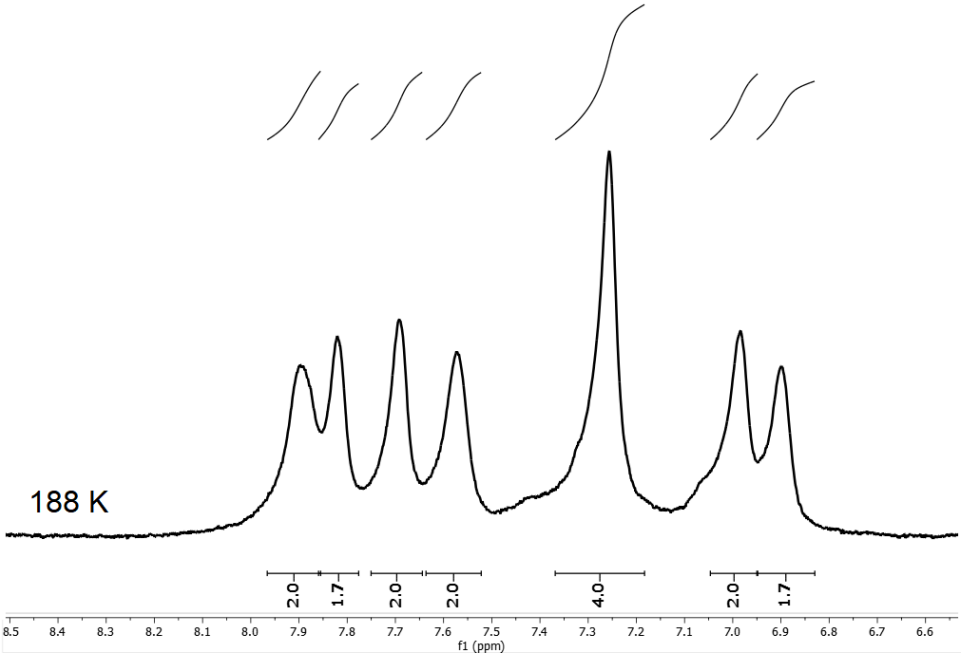

Figure 102. ^{1}H NMR spectrum of W[TPFPC]$_2$ in dichloromethane at 188 K.

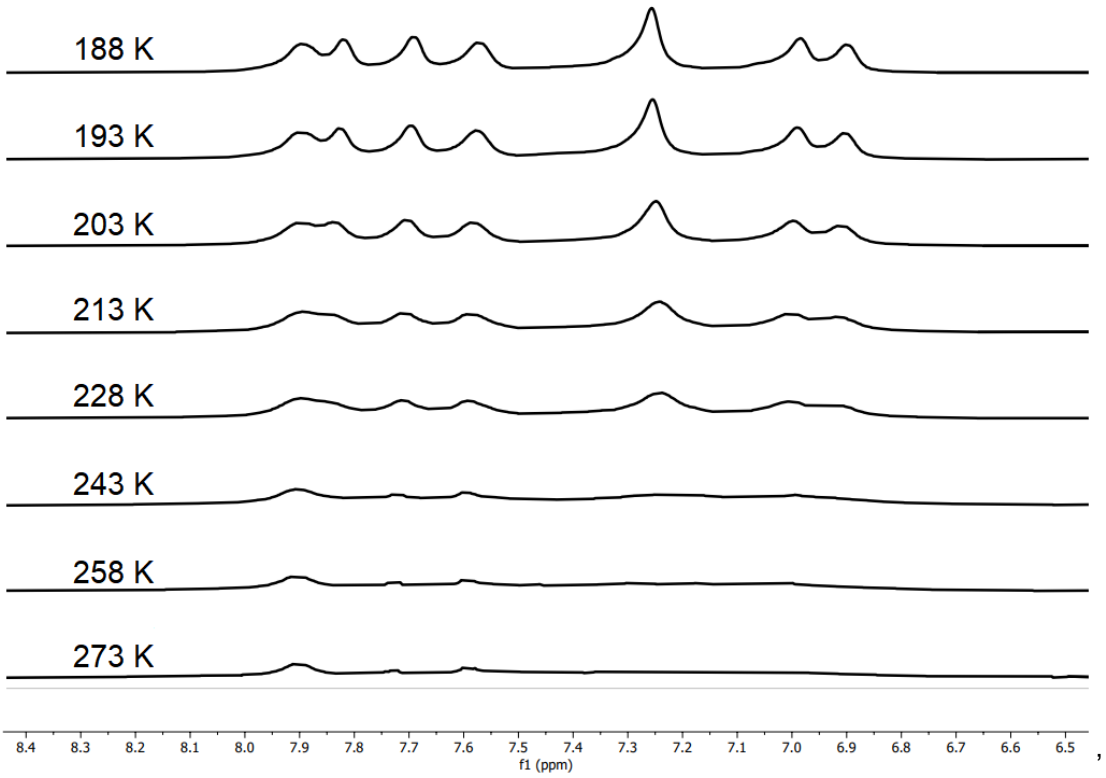

Figure 103. Variable temperature ^{1}H NMR spectrum of W[TPFPC]$_2$ in dichloromethane.

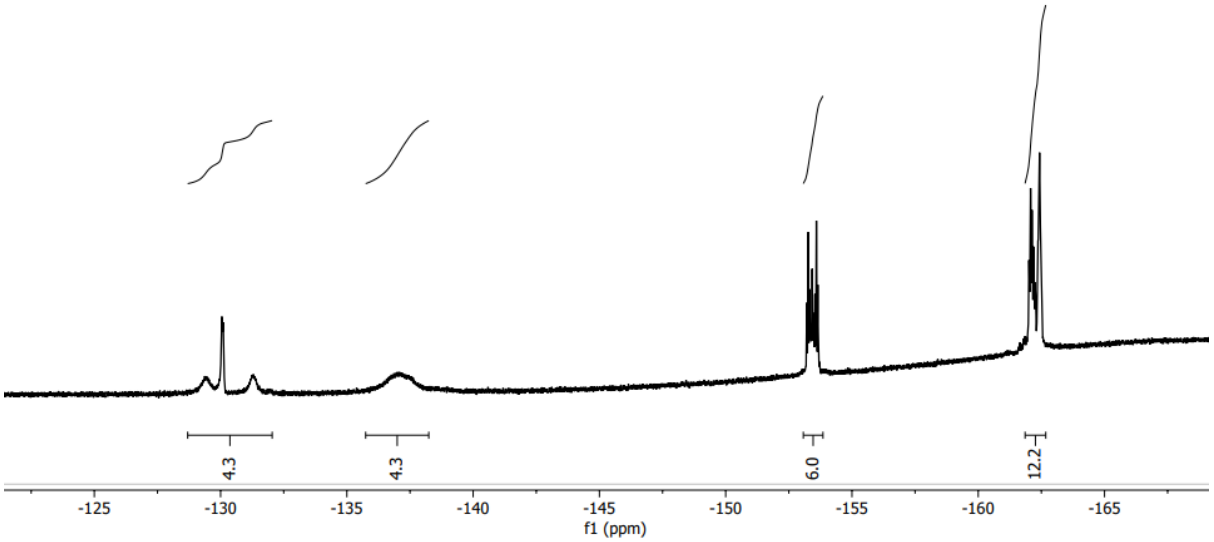

Figure 104. ^{19}F NMR spectrum of W[TPFPC]$_2$ in dichloromethane at room temperature.

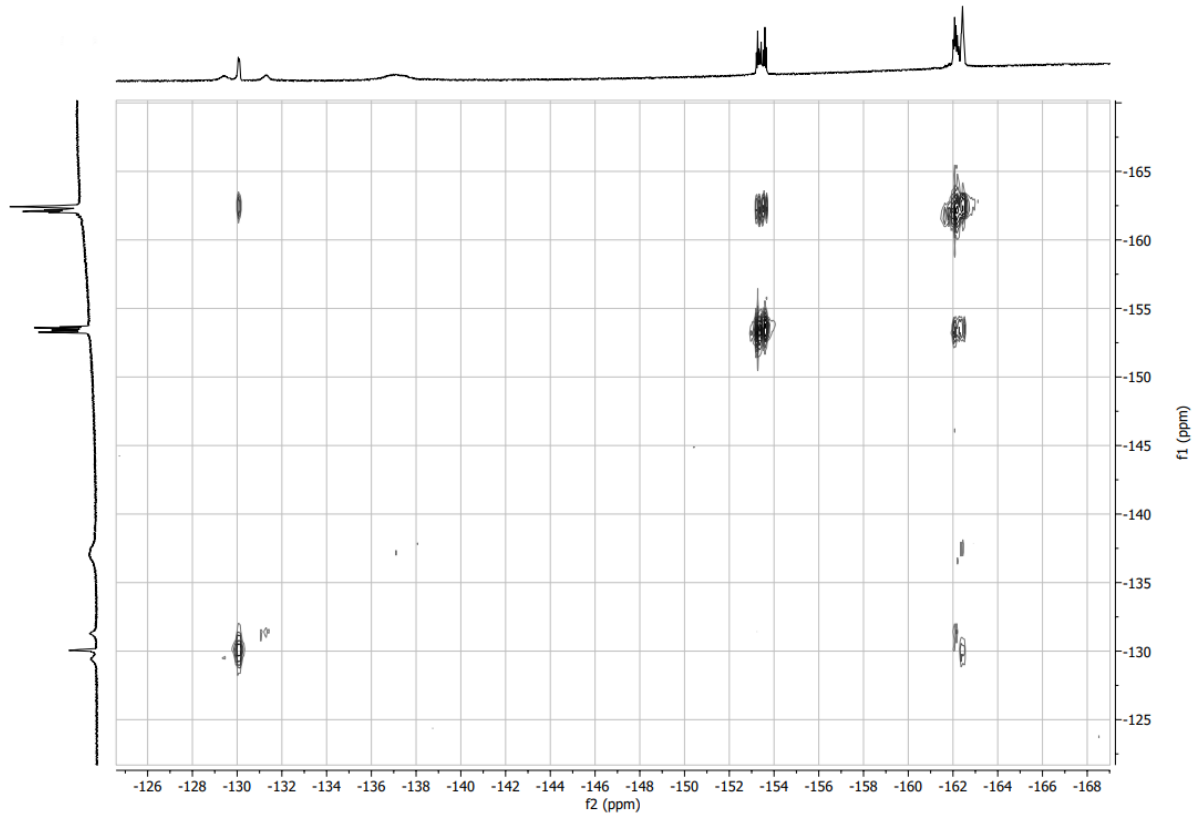

Figure 104. ^{19}F-^{19}F COSY NMR spectrum of W[TPFPC]$_2$ in dichloromethane at room temperature.

200 - W[T*m*-CF_3PC]$_2$ 1

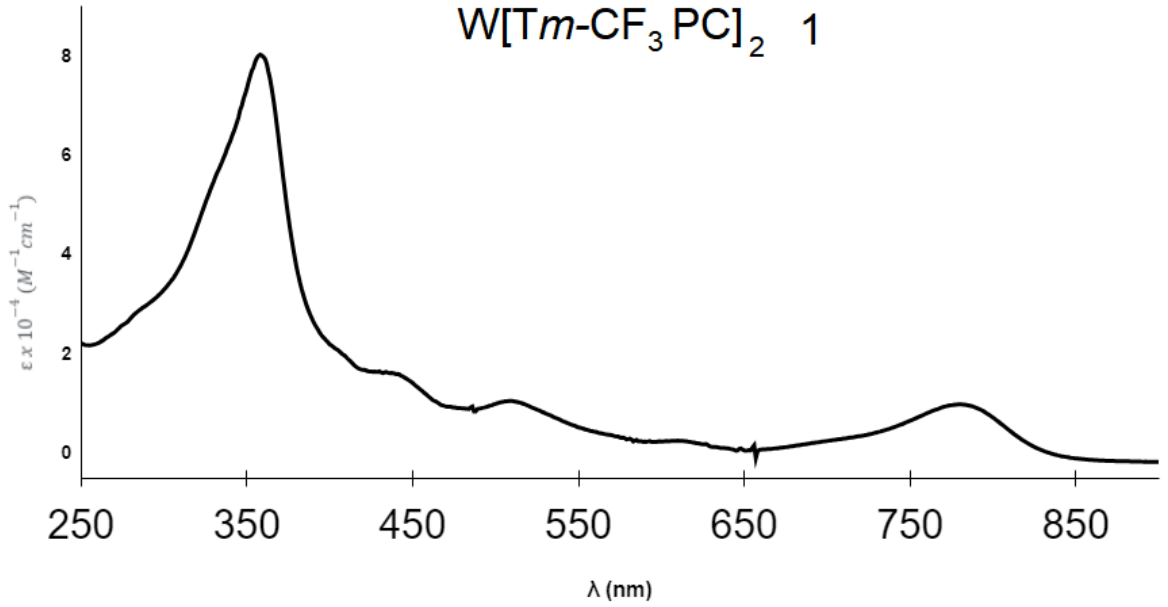

Figure 200. UV-Vis spectrum of W[T*m*-CF_3PC]$_2$ 1 in dichloromethane.

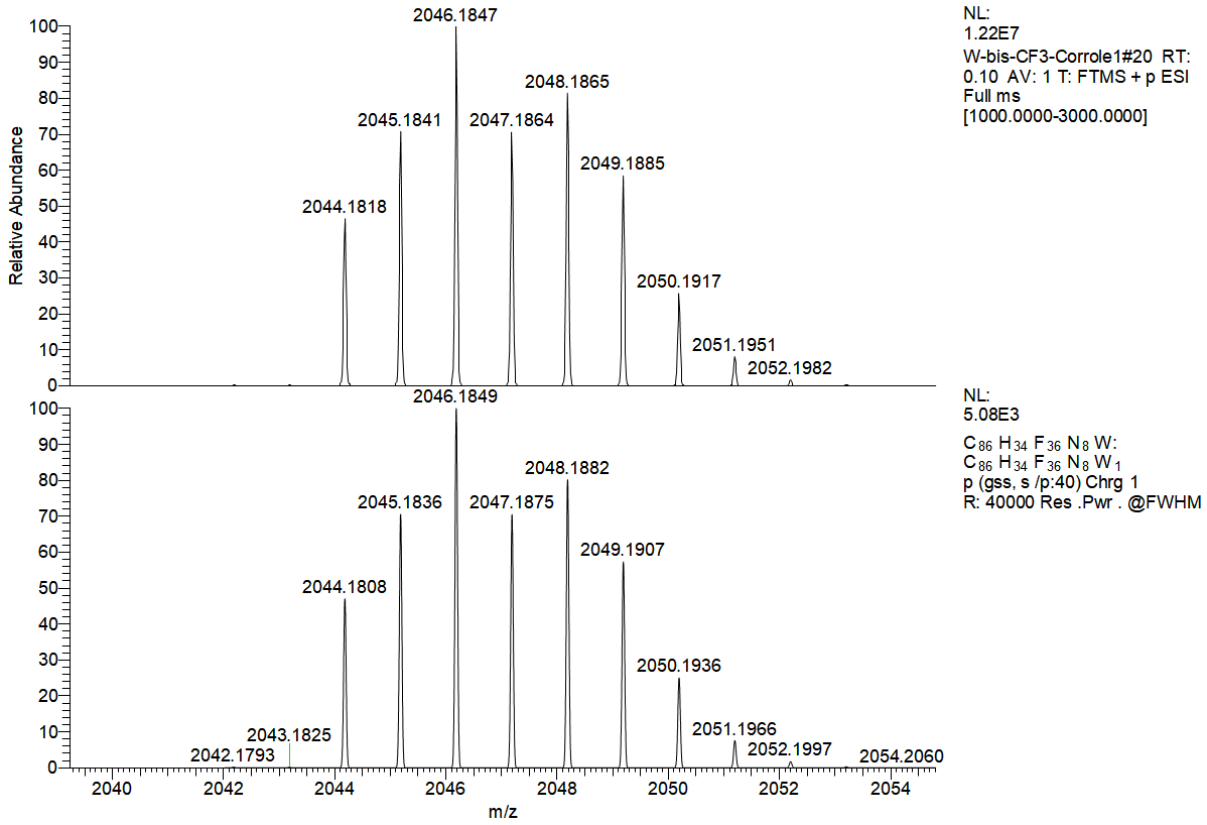

Figure 201. Mass spectrometry of W[T*m*-CF_3PC]$_2$ 1 (top) and theoretical mass spectrometry of W[T*m*-CF_3PC]$_2$ (bottom).

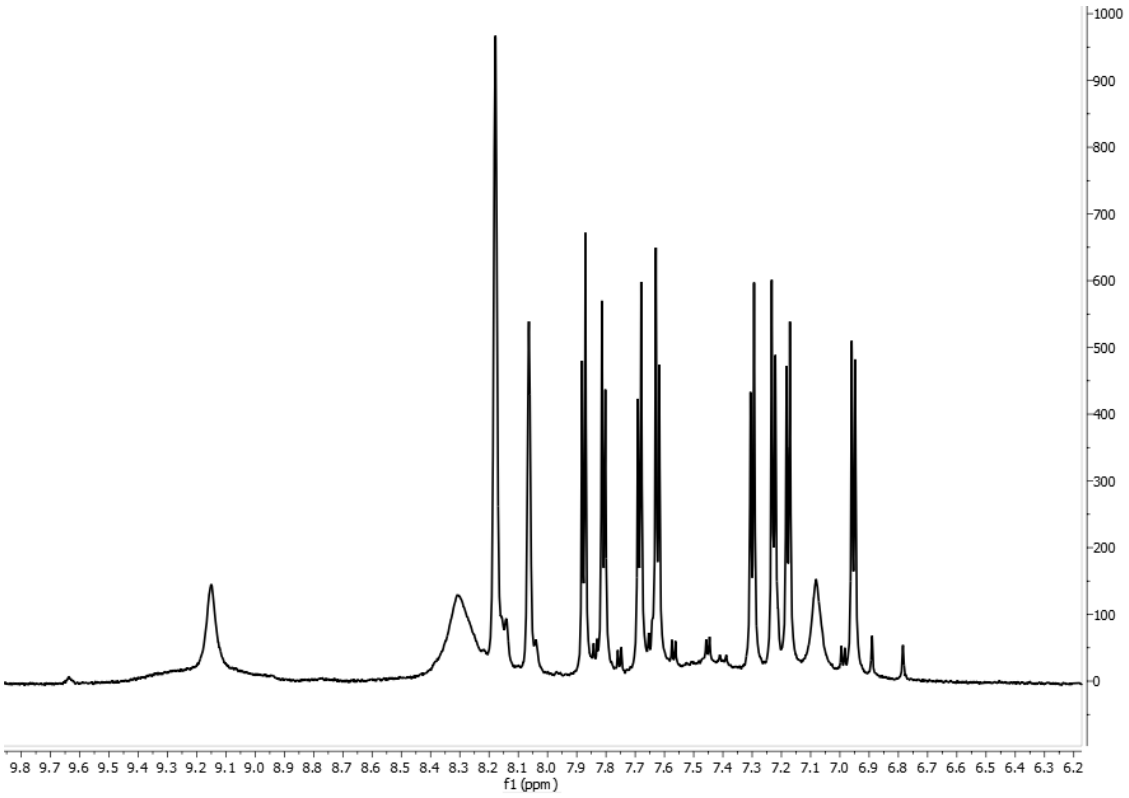

Figure 202. ^{1}H NMR spectrum of W[T*m*-CF_3PC]$_2$ 1 in dichloromethane at room temperature.

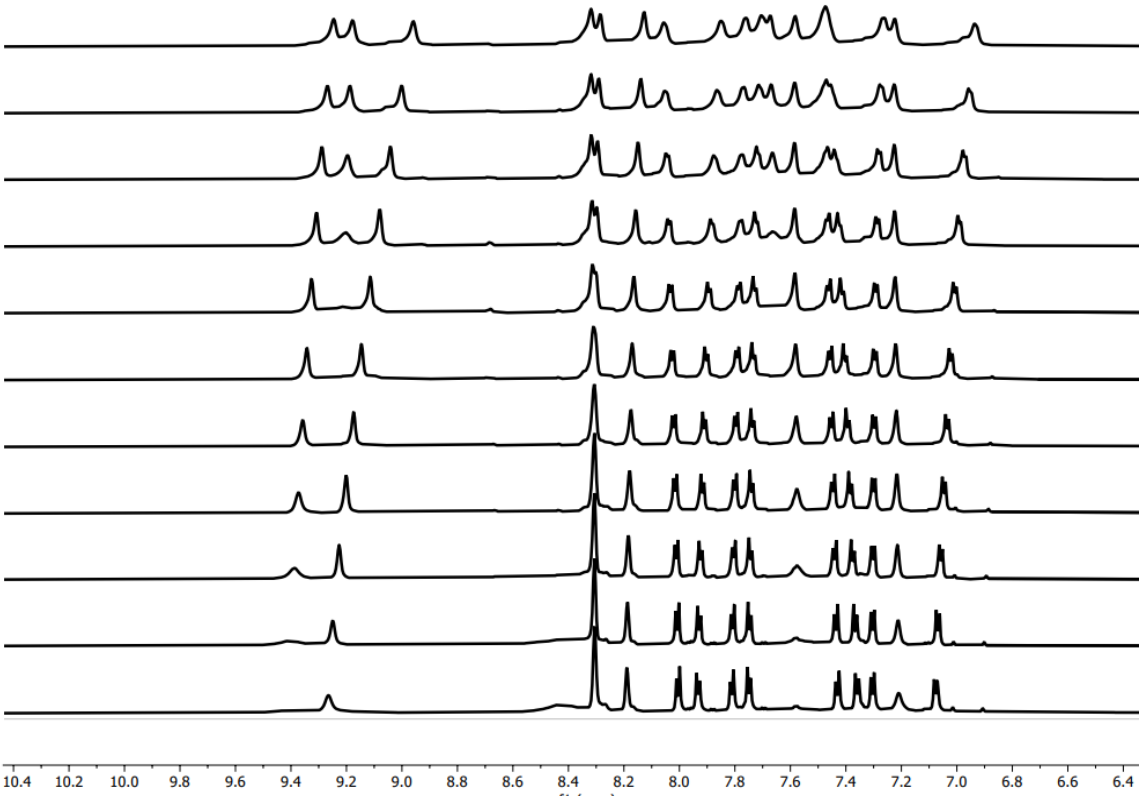

Figure 203. Variable temperature ^{1}H NMR of W[T*m*-CF_3PC]$_2$ **1** in CH_2Cl_2, 193 K (top) to 293 K (bottom) in increment of 10 K.

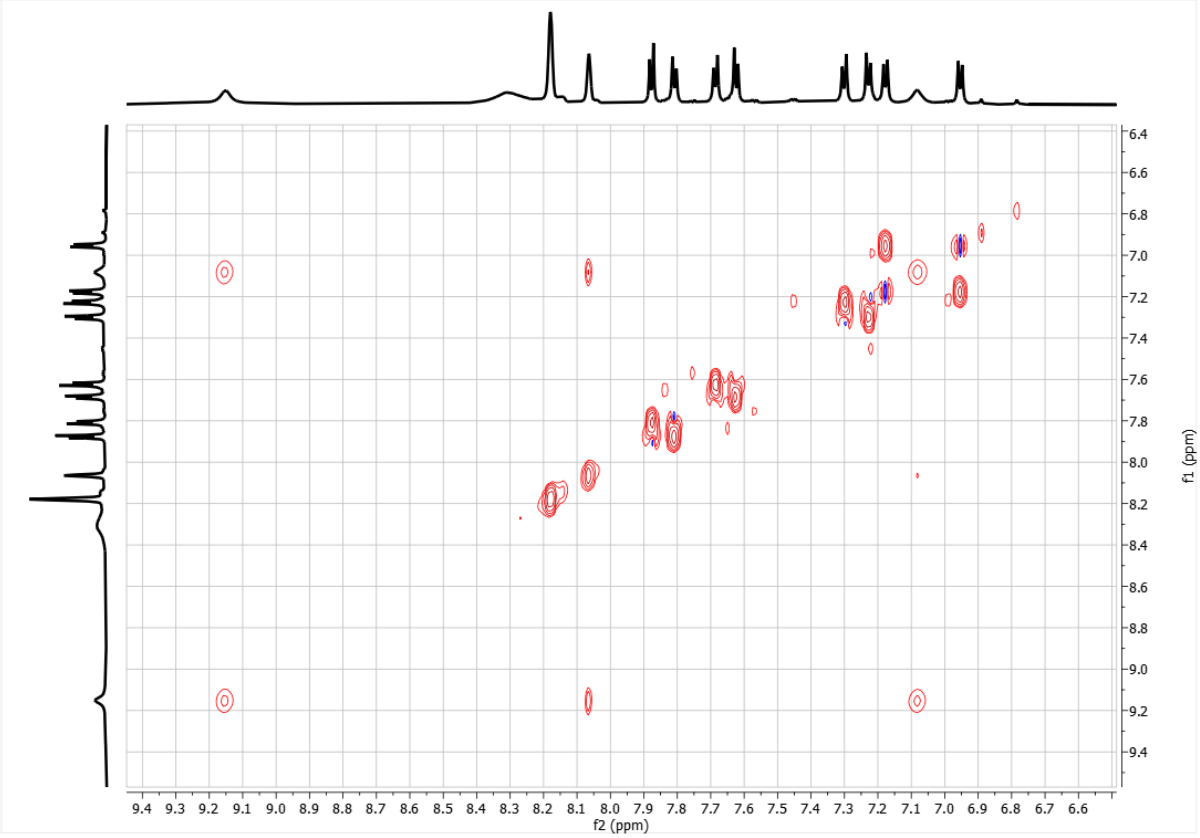

Figure 204. ^{1}H TOCSY NMR of W[T*m*-CF_3PC]$_2$ 1 in dichloromethane.

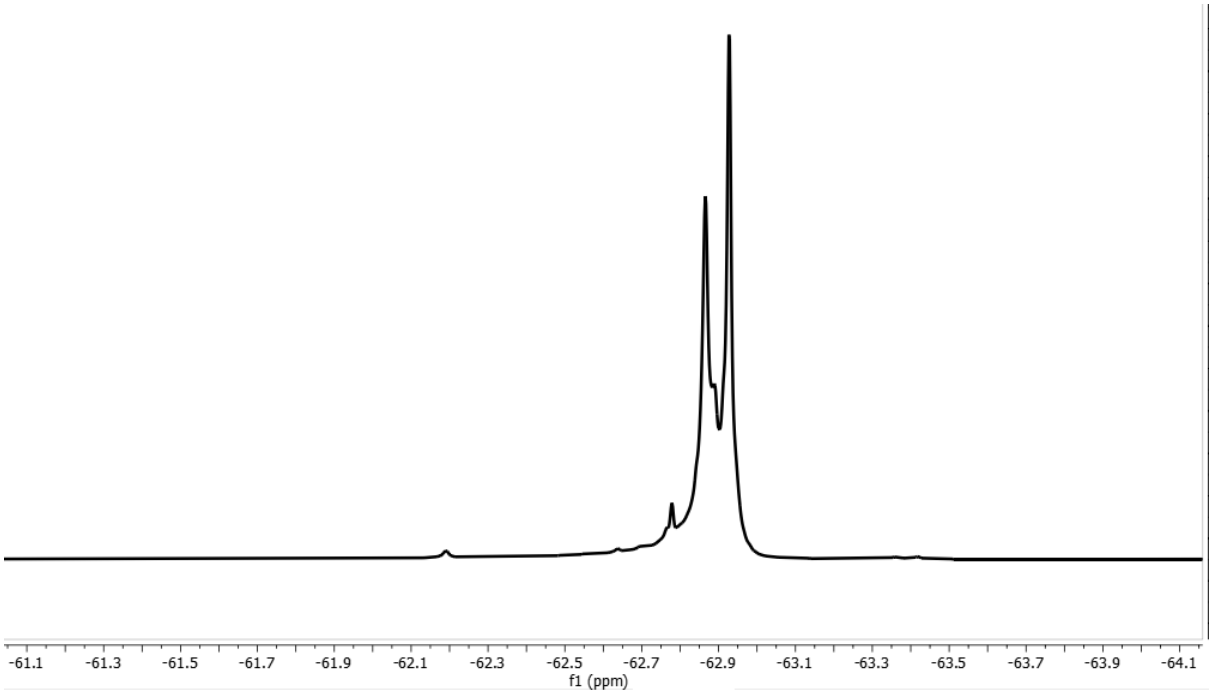

Figure 205. ^{19}F NMR spectrum of W[T*m*-CF_3PC]$_2$ 1 in dichloromethane at room temperature.

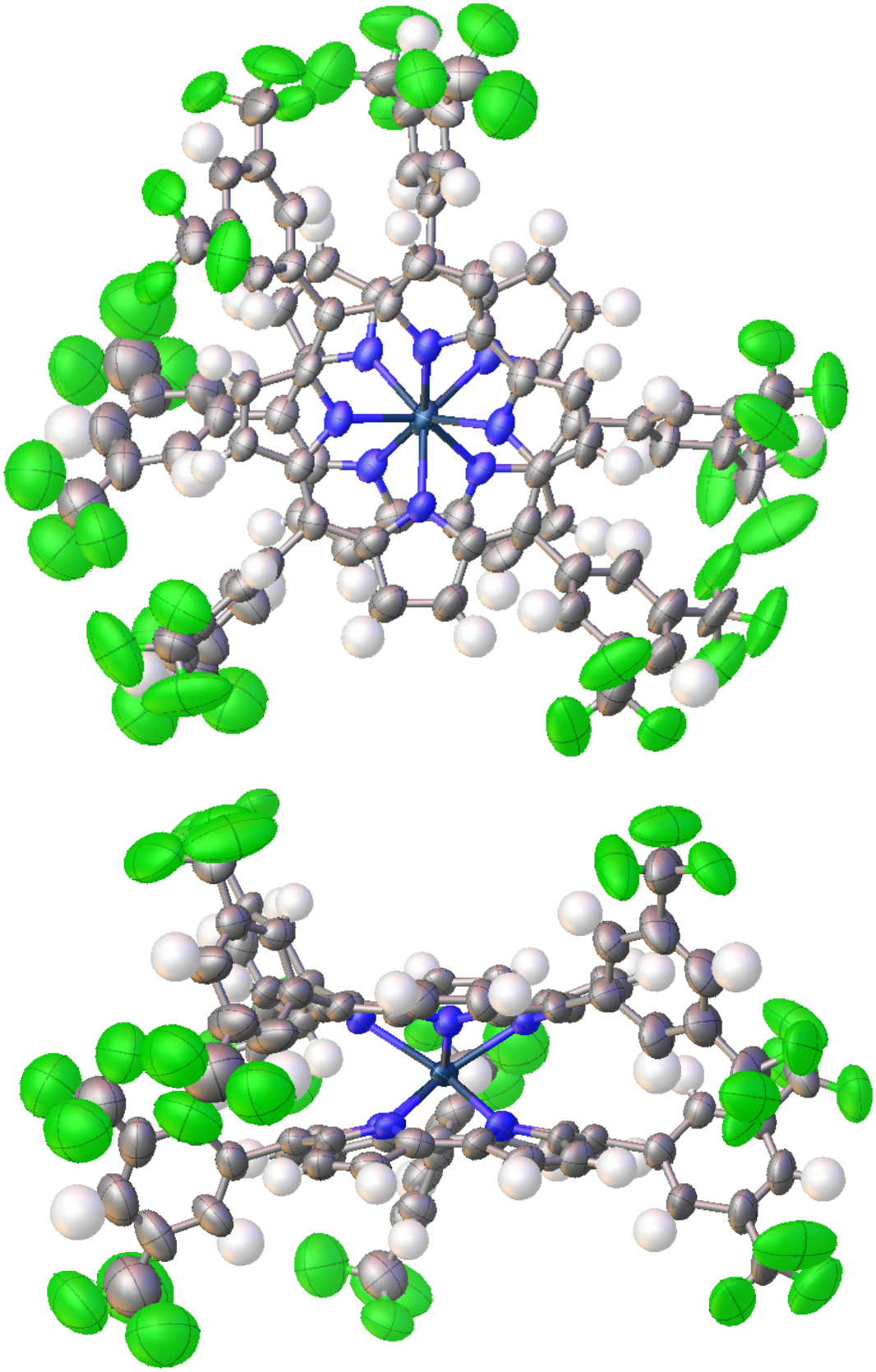

Figure 206. Thermal ellipsoid plots (25 %) for W[T*m*-CF_3PC]$_2$ 1 crystal structure solved at Advanced Light Source, Lawrence Berkeley National Laboratory.

300 - W[T*m*-CF_3PC]$_2$ 2

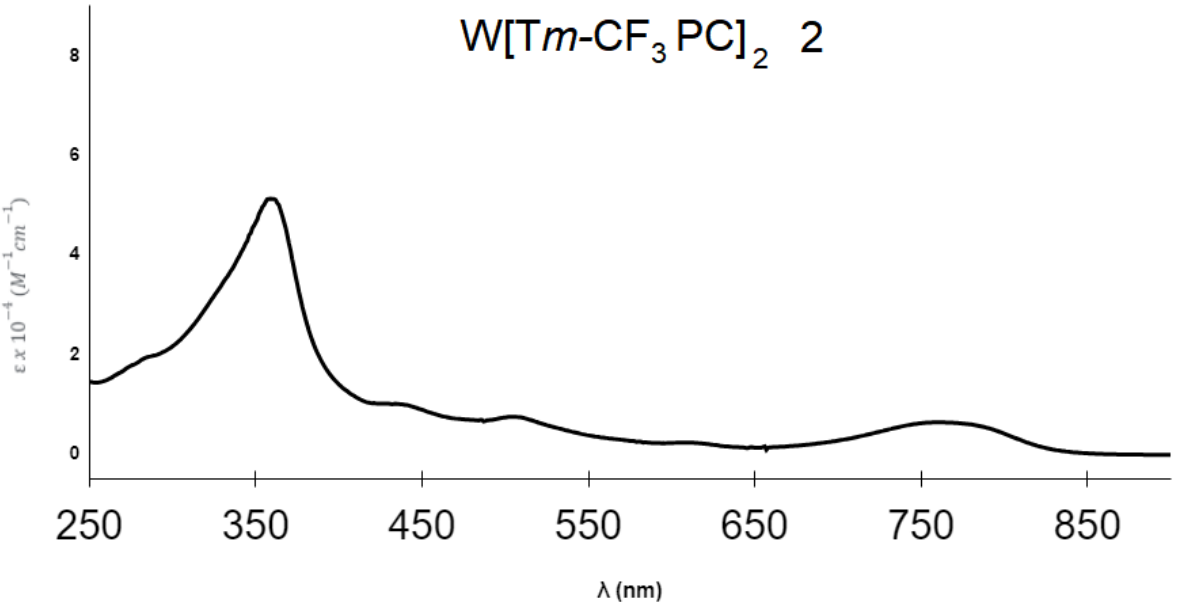

Figure 300. UV-Vis spectrum of W[T*m*-CF_3PC]$_2$ 2 in dichloromethane.

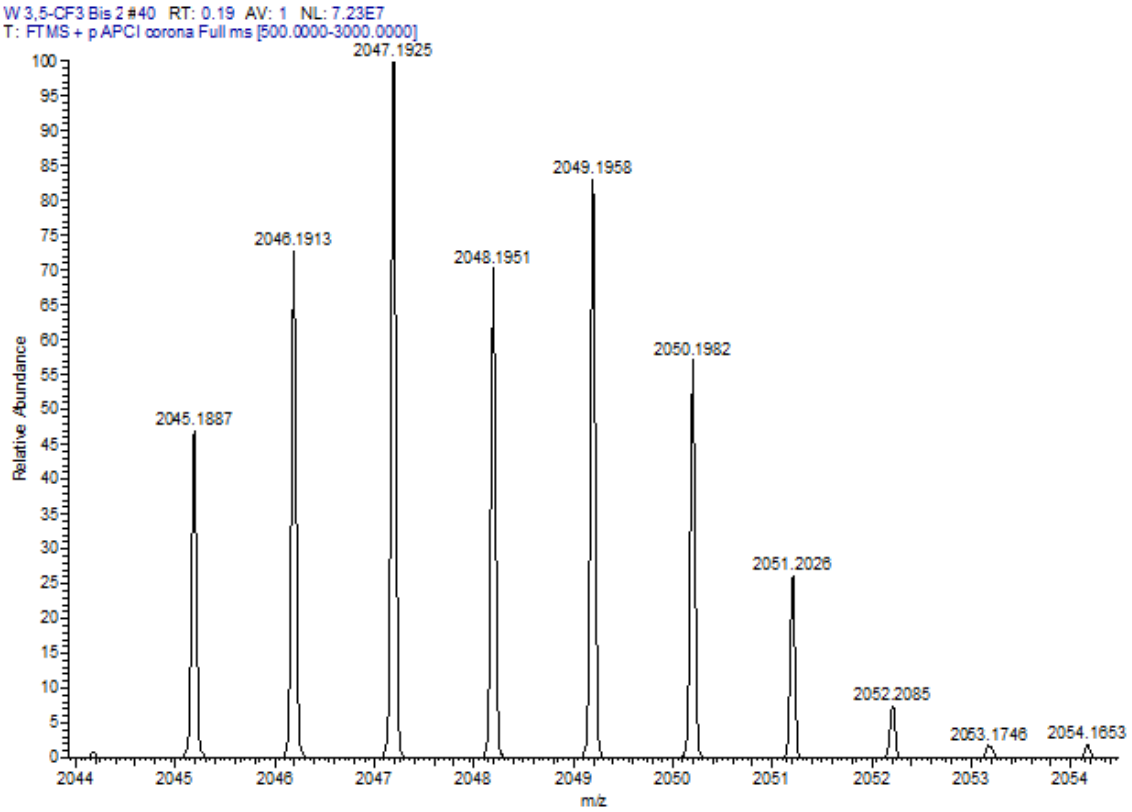

Figure 301. APCI-MS of W[T*m*-CF_3PC]$_2$ 2 with M+1 believed to be caused by hydrogen adduction.

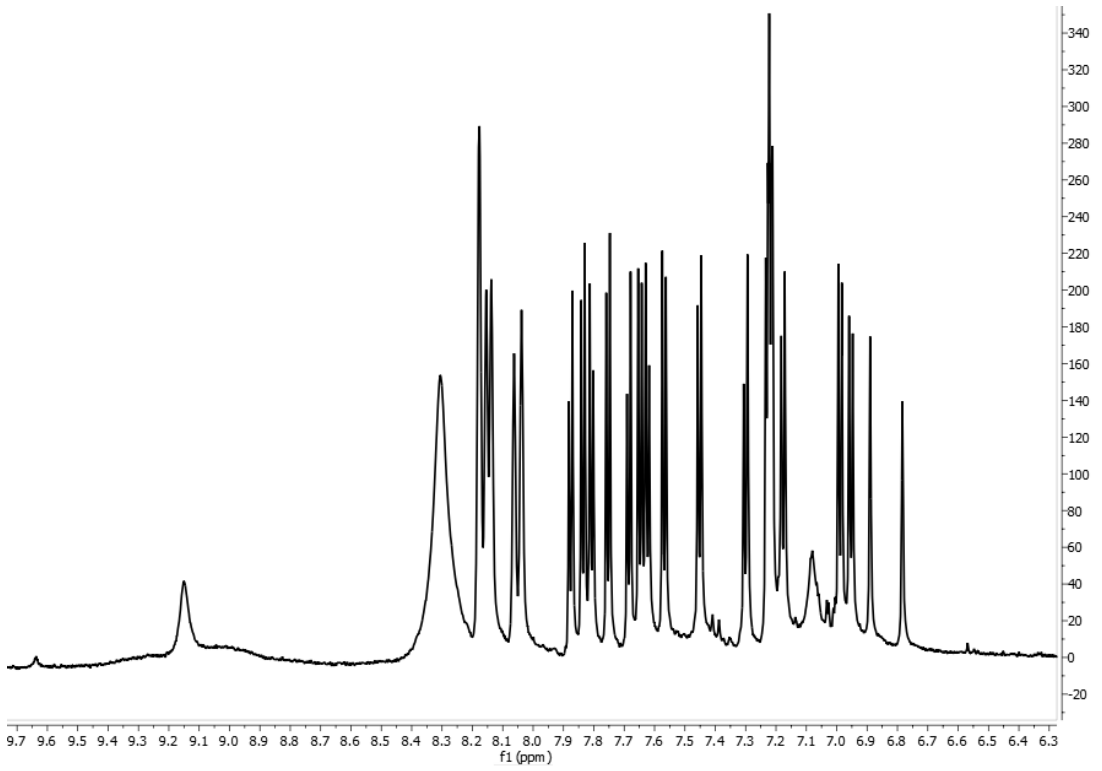

Figure 302. ^{1}H NMR spectrum of W[T*m*-CF_3PC]$_2$ 2 in dichloromethane at room temperature.

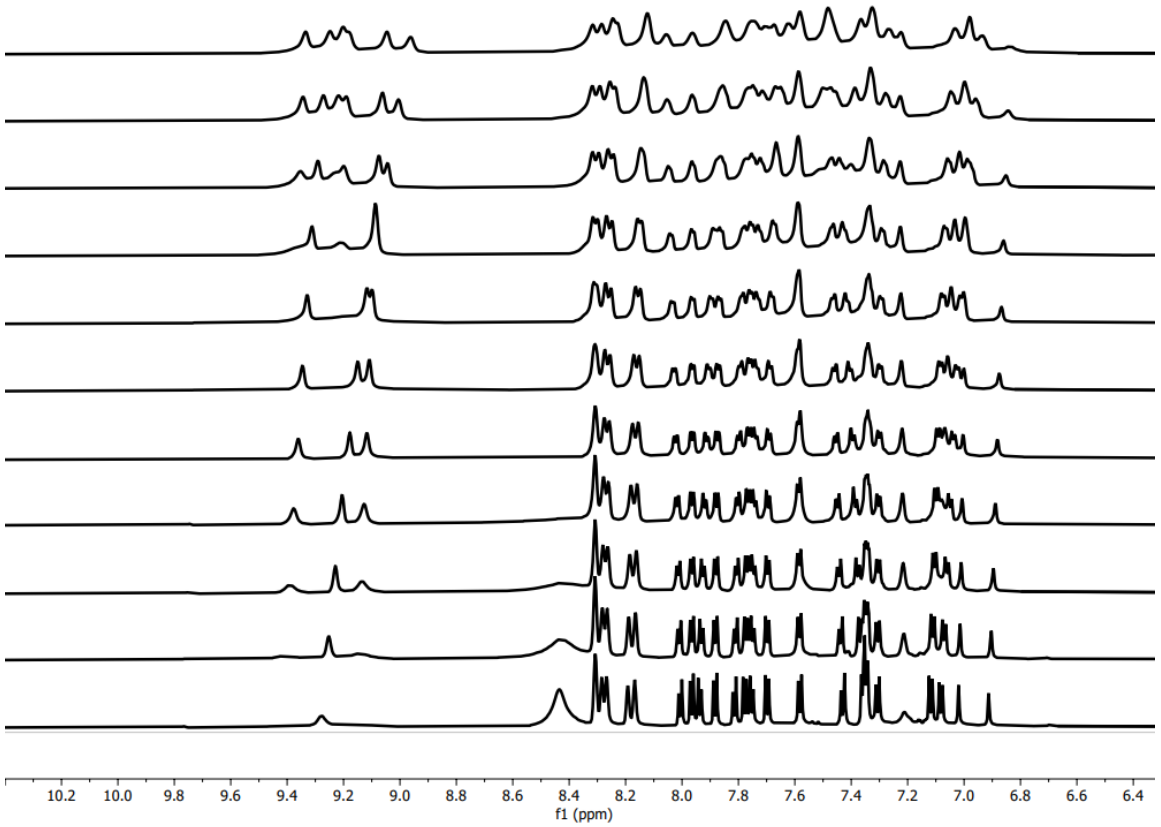

Figure 303. Variable temperature ^{1}H NMR of W[T*m*-CF_3PC]$_2$ 2 in CH_2Cl_2, 193 K (top) to 293 K (bottom) in increment of 10 K.

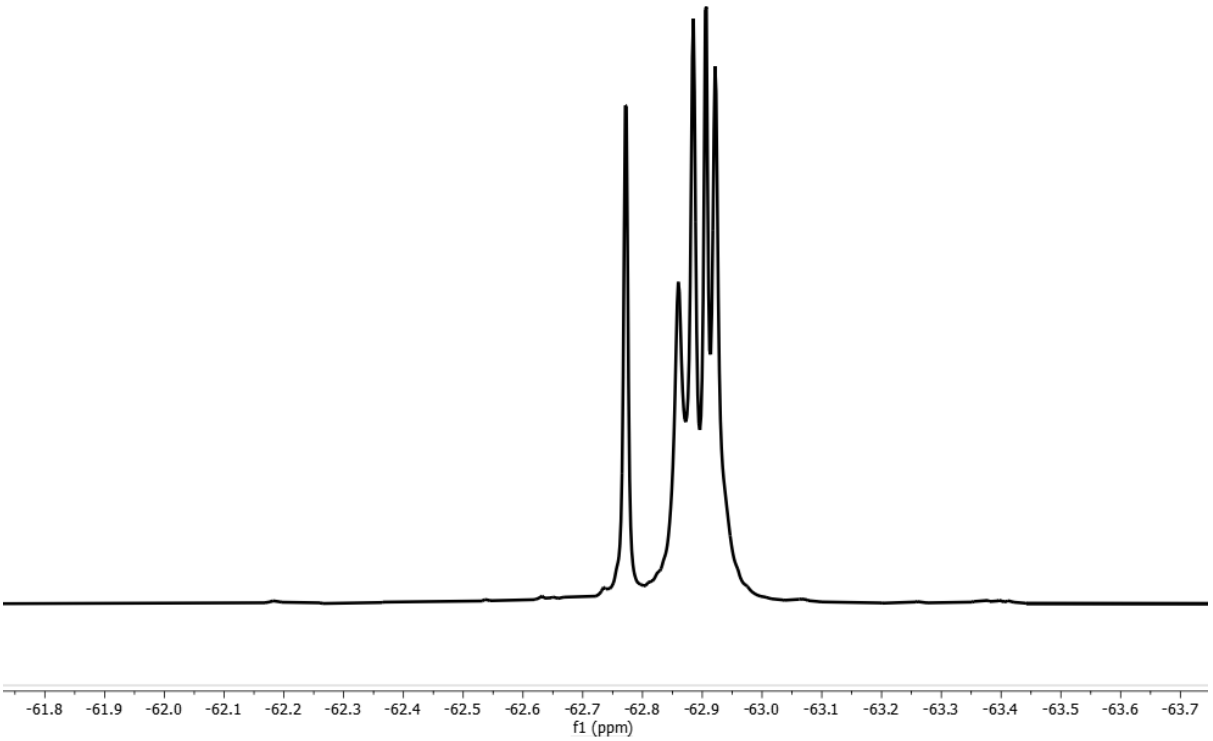

Figure 304. ^{19}F NMR spectrum of W[T*m*-CF_3PC]$_2$ 2 in dichloromethane at room temperature.

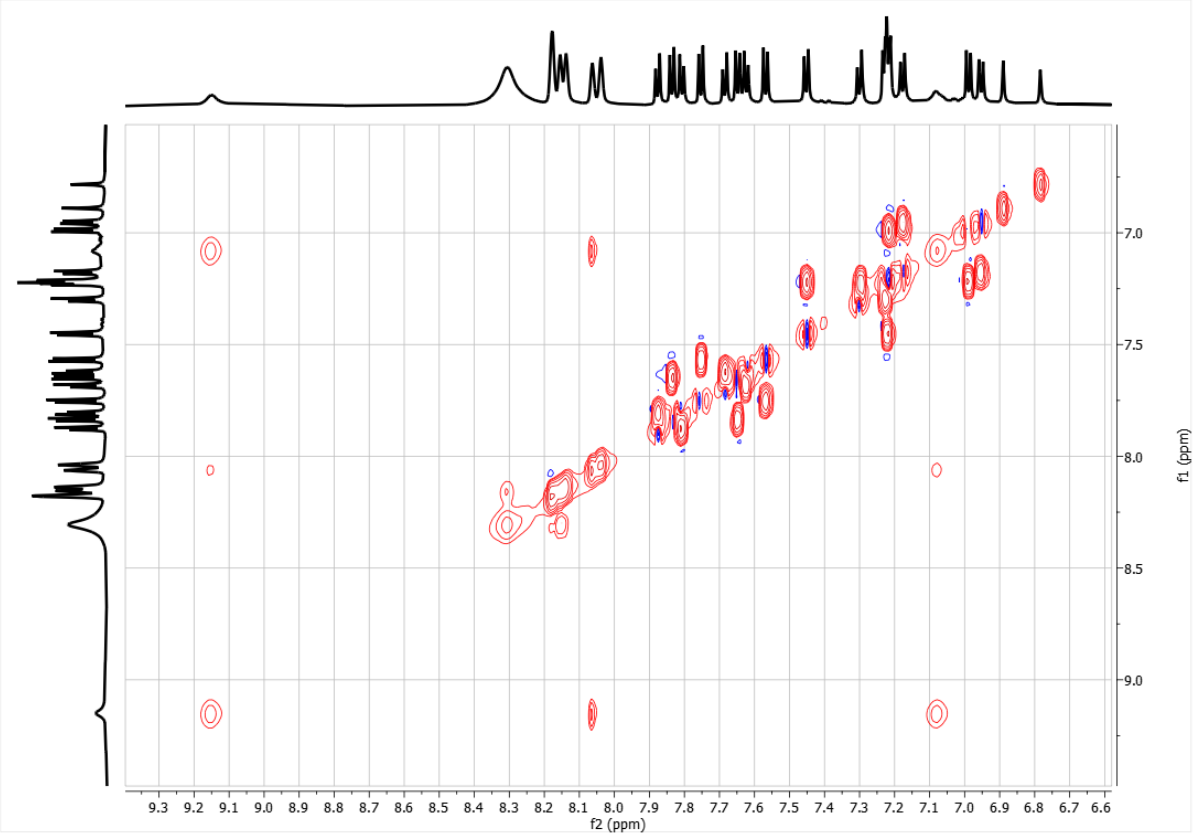

Figure 305. ^{1}H TOCSY NMR of W[T*m*-CF_3PC]$_2$ 1 in dichloromethane.

400 - W[T*m*-OMePC]$_2$

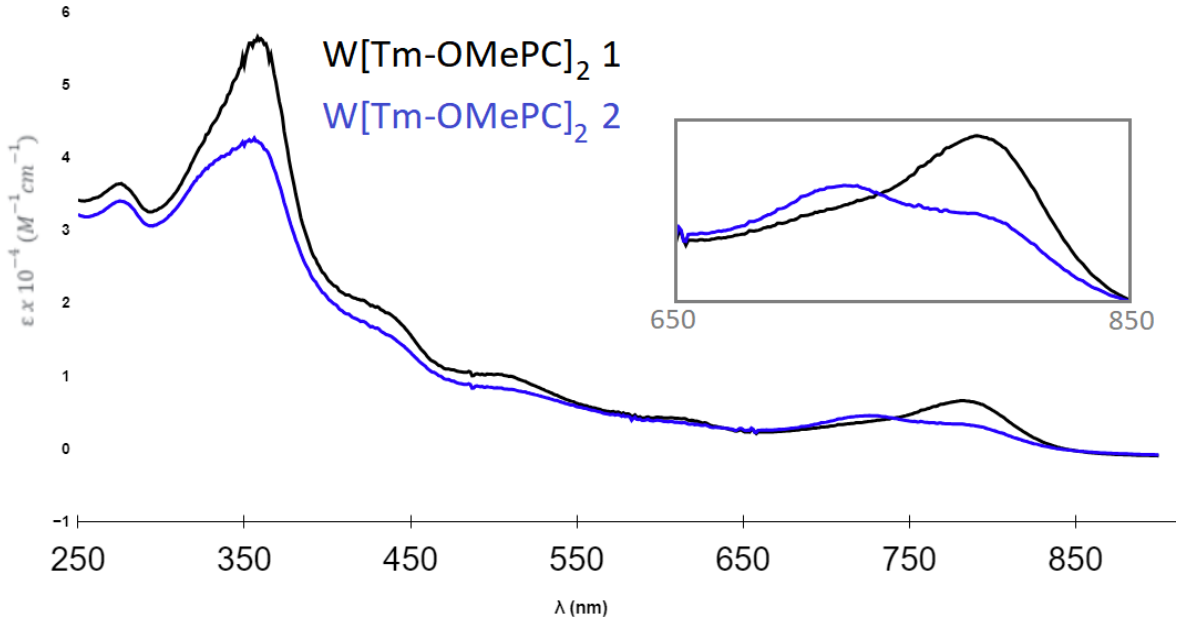

Figure 400. UV-Vis spectrum of W[T*m*-OMePC]$_2$ in dichloromethane.

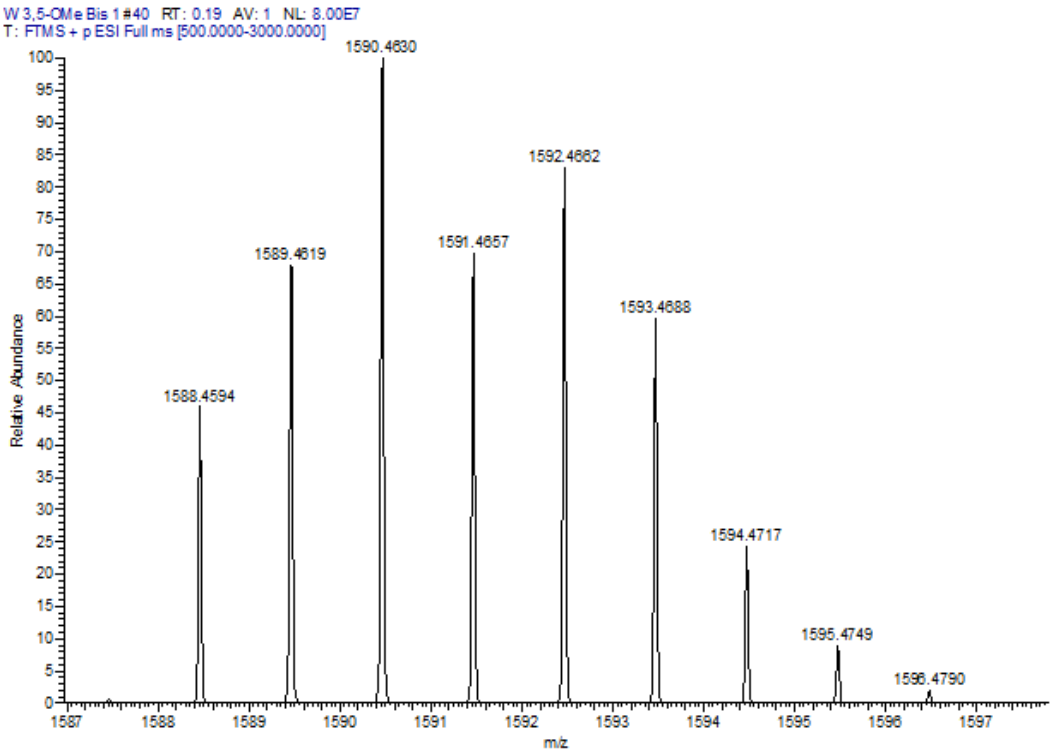

Figure 401. Mass spectrometry of W[T*m*-OMePC]$_2$ 1.

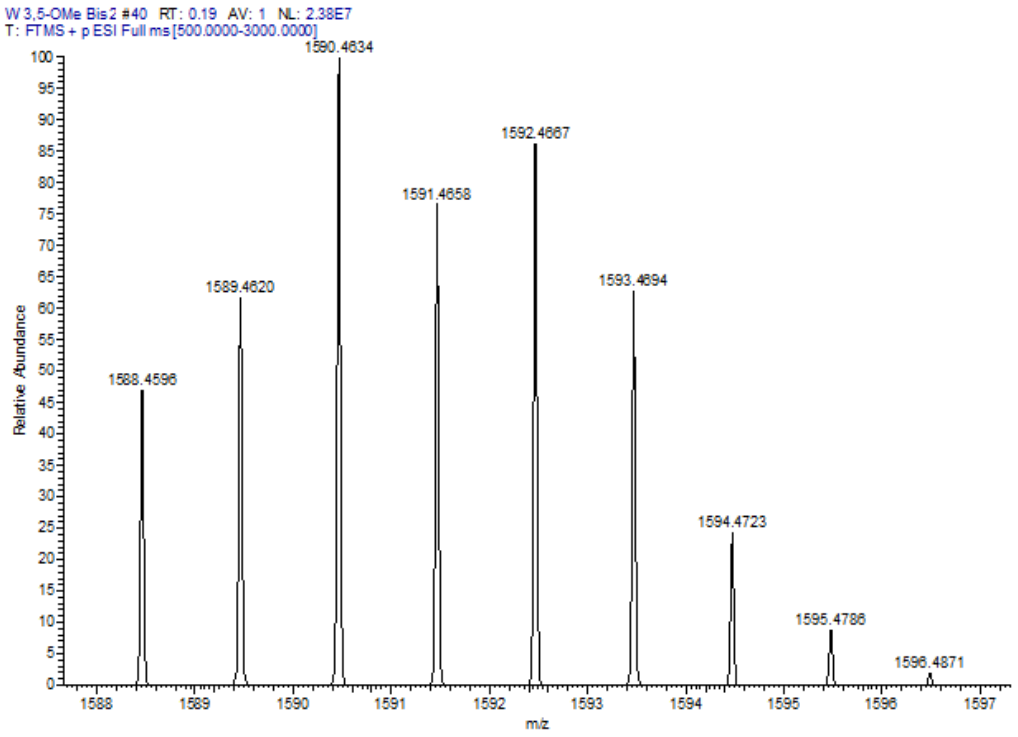

Figure 402. Mass spectrometry of W[T*m*-OMePC]$_2$ 2.

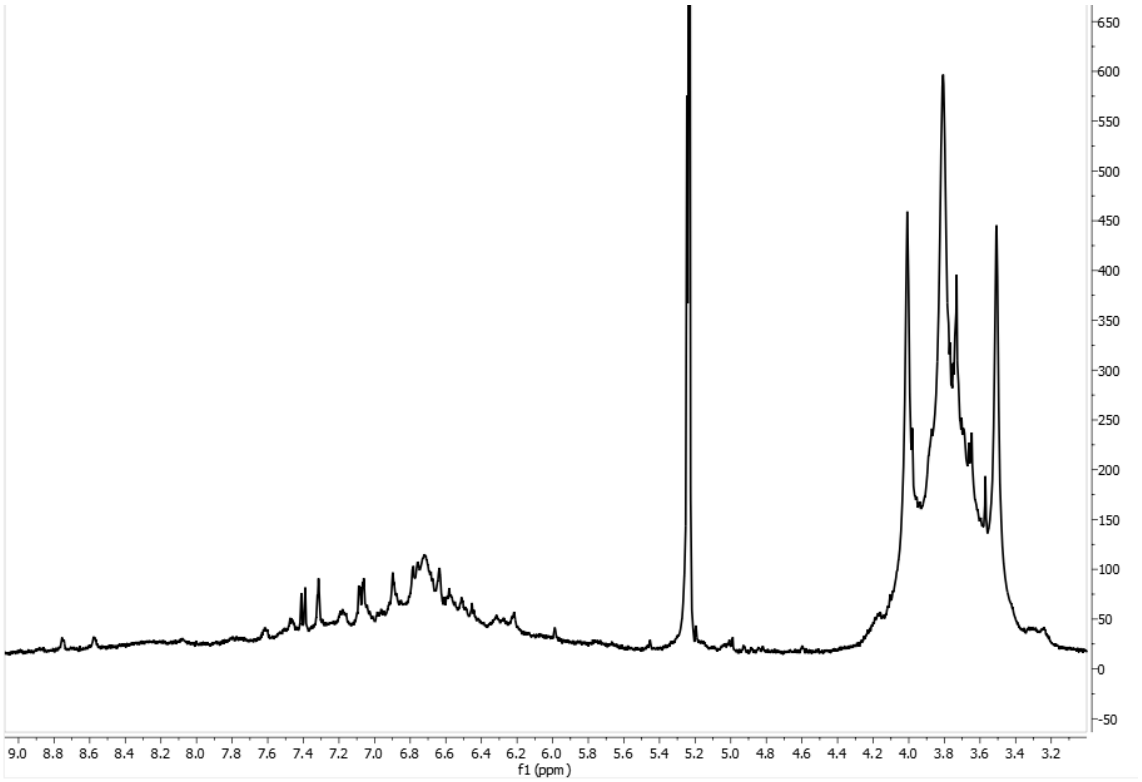

Figure 403. ^{1}H NMR spectrum of W[T*m*-OMePC]$_2$ in dichloromethane at room temperature.

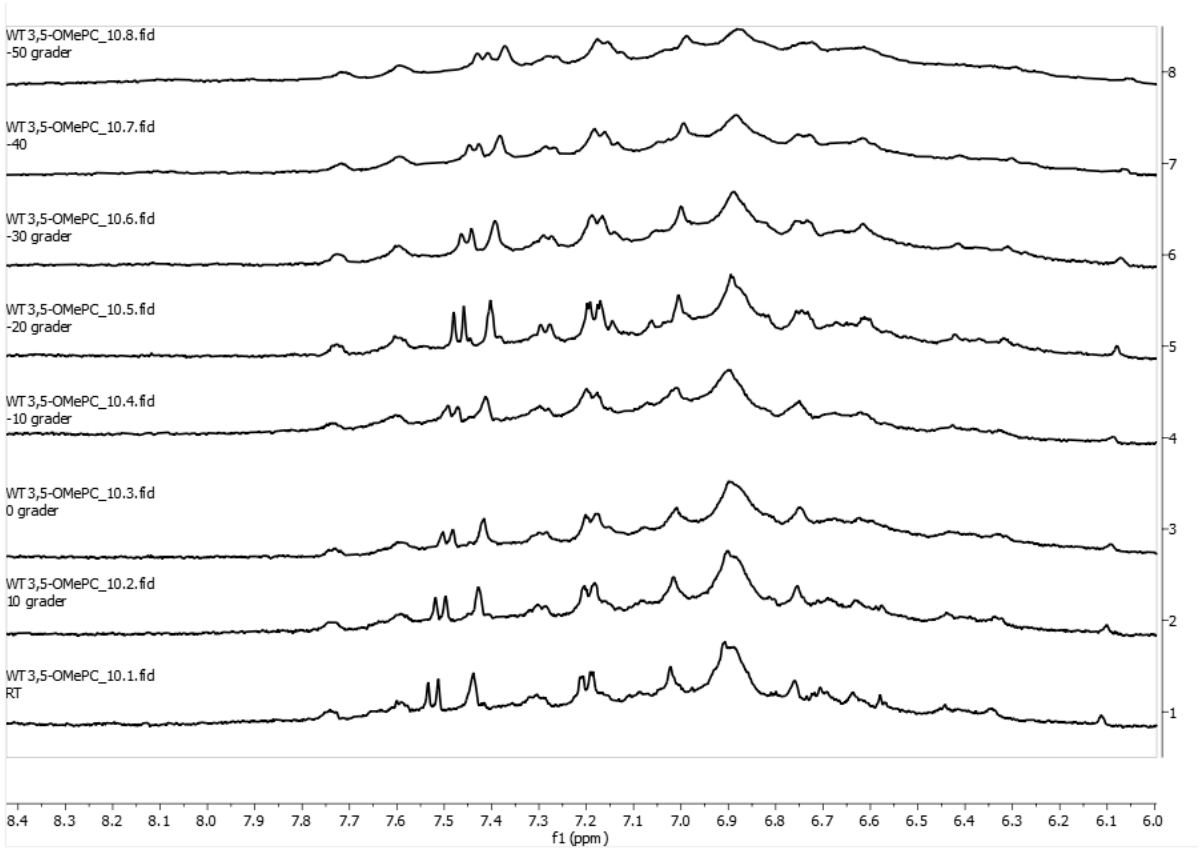

Figure 404. Variable temperature ^{1}H NMR of W[T*m*-CF_3PC]$_2$ 2 in CH_2Cl_2 degree celsius denoted on the left side.

500 - Mo[T*m*-CF_3PC]$_2$ 1

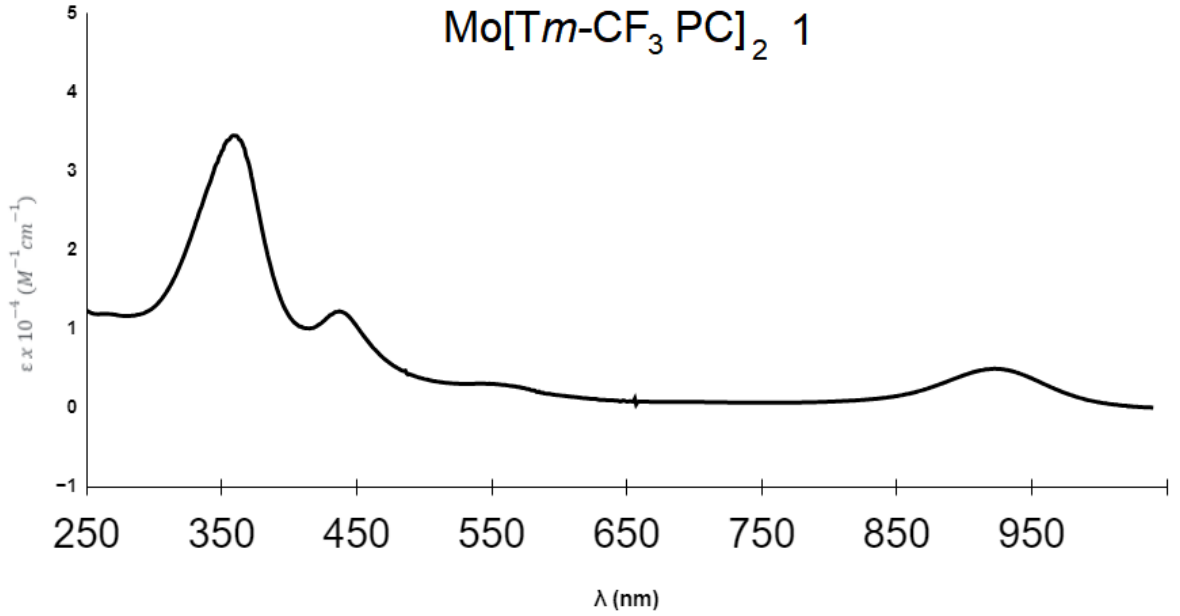

Figure 500. UV-Vis spectrum of Mo[T*m*-CF_3PC]$_2$ 1 in dichloromethane.

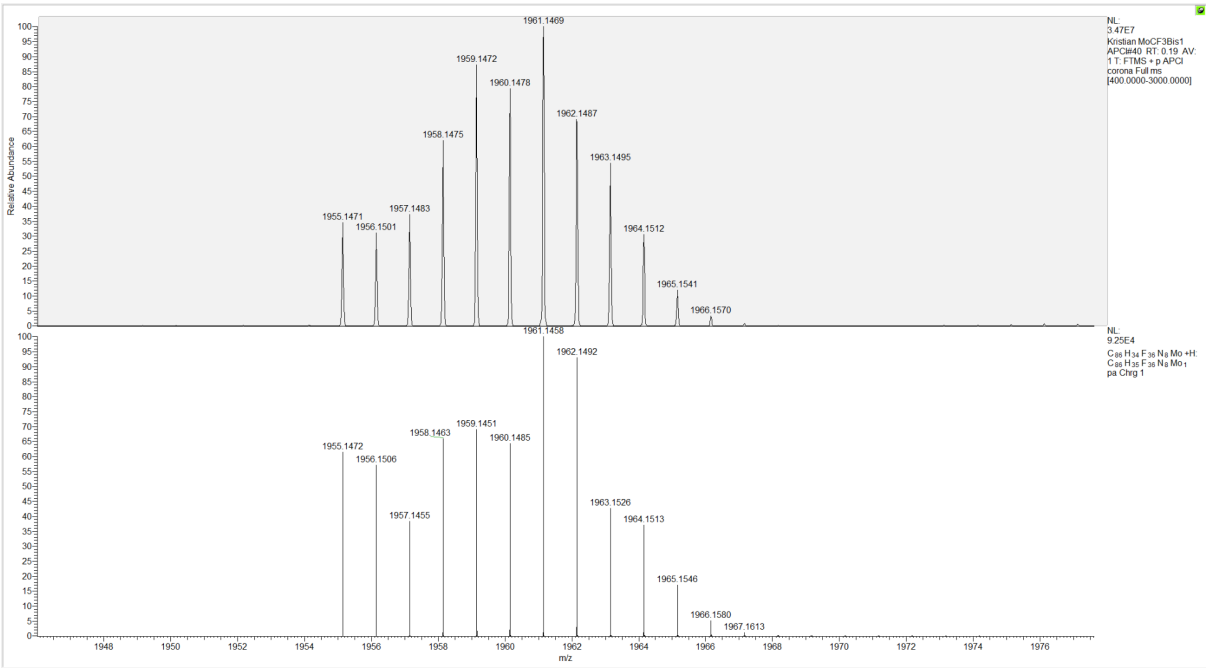

Figure 501. Mass spectrometry of Mo[T*m*-CF_3PC]$_2$ 1 (top) and theoretical mass spectrometry of Mo[T*m*-CF_3PC]$_2$ (bottom).

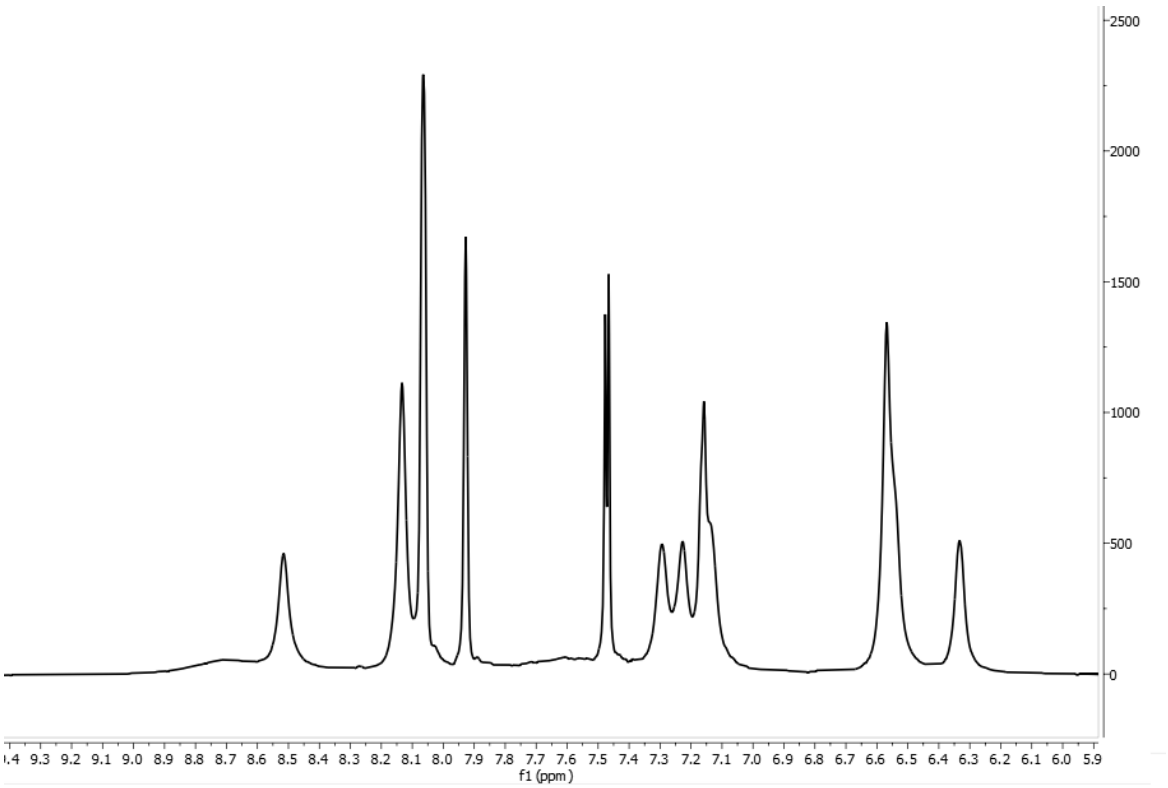

Figure 502. ^{1}H NMR spectrum of Mo[T*m*-CF_3PC]$_2$ 1 in dichloromethane at room temperature.

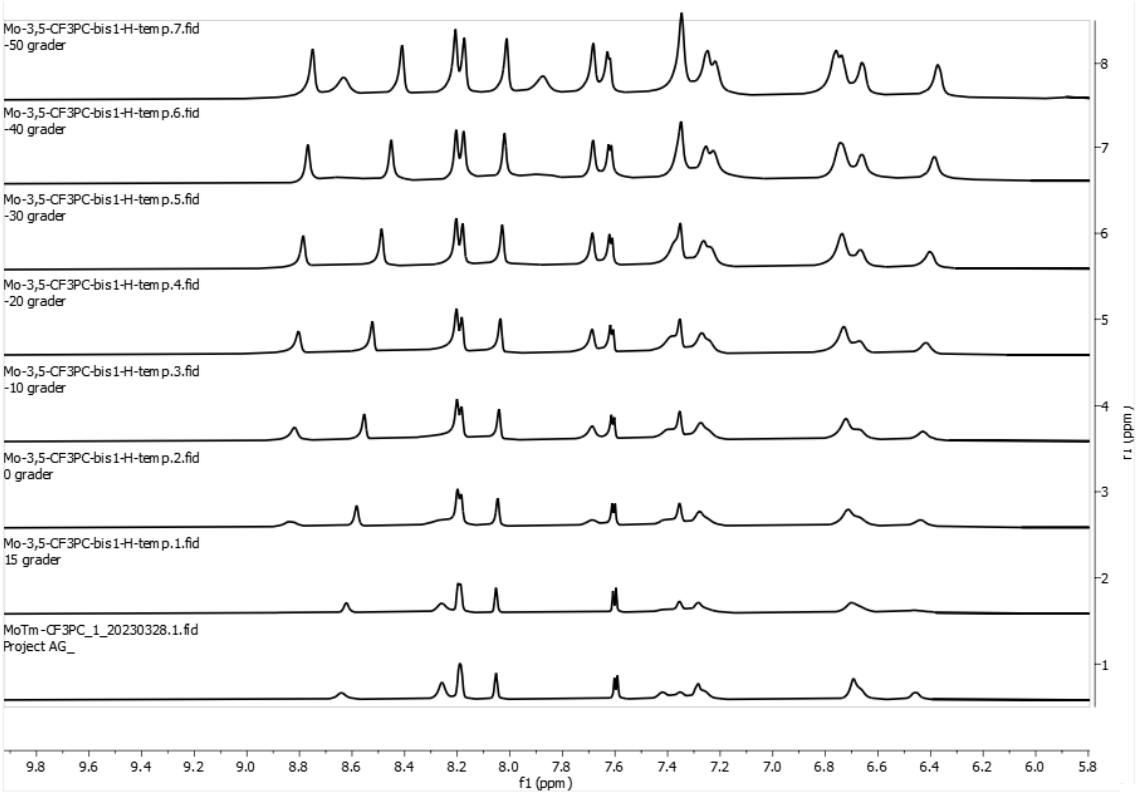

Figure 503. Variable temperature ^{1}H NMR of Mo[T*m*-CF_3PC]$_2$ 1 in dichloromethane, degree celsius denoted on the left side.

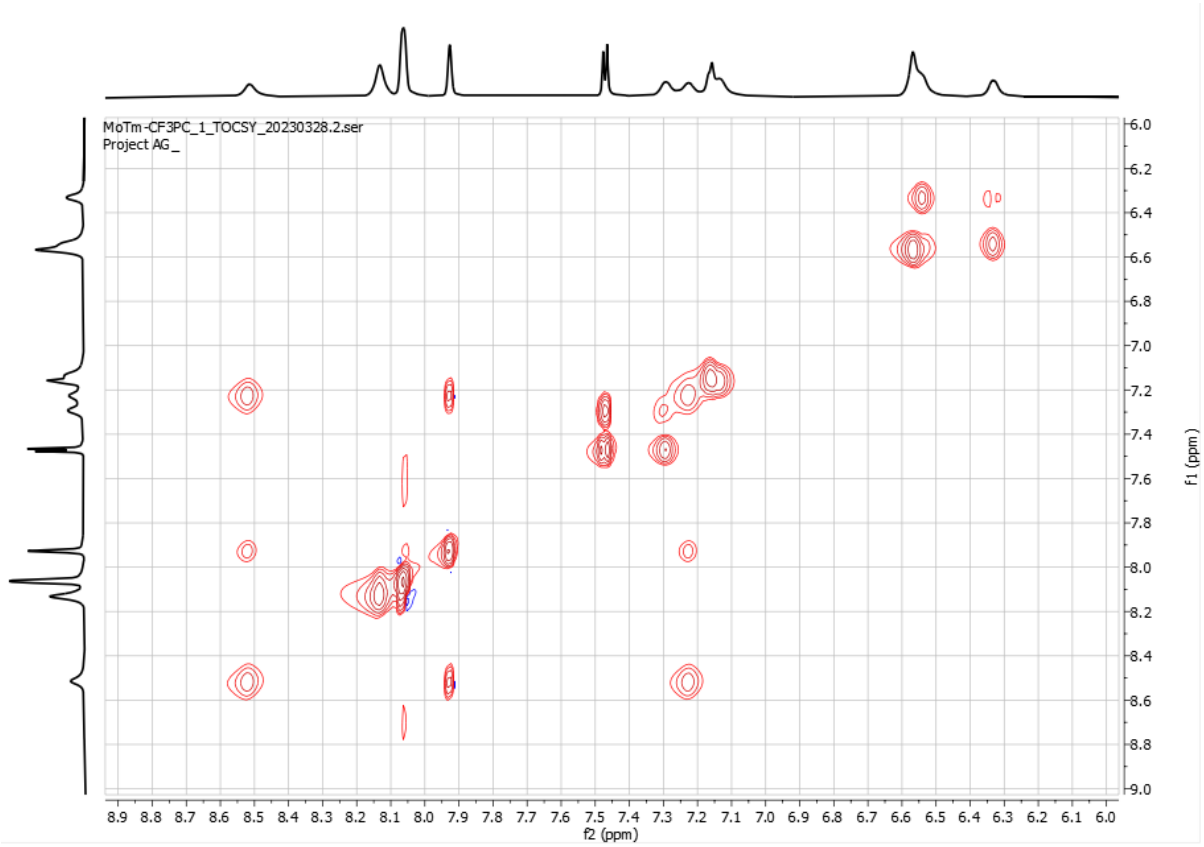

Figure 504. ^{1}H TOCSY NMR of Mo[T*m*-CF_3PC]$_2$ 1 in dichloromethane.

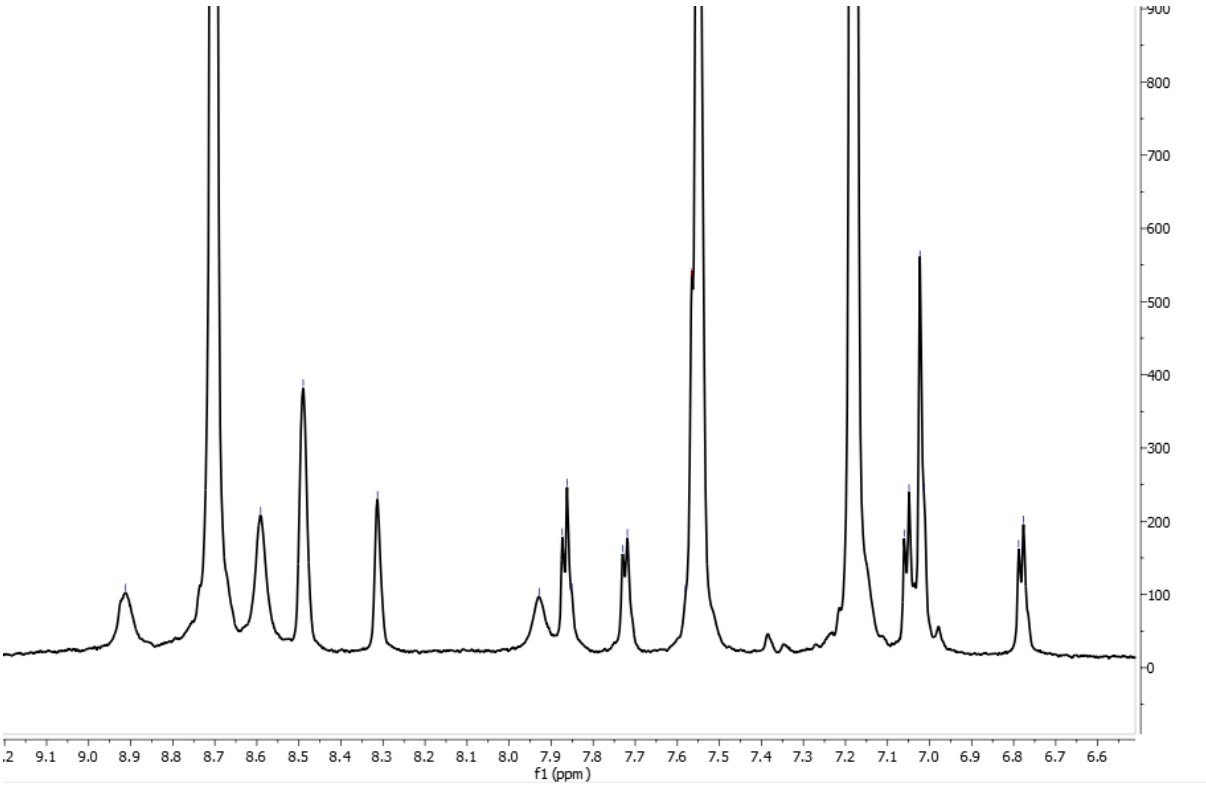

Figure 505. ^{1}H NMR spectrum of Mo[T*m*-CF_3PC]$_2$ 1 in pyridine at room temperature.

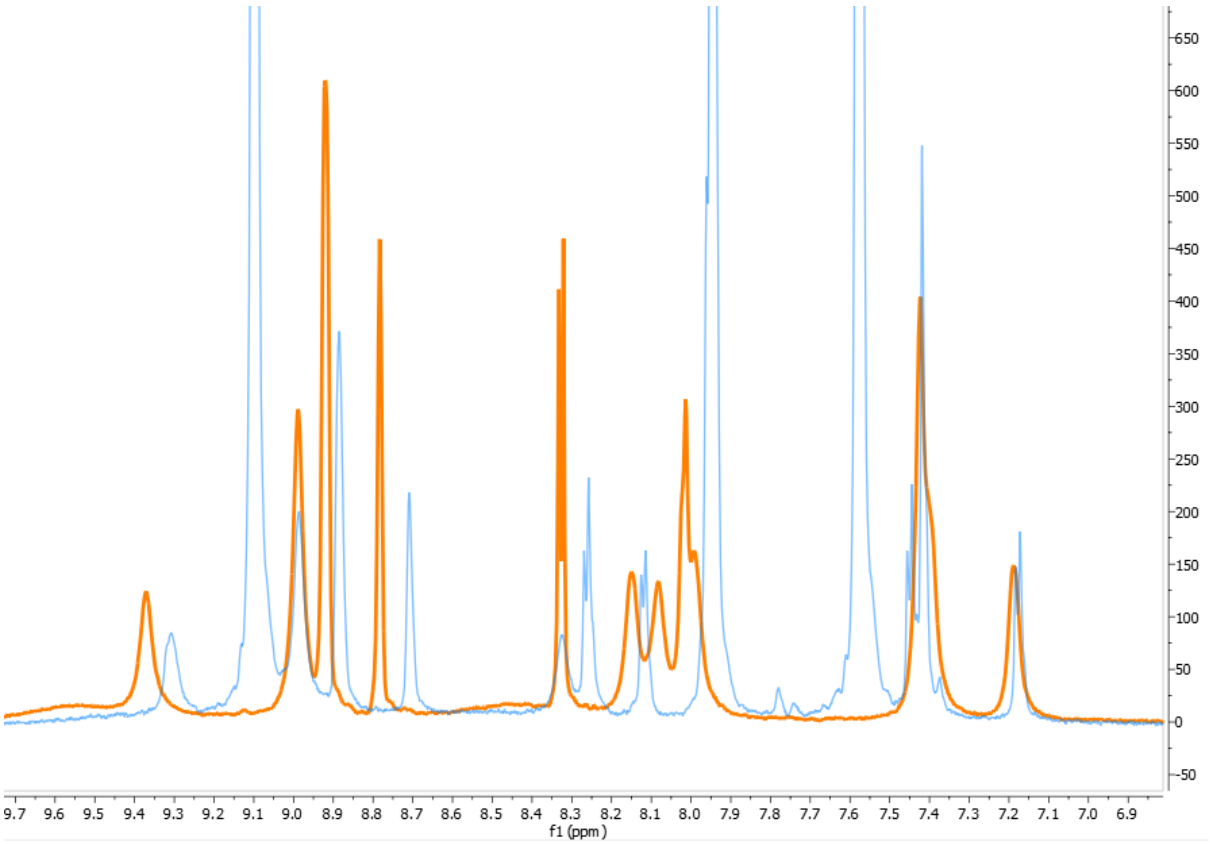

Figure 506. Comparison of ^{1}H NMR spectrum for Mo[T*m*-CF_3PC]$_2$ 1 in pyridine (blue) and dichloromethane (yellow) at room temperature.

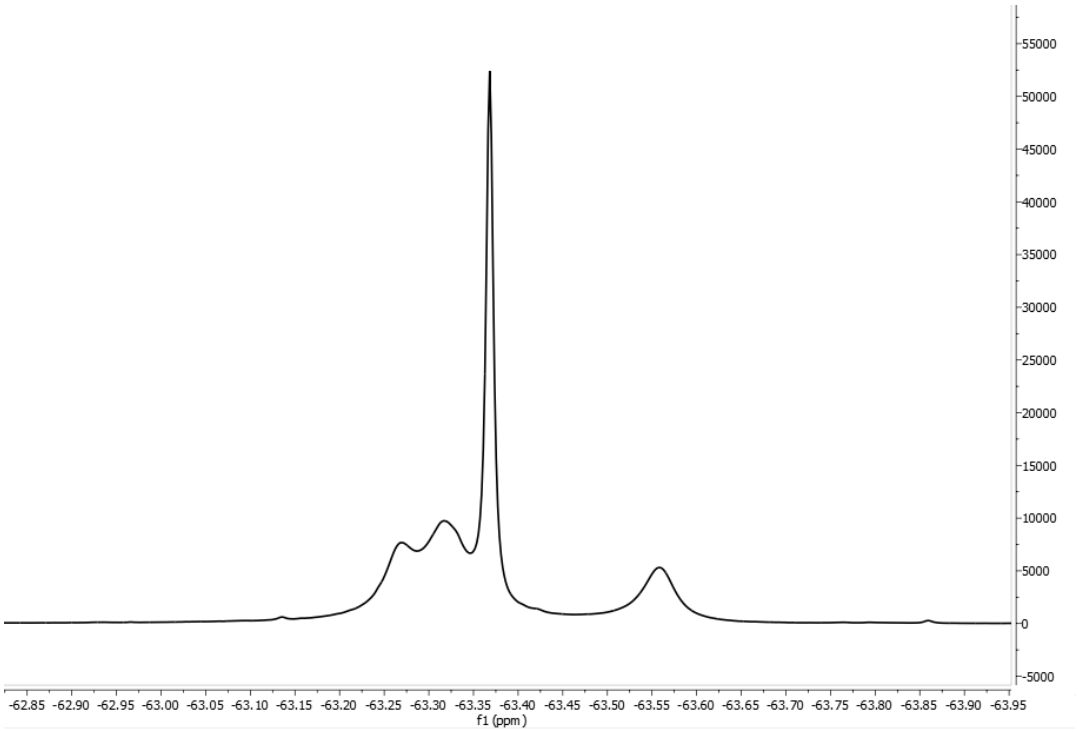

Figure 507. ^{19}F NMR spectrum of Mo[T*m*-CF_3PC]$_2$ 1 in dichloromethane at room temperature.

600 - Mo[T*m*-CF_3PC]$_2$ 2

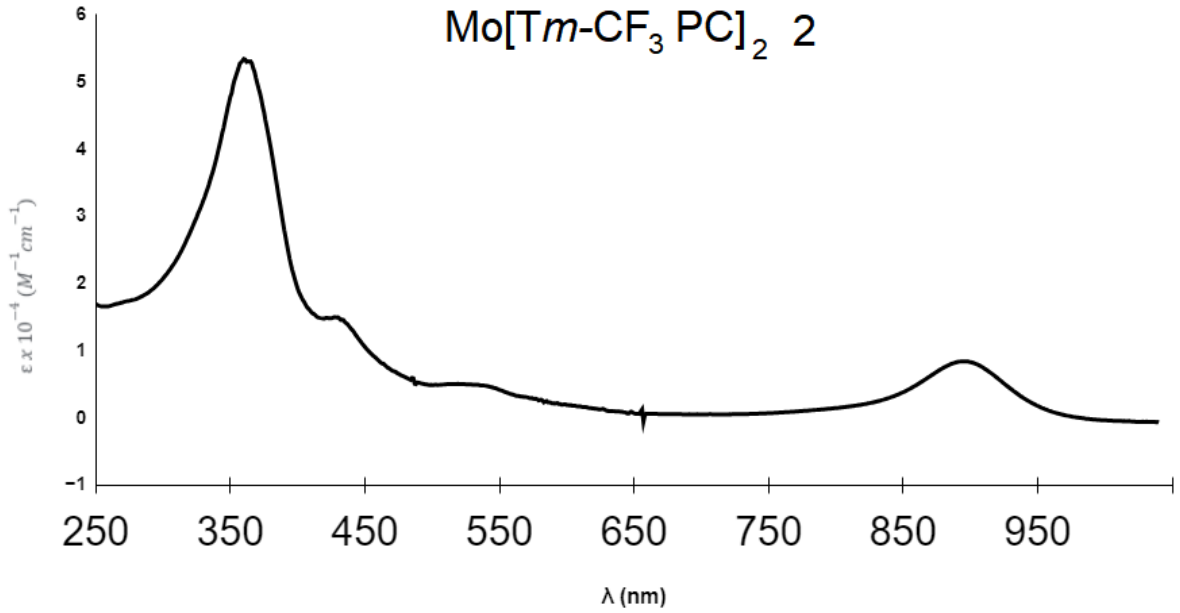

Figure 600. UV-Vis spectrum of Mo[T*m*-CF_3PC]$_2$ 2 in dichloromethane.

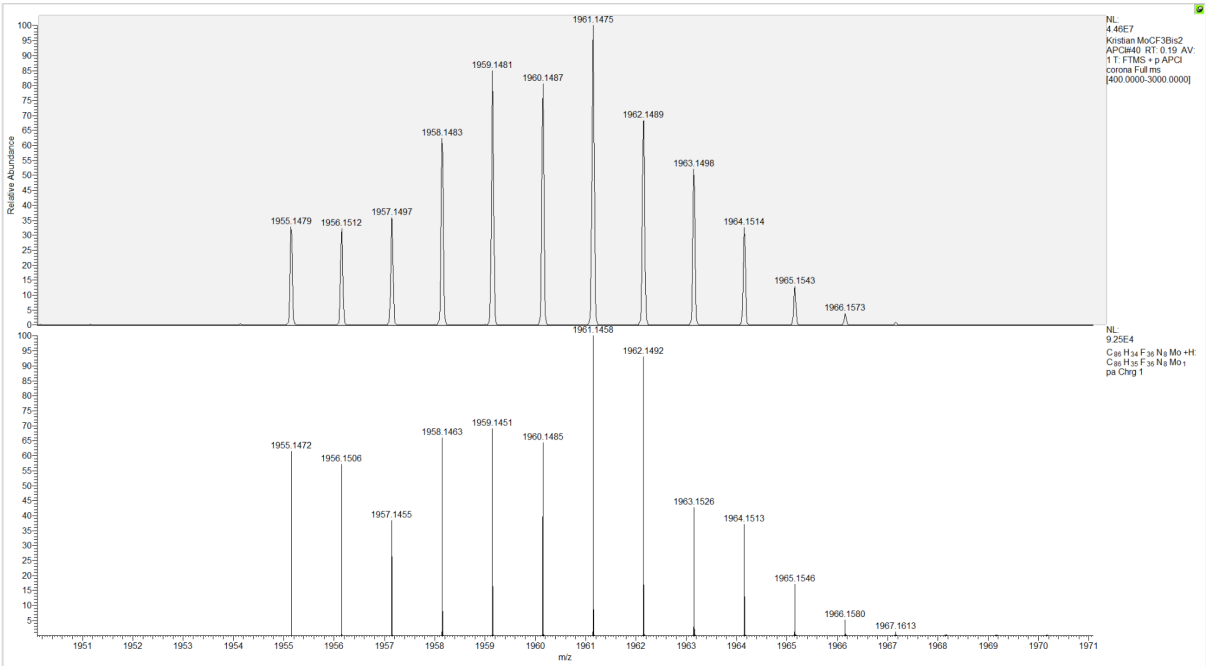

Figure 601. Mass spectrometry of Mo[T*m*-CF_3PC]$_2$ 2 (top) and theoretical mass spectrometry of Mo[T*m*-CF_3PC]$_2$ (bottom).

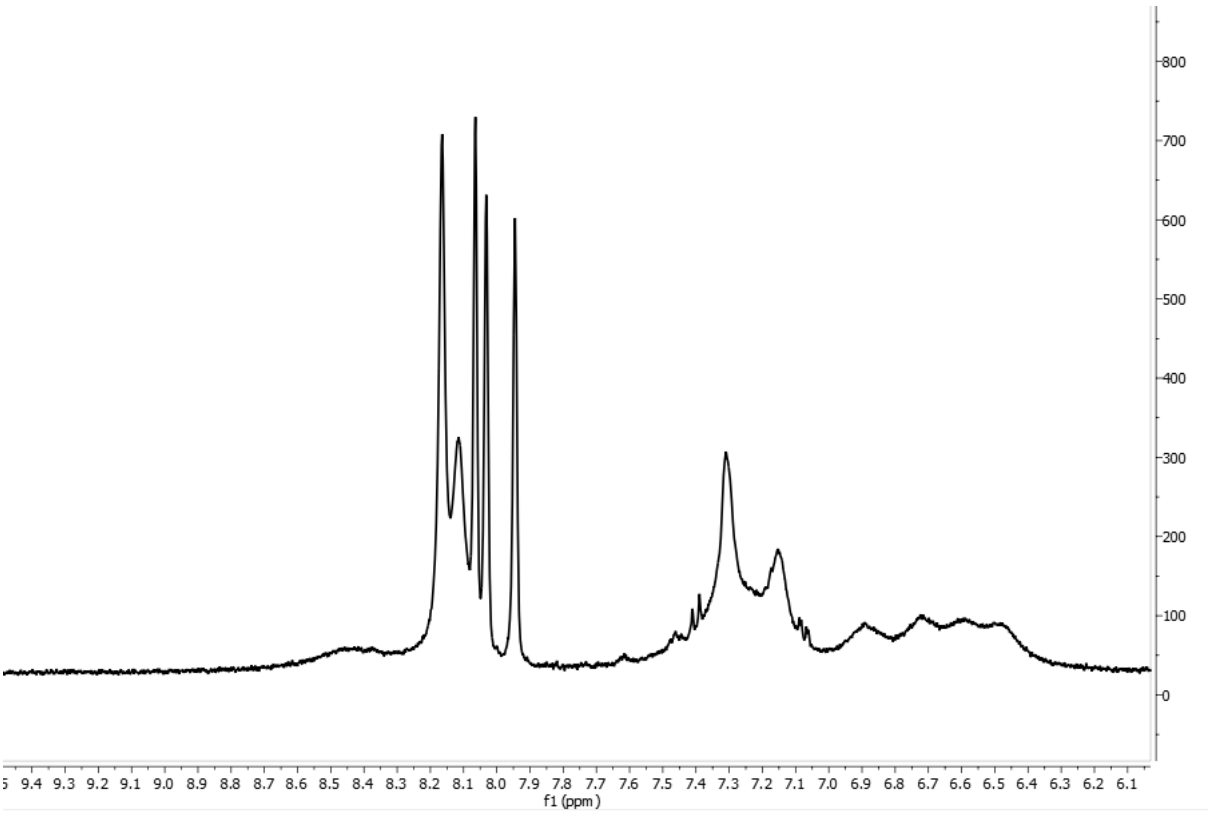

Figure 602. ^{1}H NMR spectrum of Mo[T*m*-CF_3PC]$_2$ 2 in dichloromethane at room temperature.

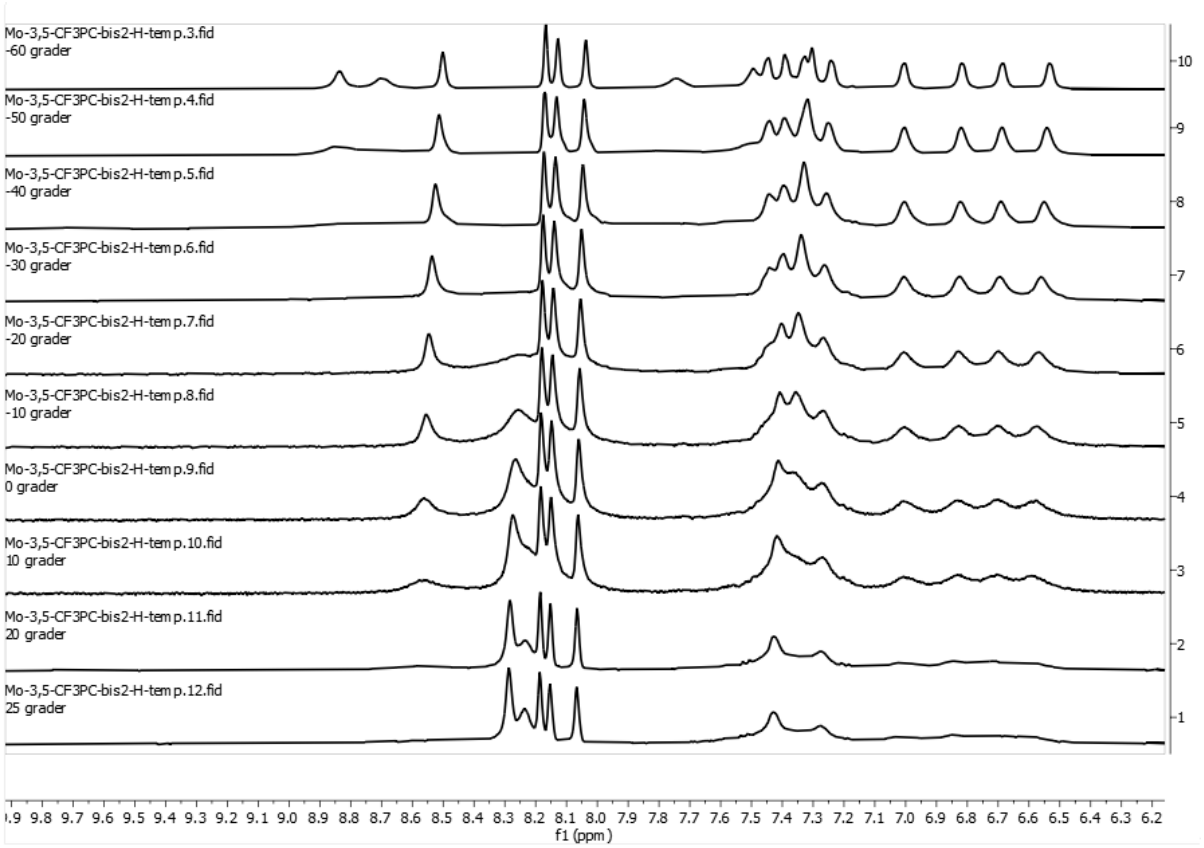

Figure 603. Variable temperature ^{1}H NMR of Mo[T*m*-CF_3PC]$_2$ 2 in dichloromethane, degree celsius denoted on the left side.

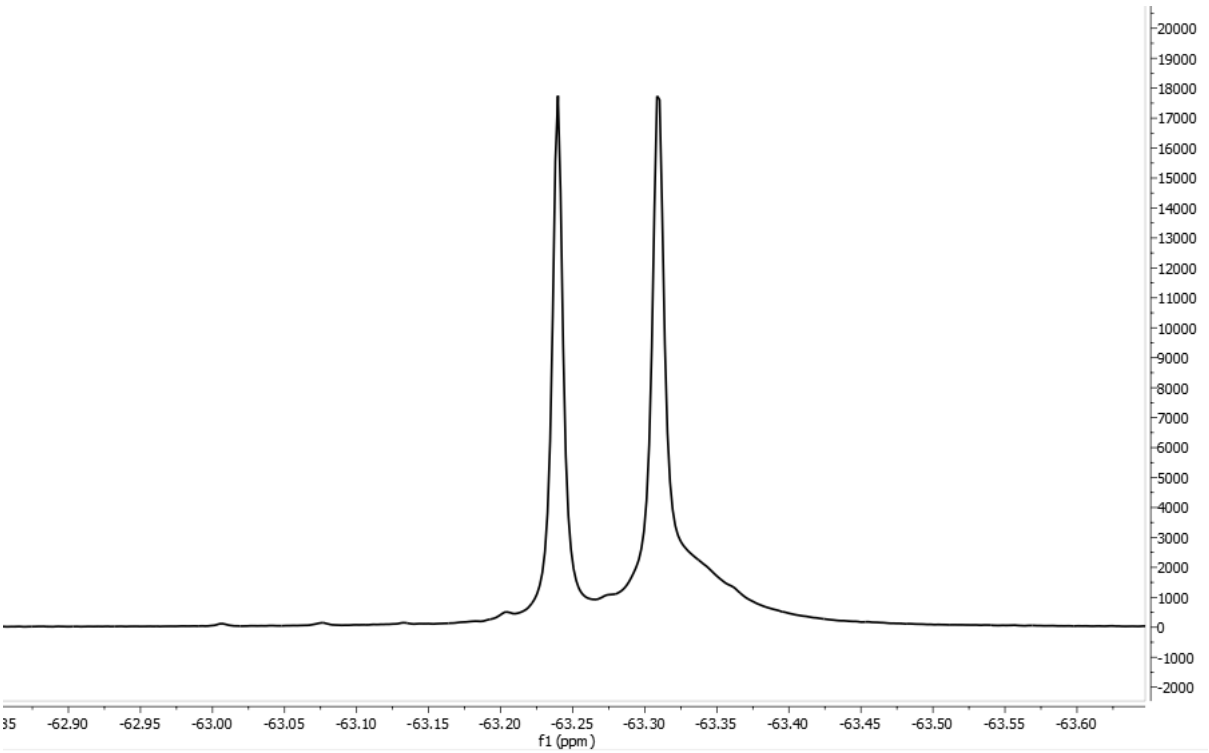

Figure 604. ^{19}F NMR spectrum of Mo[T*m*-CF_3PC]$_2$ 2 in dichloromethane at room temperature.

700 - Mo[T2-TPC]$_2$ - 2-TP = 2-thiophene

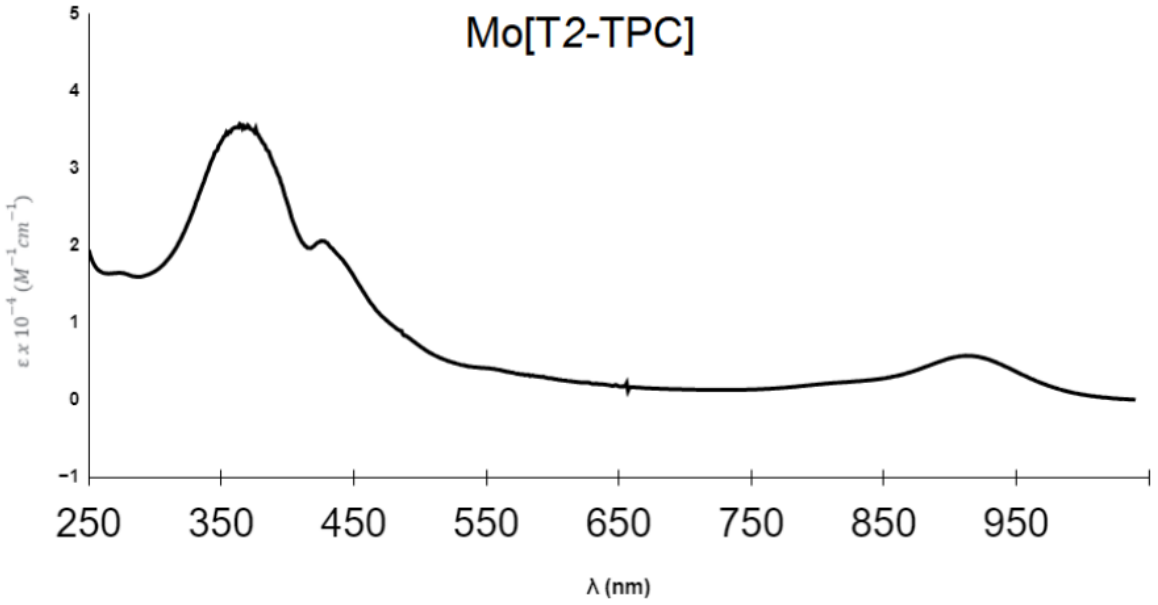

Figure 700. UV-Vis spectrum of Mo[T2-TPC]$_2$ in dichloromethane.

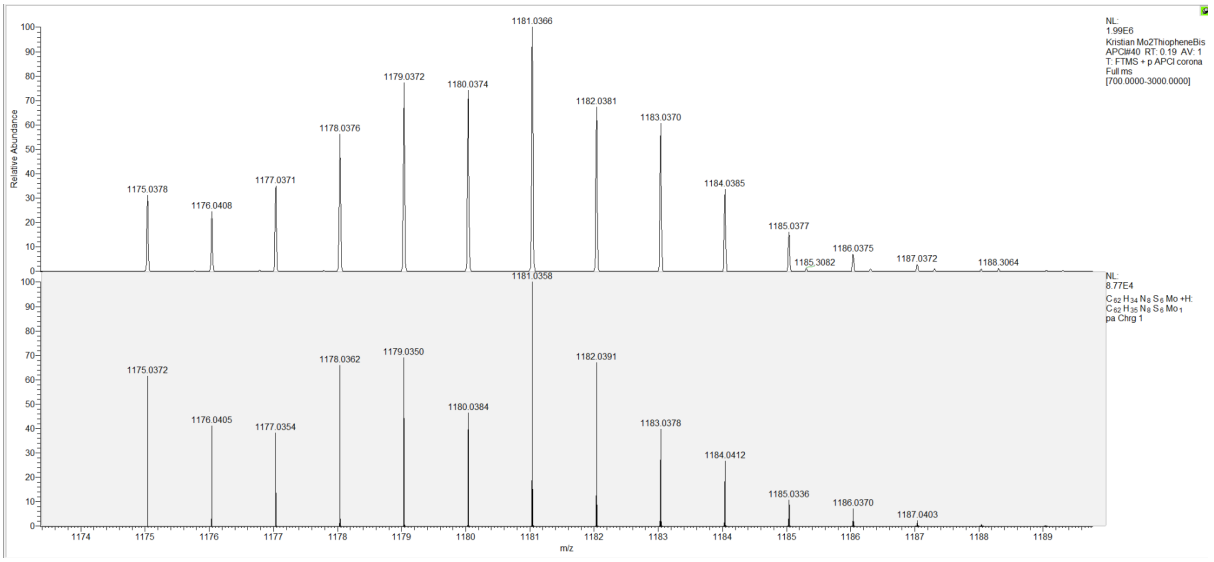

Figure 701. Mass spectrometry of Mo[T2-TPC]$_2$ (top) and theoretical mass spectrometry of Mo[T2-TPC]$_2$ (bottom).

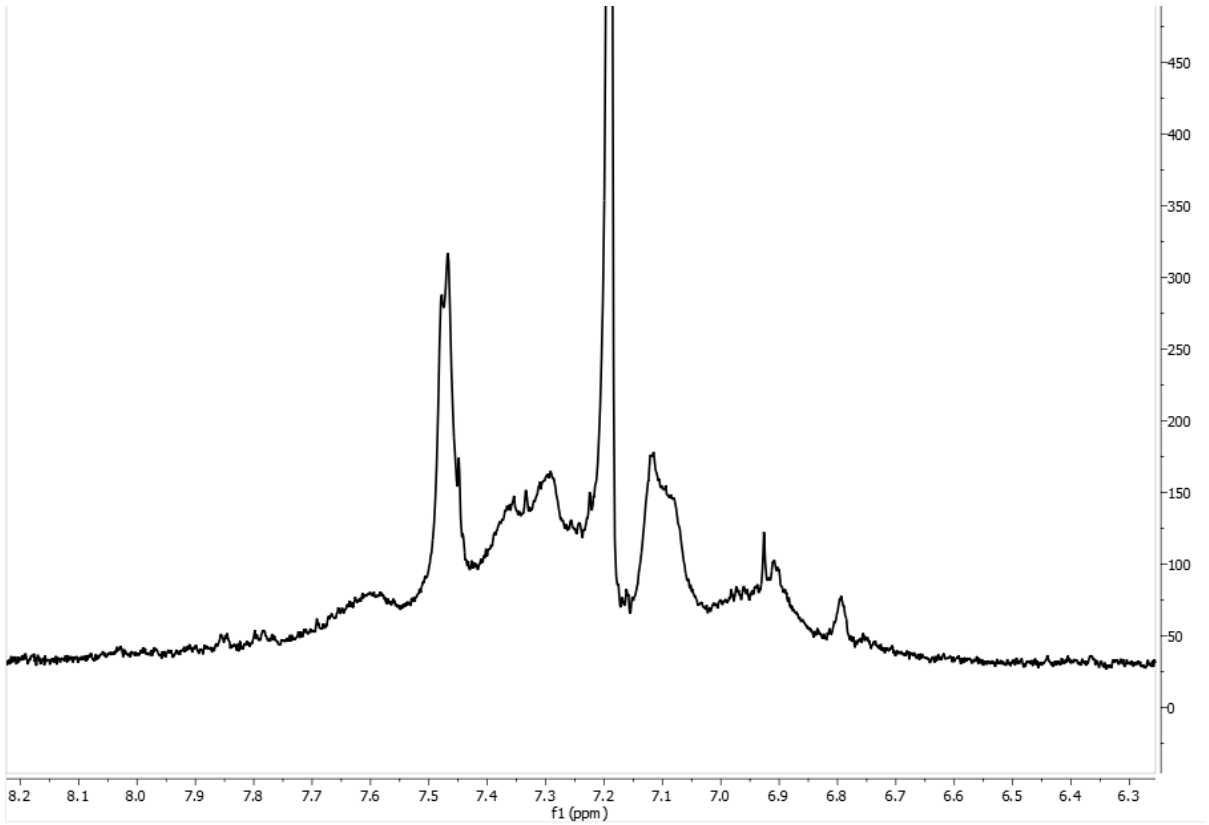

Figure 702. ^{1}H NMR spectrum of Mo[T2-TPC]$_2$ in chloroform at room temperature.

800 - Fast Fourier transform

#In Figure 46, the values for functions f(x) and g(x) were changed to f(x)=cos(20x), g(x)=cos(10) for the slow exchange and f(x)=cos(15x), g(x)=cos(15x) for the rapid exchange. To improve the simulation, the swapping inside the composite_function should actually depend on the exchange rate *k*, and not manipulate the functions f(x) and g(x) - but for illustration purposes this is sufficient.

```
import numpy as np
import matplotlib.pyplot as plt

def f(x):
    return np.cos(20 * x)

def g(x):
    return np.cos(10 * x)

def composite_function(x):
    if 0 <= x < np.pi:
        return f(x) * np.exp(-0.2 * x)  # Exponential damping for f(x)
    elif np.pi <= x < 2 * np.pi:
        return g(x) * np.exp(-0.2 * x)  # Exponential damping for g(x)
    elif 2 * np.pi <= x < 3 * np.pi:
        return f(x) * np.exp(-0.2 * x)  # Exponential damping for f(x)
    elif 3 * np.pi <= x < 4 * np.pi:
        return g(x) * np.exp(-0.2 * x)  # Exponential damping for g(x)

# Create x values from 0 to 4*pi
x_values = np.linspace(0, 4 * np.pi, 1000)

# Calculate y values for the exponentially dampened composite function
y_values = [composite_function(x) for x in x_values]
y_values = y_values[:-1]

# Plotting the exponentially dampened composite function
plt.figure(figsize=(8, 6))
plt.subplot(2, 1, 1)
plt.plot(x_values[:-1], y_values, label='Exponentially Dampened Composite Function', color='0')
plt.title('Exponentially Dampened Composite Function of cos(20x) and cos(10x)')
plt.xlabel('Time')
plt.ylabel('Amplitude')
plt.legend()
plt.grid(True)

# Performing FFT
N = len(y_values)
dt = x_values[1] - x_values[0]
fft_result = np.fft.fft(y_values)
frequencies = np.fft.fftfreq(N, dt)

# Plotting the FFT result with positive frequencies up to 10
plt.subplot(2, 1, 2)
positive_freq_mask = (frequencies >= 0) & (frequencies <= 6)
plt.plot(frequencies[positive_freq_mask], np.abs(fft_result[positive_freq_mask]), color='0')
plt.title('FFT of Exponentially Dampened Composite Function')
plt.xlabel('Frequency')
plt.ylabel('Amplitude')
plt.grid(True)

plt.tight_layout()
plt.show()
```

900 - DFT Optimized Coordinates

Results from section 7.3.1

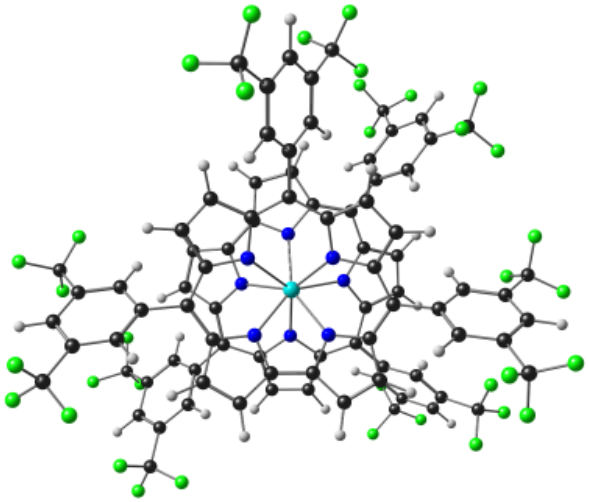	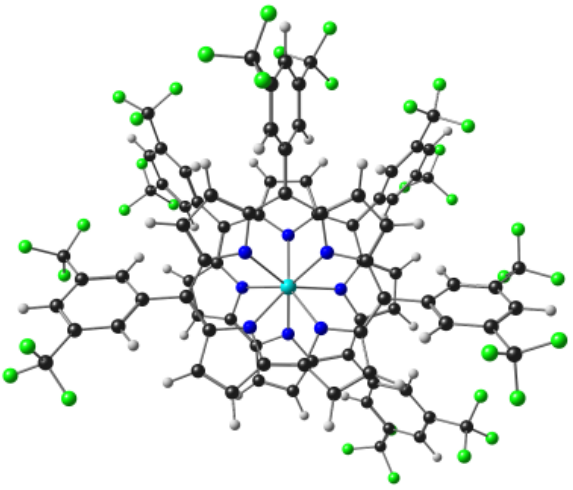
W[T*m*-CF_3PC]$_2$ 1 (135°) ΔE = 0.01 eV	W[T*m*-CF_3PC]$_2$ 2 (45°) ΔE = 0.00 eV

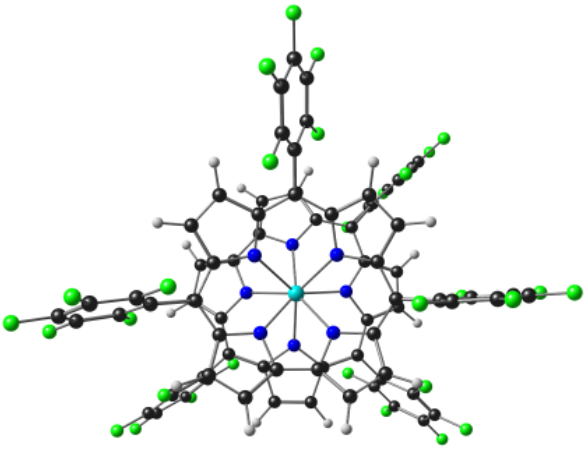	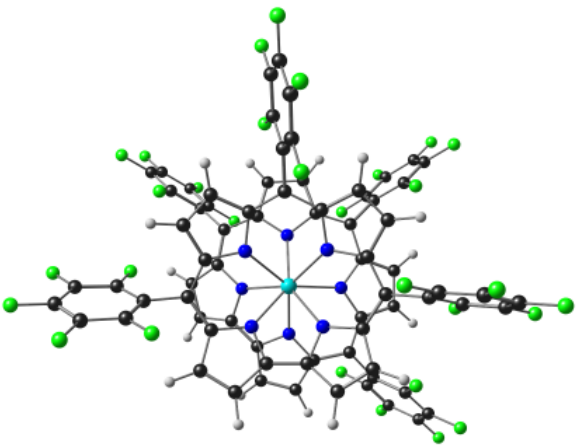
W[TPFPC]$_2$ (135°) ΔE = 0.01 eV	W[TPFPC]$_2$ (45°) ΔE = 0.00 eV

W[T*m*-CF_3PC]$_2$ 1 (135 °)

74	0.000000000	0.000000000	0.470811000
7	0.498722000	1.313527000	2.124955000
7	0.834771000	-1.054017000	-1.298082000
7	-1.905471000	0.830470000	1.279422000
7	-1.483602000	-1.436527000	-0.140987000
7	-0.498722000	-1.313527000	2.124955000
7	-0.834771000	1.054017000	-1.298082000
7	1.905471000	-0.830470000	1.279422000
7	1.483602000	1.436527000	-0.140987000
6	2.031234000	2.486618000	3.360453000
6	2.178084000	-1.162009000	-1.642612000
6	-1.724017000	-1.935815000	2.095324000
6	-3.264971000	0.955614000	-0.787905000
6	2.302929000	-1.627129000	-2.986556000
6	0.959989000	2.195419000	4.181484000
6	-0.015802000	1.504013000	3.396930000
6	-2.284695000	-1.991996000	0.825053000
6	-3.120241000	0.835520000	0.595339000
6	0.122788000	-1.470900000	-2.428277000
6	1.036510000	-1.809700000	-3.471352000
6	-2.233578000	0.931986000	2.634178000
6	-1.347465000	1.201993000	3.691122000
6	-2.018204000	-1.803701000	-1.361401000
6	-3.401428000	-2.633054000	0.233764000
6	-4.201762000	0.843418000	1.530694000
6	-1.253850000	-1.735686000	-2.519444000
6	-3.656144000	0.917807000	2.781356000
6	-3.250868000	-2.496467000	-1.130965000
6	-2.031234000	-2.486618000	3.360453000
6	-2.178084000	1.162009000	-1.642612000
6	1.724017000	1.935815000	2.095324000
6	3.264971000	-0.955614000	-0.787905000
6	-2.302929000	1.627129000	-2.986556000
6	-0.959989000	-2.195419000	4.181484000
6	0.015802000	-1.504013000	3.396930000
6	2.284695000	1.991996000	0.825053000
6	3.120241000	-0.835520000	0.595339000
6	-0.122788000	1.470900000	-2.428277000
6	-1.036510000	1.809700000	-3.471352000
6	2.233578000	-0.931986000	2.634178000
6	1.347465000	-1.201993000	3.691122000
6	2.018204000	1.803701000	-1.361401000
6	3.401428000	2.633054000	0.233764000
6	4.201762000	-0.843418000	1.530694000
6	1.253850000	1.735686000	-2.519444000
6	3.656144000	-0.917807000	2.781356000
6	3.250868000	2.496467000	-1.130965000
1	-2.927508000	-3.036601000	3.612155000
1	3.238712000	-1.834436000	-3.481581000
1	0.853794000	2.463324000	5.219335000
1	-4.184684000	-3.154804000	0.766065000
1	0.743257000	-2.203190000	-4.433277000
1	-5.247626000	0.843297000	1.268199000
1	-4.175901000	1.014944000	3.721898000
1	-3.884841000	-2.906104000	-1.901694000
1	2.927508000	3.036601000	3.612155000
1	-3.238712000	1.834436000	-3.481581000
1	-0.853794000	-2.463324000	5.219335000
1	4.184684000	3.154804000	0.766065000
1	-0.743257000	2.203190000	-4.433277000
1	5.247626000	-0.843297000	1.268199000
1	4.175901000	-1.014944000	3.721898000
1	3.884841000	2.906104000	-1.901694000
6	-1.852058000	1.280511000	5.087749000
6	-2.560270000	0.201255000	5.639061000
6	-1.613126000	2.396877000	5.905322000
6	-2.964657000	0.211573000	6.972849000
6	-1.995780000	2.394905000	7.247416000
6	-2.669275000	1.300884000	7.793946000
1	-2.773658000	-0.656007000	5.019194000
1	-1.126810000	3.271510000	5.493314000
1	-2.959935000	1.299611000	8.838365000
6	1.841249000	2.173203000	-3.815485000
6	1.947012000	1.284329000	-4.891765000
6	2.314649000	3.483500000	-3.976847000
6	2.551588000	1.682514000	-6.085553000
6	2.904713000	3.882510000	-5.176194000
6	3.035642000	2.981851000	-6.235112000
1	1.585680000	0.271741000	-4.775844000
1	2.211506000	4.191507000	-3.162816000
1	3.509489000	3.288488000	-7.159800000
6	-4.632869000	1.029259000	-1.377748000
6	-5.030842000	0.118388000	-2.367781000
6	-5.534302000	2.029048000	-0.990369000

6	-6.309759000	0.181589000	-2.920449000
6	-6.811996000	2.094506000	-1.551448000
6	-7.213482000	1.163574000	-2.508185000
1	-4.332510000	-0.634931000	-2.702514000
1	-5.228771000	2.767144000	-0.257598000
1	-8.205367000	1.214266000	-2.941512000
6	-1.841249000	-2.173203000	-3.815485000
6	-2.314649000	-3.483500000	-3.976847000
6	-1.947012000	-1.284329000	-4.891765000
6	-2.904713000	-3.882510000	-5.176194000
6	-2.551588000	-1.682514000	-6.085553000
6	-3.035642000	-2.981851000	-6.235112000
1	-2.211506000	-4.191507000	-3.162816000
1	-1.585680000	-0.271741000	-4.775844000
1	-3.509489000	-3.288488000	-7.159800000
6	1.852058000	-1.280511000	5.087749000
6	1.613126000	-2.396877000	5.905322000
6	2.560270000	-0.201255000	5.639061000
6	1.995780000	-2.394905000	7.247416000
6	2.964657000	-0.211573000	6.972849000
6	2.669275000	-1.300884000	7.793946000
1	1.126810000	-3.271510000	5.493314000
1	2.773658000	0.656007000	5.019194000
1	2.959935000	-1.299611000	8.838365000
6	4.632869000	-1.029259000	-1.377748000
6	5.534302000	-2.029048000	-0.990369000
6	5.030842000	-0.118388000	-2.367781000
6	6.811996000	-2.094506000	-1.551448000
6	6.309759000	-0.181589000	-2.920449000
6	7.213482000	-1.163574000	-2.508185000
1	5.228771000	-2.767144000	-0.257598000
1	4.332510000	0.634931000	-2.702514000
1	8.205367000	-1.214266000	-2.941512000
6	3.460679000	5.287376000	-5.303615000
9	2.725272000	6.185360000	-4.604104000
9	4.731832000	5.354336000	-4.822416000
9	3.498604000	5.700043000	-6.590118000
6	2.660865000	0.687446000	-7.224240000
9	1.486153000	0.580764000	-7.897585000
9	3.611548000	1.038699000	-8.118119000
9	2.967456000	-0.556395000	-6.769996000
6	3.654097000	1.005358000	7.558253000
9	4.319970000	1.715449000	6.613810000
9	2.750984000	1.851413000	8.127126000
9	4.544394000	0.669227000	8.518522000
6	1.700625000	-3.598040000	8.123066000
9	2.764155000	-4.440983000	8.182261000
9	1.412921000	-3.226234000	9.392953000
9	0.647729000	-4.315026000	7.660342000
6	6.752945000	0.855947000	-3.931966000
9	7.624518000	0.347093000	-4.833029000
9	5.707230000	1.369935000	-4.620971000
9	7.376017000	1.897625000	-3.315926000
6	7.763873000	-3.176183000	-1.083596000
9	8.806627000	-3.340037000	-1.927171000
9	8.276473000	-2.876869000	0.141165000
9	7.136495000	-4.371868000	-0.966949000
6	-7.763873000	3.176183000	-1.083596000
9	-8.806627000	3.340037000	-1.927171000
9	-8.276473000	2.876869000	0.141165000
9	-7.136495000	4.371868000	-0.966949000
6	-6.752945000	-0.855947000	-3.931966000
9	-7.624518000	-0.347093000	-4.833029000
9	-5.707230000	-1.369935000	-4.620971000
9	-7.376017000	-1.897625000	-3.315926000
6	-2.660865000	-0.687446000	-7.224240000
9	-1.486153000	-0.580764000	-7.897585000
9	-3.611548000	-1.038699000	-8.118119000
9	-2.967456000	0.556395000	-6.769996000
6	-3.460679000	-5.287376000	-5.303615000
9	-2.725272000	-6.185360000	-4.604104000
9	-4.731832000	-5.354336000	-4.822416000
9	-3.498604000	-5.700043000	-6.590118000
6	-1.700625000	3.598040000	8.123066000
9	-2.764155000	4.440983000	8.182261000
9	-1.412921000	3.226234000	9.392953000
9	-0.647729000	4.315026000	7.660342000
6	-3.654097000	-1.005358000	7.558253000
9	-4.319970000	-1.715449000	6.613810000
9	-2.750984000	-1.851413000	8.127126000
9	-4.544394000	-0.669227000	8.518522000

W[T*m*-CF_3PC]$_2$ 2 (45°)

74	0.000000000	0.000000000	-1.150463000
7	0.455964000	1.248916000	-2.868152000
7	0.967421000	-1.020900000	0.547823000
7	1.595705000	1.435537000	-0.550597000
7	1.790679000	-0.933989000	-1.936288000
7	-0.455964000	-1.248916000	-2.868152000
7	-0.967421000	1.020900000	0.547823000
7	-1.595705000	-1.435537000	-0.550597000
7	-1.790679000	0.933989000	-1.936288000
6	0.019427000	1.810578000	-5.047311000
6	0.335794000	-1.467414000	1.707663000
6	0.535380000	-1.436408000	-3.799042000
6	1.019005000	1.764482000	1.842900000
6	1.307780000	-1.775202000	2.706514000
6	1.385312000	1.871826000	-4.863967000
6	1.651077000	1.587268000	-3.483536000
6	1.809069000	-1.293234000	-3.262450000
6	1.889596000	1.829491000	0.756062000
6	2.338193000	-1.104583000	0.814418000
6	2.539604000	-1.541865000	2.159875000
6	2.686953000	1.851066000	-1.318771000
6	2.790926000	1.836071000	-2.723657000
6	3.094849000	-1.037453000	-1.479755000
6	3.133442000	-1.558744000	-3.689395000
6	3.176722000	2.444267000	0.802586000
6	3.385071000	-1.028474000	-0.119937000
6	3.662690000	2.464336000	-0.474930000
6	3.939873000	-1.381404000	-2.584584000
6	-0.019427000	-1.810578000	-5.047311000
6	-0.335794000	1.467414000	1.707663000
6	-0.535380000	1.436408000	-3.799042000
6	-1.019005000	-1.764482000	1.842900000
6	-1.307780000	1.775202000	2.706514000
6	-1.385312000	-1.871826000	-4.863967000
6	-1.651077000	-1.587268000	-3.483536000
6	-1.809069000	1.293234000	-3.262450000
6	-1.889596000	-1.829491000	0.756062000
6	-2.338193000	1.104583000	0.814418000
6	-2.539604000	1.541865000	2.159875000
6	-2.686953000	-1.851066000	-1.318771000
6	-2.790926000	-1.836071000	-2.723657000
6	-3.094849000	1.037453000	-1.479755000
6	-3.133442000	1.558744000	-3.689395000
6	-3.176722000	-2.444267000	0.802586000
6	-3.385071000	1.028474000	-0.119937000
6	-3.662690000	-2.464336000	-0.474930000
6	-3.939873000	1.381404000	-2.584584000
1	0.538086000	-2.014848000	-5.951073000
1	1.076375000	-2.182205000	3.679061000
1	2.126671000	2.145147000	-5.598183000
1	3.427254000	-1.869291000	-4.682732000
1	3.506409000	-1.722090000	2.604183000
1	3.632850000	2.857314000	1.688261000
1	4.583386000	2.906496000	-0.822324000
1	5.005662000	-1.536675000	-2.524818000
1	-0.538086000	2.014848000	-5.951073000
1	-1.076375000	2.182205000	3.679061000
1	-2.126671000	-2.145147000	-5.598183000
1	-3.427254000	1.869291000	-4.682732000
1	-3.506409000	1.722090000	2.604183000
1	-3.632850000	-2.857314000	1.688261000
1	-4.583386000	-2.906496000	-0.822324000
1	-5.005662000	1.536675000	-2.524818000
6	4.057789000	2.264585000	-3.368962000
6	5.275795000	1.654214000	-3.029153000
6	4.078026000	3.292420000	-4.324592000
6	6.465082000	2.034495000	-3.650088000
6	5.263877000	3.649566000	-4.968389000
6	6.465892000	3.022019000	-4.638553000
1	5.283002000	0.879387000	-2.276263000
1	3.163191000	3.820804000	-4.561005000
1	7.387378000	3.303112000	-5.135187000
6	-4.787290000	1.167622000	0.354434000
6	-5.337780000	0.223425000	1.230090000
6	-5.573821000	2.265962000	-0.026255000
6	-6.648692000	0.357053000	1.691071000
6	-6.883623000	2.396855000	0.436007000
6	-7.433109000	1.438806000	1.291604000
1	-4.735115000	-0.619936000	1.538364000
1	-5.148755000	3.030682000	-0.665448000
1	-8.450750000	1.541407000	1.648354000
6	1.510709000	2.186329000	3.190973000
6	1.637490000	1.235600000	4.210842000
6	1.835539000	3.518991000	3.470890000

6	2.110802000	1.597735000	5.470874000
6	2.295238000	3.883654000	4.740394000
6	2.448493000	2.924965000	5.742513000
1	1.376110000	0.208768000	4.004900000
1	1.719918000	4.271781000	2.698858000
1	2.810272000	3.211185000	6.723187000
6	4.787290000	-1.167622000	0.354434000
6	5.573821000	-2.265962000	-0.026255000
6	5.337780000	-0.223425000	1.230090000
6	6.883623000	-2.396855000	0.436007000
6	6.648692000	-0.357053000	1.691071000
6	7.433109000	-1.438806000	1.291604000
1	5.148755000	-3.030682000	-0.665448000
1	4.735115000	0.619936000	1.538364000
1	8.450750000	-1.541407000	1.648354000
6	-4.057789000	-2.264585000	-3.368962000
6	-4.078026000	-3.292420000	-4.324592000
6	-5.275795000	-1.654214000	-3.029153000
6	-5.263877000	-3.649566000	-4.968389000
6	-6.465082000	-2.034495000	-3.650088000
6	-6.465892000	-3.022019000	-4.638553000
1	-3.163191000	-3.820804000	-4.561005000
1	-5.283002000	-0.879387000	-2.276263000
1	-7.387378000	-3.303112000	-5.135187000
6	-1.510709000	-2.186329000	3.190973000
6	-1.835539000	-3.518991000	3.470890000
6	-1.637490000	-1.235600000	4.210842000
6	-2.295238000	-3.883654000	4.740394000
6	-2.110802000	-1.597735000	5.470874000
6	-2.448493000	-2.924965000	5.742513000
1	-1.719918000	-4.271781000	2.698858000
1	-1.376110000	-0.208768000	4.004900000
1	-2.810272000	-3.211185000	6.723187000
6	-7.725124000	3.572755000	-0.022442000
9	-6.972500000	4.681975000	-0.221416000
9	-8.348430000	3.298357000	-1.200564000
9	-8.685729000	3.886817000	0.875776000
6	-7.186328000	-0.675677000	2.661952000
9	-6.621394000	-0.529264000	3.891382000
9	-8.523752000	-0.587730000	2.818893000
9	-6.905478000	-1.938752000	2.248568000
6	-7.760408000	-1.331354000	-3.292516000
9	-7.744209000	-0.863890000	-2.020269000
9	-7.981502000	-0.262881000	-4.106296000
9	-8.829453000	-2.151510000	-3.412527000
6	-5.244497000	-4.759281000	-6.002434000
9	-5.399040000	-5.980216000	-5.427225000
9	-6.236718000	-4.614473000	-6.910211000
9	-4.070021000	-4.788010000	-6.681829000
6	-2.331582000	-0.537473000	6.531613000
9	-2.038117000	-0.991768000	7.771465000
9	-1.579921000	0.569007000	6.310033000
9	-3.632097000	-0.137340000	6.549299000
6	-2.666773000	-5.328377000	5.012179000
9	-2.631511000	-5.622865000	6.331155000
9	-3.926108000	-5.600373000	4.574446000
9	-1.829665000	-6.184634000	4.377502000
6	2.666773000	5.328377000	5.012179000
9	2.631511000	5.622865000	6.331155000
9	3.926108000	5.600373000	4.574446000
9	1.829665000	6.184634000	4.377502000
6	2.331582000	0.537473000	6.531613000
9	2.038117000	0.991768000	7.771465000
9	1.579921000	-0.569007000	6.310033000
9	3.632097000	0.137340000	6.549299000
6	7.186328000	0.675677000	2.661952000
9	6.621394000	0.529264000	3.891382000
9	8.523752000	0.587730000	2.818893000
9	6.905478000	1.938752000	2.248568000
6	7.725124000	-3.572755000	-0.022442000
9	6.972500000	-4.681975000	-0.221416000
9	8.348430000	-3.298357000	-1.200564000
9	8.685729000	-3.886817000	0.875776000
6	5.244497000	4.759281000	-6.002434000
9	5.399040000	5.980216000	-5.427225000
9	6.236718000	4.614473000	-6.910211000
9	4.070021000	4.788010000	-6.681829000
6	7.760408000	1.331354000	-3.292516000
9	7.744209000	0.863890000	-2.020269000
9	7.981502000	0.262881000	-4.106296000
9	8.829453000	2.151510000	-3.412527000

W[TPFPC]$_2$ (135°)

74	0.000000000	0.000000000	0.375203000
7	-0.895624000	1.011588000	-1.387203000
7	1.938037000	-0.766482000	1.182137000
7	0.488299000	1.302731000	2.032069000
7	1.441698000	1.486651000	-0.233190000
7	0.895624000	-1.011588000	-1.387203000
7	-1.938037000	0.766482000	1.182137000
7	-0.488299000	-1.302731000	2.032069000
7	-1.441698000	-1.486651000	-0.233190000
6	-2.917837000	3.602605000	6.104613000
6	1.388921000	-1.271908000	3.550799000
6	-2.459594000	3.047346000	4.914238000
6	1.940584000	-1.748961000	4.846749000
6	2.845773000	-2.854191000	7.279285000
6	-1.156546000	1.772028000	-3.556844000
6	2.402604000	-1.515676000	-3.070532000
6	1.906418000	-1.017556000	6.032924000
6	2.245694000	-1.063815000	-1.728569000
6	2.340282000	-1.556686000	7.244130000
6	2.269913000	-0.912818000	2.529336000
6	-0.223799000	1.496203000	-2.513048000
6	-0.060681000	1.542847000	3.277854000
6	3.159059000	-0.727428000	0.514520000
6	3.310597000	-0.859536000	-0.860198000
6	3.686230000	-0.854687000	2.694232000
6	5.304535000	-2.340538000	-1.108227000
6	1.114574000	1.896151000	-2.583155000
6	0.854941000	2.322309000	4.050279000
6	4.236561000	-0.739421000	1.450633000
6	2.059165000	2.072045000	-4.943252000
6	4.678539000	-1.118808000	-1.387842000
6	1.683876000	1.981028000	2.002399000
6	1.899929000	1.960976000	-1.448753000
6	6.575334000	-2.650351000	-1.585017000
6	1.529200000	2.655889000	-3.794683000
6	2.221586000	2.082238000	0.728764000
6	2.324296000	2.814609000	-6.093550000
6	1.939105000	2.600835000	3.251563000
6	5.369452000	-0.232586000	-2.214151000
6	1.287647000	4.034360000	-3.834933000
6	3.052097000	2.777286000	-1.226808000
6	7.250174000	-1.728294000	-2.384168000
6	2.056342000	4.181402000	-6.108384000
6	3.246295000	2.860350000	0.131404000
6	6.642047000	-0.517464000	-2.706875000
6	1.541478000	4.799246000	-4.969265000
6	2.917837000	-3.602605000	6.104613000
6	-1.388921000	1.271908000	3.550799000
6	2.459594000	-3.047346000	4.914238000
6	-1.940584000	1.748961000	4.846749000
6	-2.845773000	2.854191000	7.279285000
6	1.156546000	-1.772028000	-3.556844000
6	-2.402604000	1.515676000	-3.070532000
6	-1.906418000	1.017556000	6.032924000
6	-2.245694000	1.063815000	-1.728569000
6	-2.340282000	1.556686000	7.244130000
6	-2.269913000	0.912818000	2.529336000
6	0.223799000	-1.496203000	-2.513048000
6	0.060681000	-1.542847000	3.277854000
6	-3.159059000	0.727428000	0.514520000
6	-3.310597000	0.859536000	-0.860198000
6	-3.686230000	0.854687000	2.694232000
6	-5.304535000	2.340538000	-1.108227000
6	-1.114574000	-1.896151000	-2.583155000
6	-0.854941000	-2.322309000	4.050279000
6	-4.236561000	0.739421000	1.450633000
6	-2.059165000	-2.072045000	-4.943252000
6	-4.678539000	1.118808000	-1.387842000
6	-1.683876000	-1.981028000	2.002399000
6	-1.899929000	-1.960976000	-1.448753000
6	-6.575334000	2.650351000	-1.585017000
6	-1.529200000	-2.655889000	-3.794683000
6	-2.221586000	-2.082238000	0.728764000
6	-2.324296000	-2.814609000	-6.093550000
6	-1.939105000	-2.600835000	3.251563000
6	-5.369452000	0.232586000	-2.214151000
6	-1.287647000	-4.034360000	-3.834933000
6	-3.052097000	-2.777286000	-1.226808000
6	-7.250174000	1.728294000	-2.384168000
6	-2.056342000	-4.181402000	-6.108384000
6	-3.246295000	-2.860350000	0.131404000
6	-6.642047000	0.517464000	-2.706875000
6	-1.541478000	-4.799246000	-4.969265000
9	-3.407471000	4.846823000	6.132520000

9	-2.505140000	3.803569000	3.810159000
9	3.258942000	-3.381728000	8.433246000
9	4.668587000	-3.264488000	-0.377460000
1	-0.888794000	2.165450000	-4.525538000
9	1.446941000	0.239816000	6.041997000
1	3.351415000	-1.652154000	-3.564984000
9	2.271154000	-0.836652000	8.369867000
9	2.309024000	0.757859000	-4.981991000
1	4.191235000	-0.952171000	3.644154000
9	7.149580000	-3.821895000	-1.290764000
1	0.664851000	2.664106000	5.056375000
9	2.826338000	2.219726000	-7.181860000
1	5.281805000	-0.722741000	1.180900000
1	2.801597000	3.209458000	3.485879000
9	4.814862000	0.932692000	-2.570290000
9	0.760125000	4.648491000	-2.767883000
9	8.472148000	-2.008279000	-2.840328000
9	2.292261000	4.898824000	-7.208349000
1	3.597926000	3.282796000	-2.008944000
1	3.985865000	3.440970000	0.665388000
9	1.284016000	6.111628000	-4.980836000
9	7.280661000	0.366664000	-3.482768000
9	3.407471000	-4.846823000	6.132520000
9	2.505140000	-3.803569000	3.810159000
9	-3.258942000	3.381728000	8.433246000
9	-4.668587000	3.264488000	-0.377460000
1	0.888794000	-2.165450000	-4.525538000
9	-1.446941000	-0.239816000	6.041997000
1	-3.351415000	1.652154000	-3.564984000
9	-2.271154000	0.836652000	8.369867000
9	-2.309024000	-0.757859000	-4.981991000
1	-4.191235000	0.952171000	3.644154000
9	-7.149580000	3.821895000	-1.290764000
1	-0.664851000	-2.664106000	5.056375000
9	-2.826338000	-2.219726000	-7.181860000
1	-5.281805000	0.722741000	1.180900000
1	-2.801597000	-3.209458000	3.485879000
9	-4.814862000	-0.932692000	-2.570290000
9	-0.760125000	-4.648491000	-2.767883000
9	-8.472148000	2.008279000	-2.840328000
9	-2.292261000	-4.898824000	-7.208349000
1	-3.597926000	-3.282796000	-2.008944000
1	-3.985865000	-3.440970000	0.665388000
9	-1.284016000	-6.111628000	-4.980836000
9	-7.280661000	-0.366664000	-3.482768000

W[T*m*-$CF_3PC]_2$ 2 (45°)

74	0.000000000	0.000000000	0.897045000
7	-0.697959000	1.122688000	2.617802000
7	-0.734332000	-1.198739000	-0.805831000
7	-1.863849000	1.076876000	0.281738000
7	-1.572253000	-1.251644000	1.698918000
7	0.697959000	-1.122688000	2.617802000
7	0.734332000	1.198739000	-0.805831000
7	1.863849000	-1.076876000	0.281738000
7	1.572253000	1.251644000	1.698918000
6	-0.399797000	1.822191000	4.783356000
6	-0.037759000	-1.487472000	-1.981117000
6	-0.231023000	-1.505514000	3.552688000
6	-1.344539000	1.592527000	-2.093627000
6	-0.944594000	-1.900628000	-3.003101000
6	-1.752609000	1.653132000	4.580973000
6	-1.940898000	1.271749000	3.214345000
6	-1.509438000	-1.619598000	3.021307000
6	-2.214604000	1.449544000	-1.015747000
6	-2.055318000	-1.572181000	-1.072904000
6	-2.185519000	-1.956811000	-2.440969000
6	-3.007631000	1.317543000	1.047403000
6	-3.095576000	1.337396000	2.448885000
6	-2.793129000	-1.701939000	1.226823000
6	-2.718580000	-2.241270000	3.427025000
6	-3.580732000	1.859337000	-1.061635000
6	-3.064281000	-1.793452000	-0.128882000
6	-4.068971000	1.774523000	0.208832000
6	-3.519647000	-2.292342000	2.308028000
6	0.399797000	-1.822191000	4.783356000
6	0.037759000	1.487472000	-1.981117000
6	0.231023000	1.505514000	3.552688000
6	1.344539000	-1.592527000	-2.093627000
6	0.944594000	1.900628000	-3.003101000
6	1.752609000	-1.653132000	4.580973000
6	1.940898000	-1.271749000	3.214345000
6	1.509438000	1.619598000	3.021307000
6	2.214604000	-1.449544000	-1.015747000
6	2.055318000	1.572181000	-1.072904000
6	2.185519000	1.956811000	-2.440969000
6	3.007631000	-1.317543000	1.047403000
6	3.095576000	-1.337396000	2.448885000
6	2.793129000	1.701939000	1.226823000
6	2.718580000	2.241270000	3.427025000
6	3.580732000	-1.859337000	-1.061635000
6	3.064281000	1.793452000	-0.128882000
6	4.068971000	-1.774523000	0.208832000
6	3.519647000	2.292342000	2.308028000
1	-0.102539000	-2.159761000	5.679643000
1	-0.654673000	-2.169004000	-4.007475000
1	-2.555441000	1.859294000	5.273764000
1	-2.920829000	-2.640617000	4.411658000
1	-3.110689000	-2.272689000	-2.897919000
1	-4.086267000	2.212942000	-1.947136000
1	-5.053008000	2.043246000	0.559535000
1	-4.496538000	-2.741367000	2.209265000
1	0.102539000	2.159761000	5.679643000
1	0.654673000	2.169004000	-4.007475000
1	2.555441000	-1.859294000	5.273764000
1	2.920829000	2.640617000	4.411658000
1	3.110689000	2.272689000	-2.897919000
1	4.086267000	-2.212942000	-1.947136000
1	5.053008000	-2.043246000	0.559535000
1	4.496538000	2.741367000	2.209265000
6	-4.377145000	1.782308000	3.067370000
6	-5.545527000	1.005701000	3.044572000
6	-4.493715000	3.078184000	3.603473000
6	-6.767720000	1.480191000	3.531820000
6	-5.699246000	3.569317000	4.114255000
6	-6.844172000	2.767266000	4.072700000
9	-5.526442000	-0.226211000	2.524918000
9	-3.443154000	3.907821000	3.599350000
9	-7.860623000	0.710890000	3.481120000
9	-5.770642000	4.805713000	4.619067000
9	-8.003514000	3.231201000	4.540792000
6	4.292733000	2.520312000	-0.565049000
6	5.538037000	1.914559000	-0.761265000
6	4.213022000	3.906017000	-0.784187000
6	6.660986000	2.646220000	-1.166936000
6	5.315279000	4.658333000	-1.195197000
6	6.547502000	4.022238000	-1.386406000
9	5.688090000	0.599749000	-0.569793000
9	3.050995000	4.543432000	-0.596803000
9	7.837472000	2.035361000	-1.346691000
9	5.203291000	5.974542000	-1.401268000

9	7.610735000	4.729562000	-1.772410000
6	-1.886777000	2.240926000	-3.329171000
6	-2.644503000	1.572787000	-4.297205000
6	-1.681136000	3.618515000	-3.523533000
6	-3.147960000	2.226054000	-5.428121000
6	-2.170139000	4.295206000	-4.643916000
6	-2.906897000	3.591615000	-5.603338000
9	-2.923117000	0.271448000	-4.157551000
9	-1.010388000	4.328461000	-2.609078000
9	-3.859133000	1.551969000	-6.338924000
9	-1.951055000	5.604952000	-4.800484000
9	-3.385000000	4.224243000	-6.675895000
6	-4.292733000	-2.520312000	-0.565049000
6	-4.213022000	-3.906017000	-0.784187000
6	-5.538037000	-1.914559000	-0.761265000
6	-5.315279000	-4.658333000	-1.195197000
6	-6.660986000	-2.646220000	-1.166936000
6	-6.547502000	-4.022238000	-1.386406000
9	-3.050995000	-4.543432000	-0.596803000
9	-5.688090000	-0.599749000	-0.569793000
9	-5.203291000	-5.974542000	-1.401268000
9	-7.837472000	-2.035361000	-1.346691000
9	-7.610735000	-4.729562000	-1.772410000
6	4.377145000	-1.782308000	3.067370000
6	4.493715000	-3.078184000	3.603473000
6	5.545527000	-1.005701000	3.044572000
6	5.699246000	-3.569317000	4.114255000
6	6.767720000	-1.480191000	3.531820000
6	6.844172000	-2.767266000	4.072700000
9	3.443154000	-3.907821000	3.599350000
9	5.526442000	0.226211000	2.524918000
9	5.770642000	-4.805713000	4.619067000
9	7.860623000	-0.710890000	3.481120000
9	8.003514000	-3.231201000	4.540792000
6	1.886777000	-2.240926000	-3.329171000
6	1.681136000	-3.618515000	-3.523533000
6	2.644503000	-1.572787000	-4.297205000
6	2.170139000	-4.295206000	-4.643916000
6	3.147960000	-2.226054000	-5.428121000
6	2.906897000	-3.591615000	-5.603338000
9	1.010388000	-4.328461000	-2.609078000
9	2.923117000	-0.271448000	-4.157551000
9	1.951055000	-5.604952000	-4.800484000
9	3.859133000	-1.551969000	-6.338924000
9	3.385000000	-4.224243000	-6.675895000